Laterally Loaded Monopile in Dry and Saturated Sand - Static and Cyclic Loading

Experimental and Numerical Studies

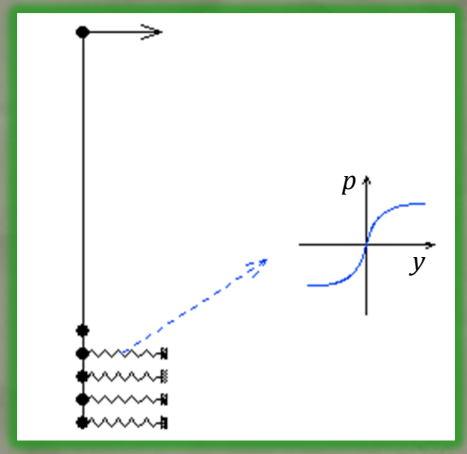

Master Project, June 2011
Aalborg University Esbjerg
Ida Folke Møller & Tina Christiansen

Title	Laterally Loaded Monopile in Dry and Saturated Sand – Static and Cyclic Loading *Experimental and Numerical Studies*

Authors	Ida Folke Møller Tina Højgaard Christiansen
Supervisors	Ronnie Refstrup Pedersen Lars Damkilde

Period	February 1st – June 17th , 2011

Abstract

This report is concerned with static and cyclic horizontal loading of monopiles used in offshore wind turbine foundation. Today the p-y method is used for determination of lateral bearing capacity and deflections of piles. However, the reliability of the p-y method in connection with rigid piles, i.e. piles with low slenderness ratios, has been questioned.

In this project the efficiency of the p-y method is tested for a rigid pile and the design code recommended p-y curves are investigated. In order to perform these investigations, a number of static pile experiments are executed as well as a number of p-y experiments.

All experiments performed in this project are 1g tests. Both experiments with dry and saturated sand are performed.

The p-y experiments indicate that the design code recommended p-y curves overestimate the initial stiffness and generally underestimate the ultimate bearing capacity. When applying the recommended p-y curves as nonlinear springs in a 2D Winkler beam model, the global response therefore underestimates the pile displacement to a given load and predicts an ultimate bearing capacity that is too low.

When applying the experimental p-y curves to a 2D Winkler model, the global response coincides with the results of the static experiments. This indicates the p-y method is a reasonable modelling approach when using correct input.

Alternative design methods are tested for static loading conditions. That is 3D modelling using Plaxis 3D foundation with non associated plasticity, and Abaqus with a user defined implementation of Mohr Coulomb soil using associated plasticity. The best results are achieved using Abaqus.

9 cyclic experiments are executed with a displacement controlled test setup. The pile is loaded with 12,000-24,000 cycles. In the cyclic experiments, a steady state is observed. That is a condition in which the soil properties have obtained their maximum potential and no longer changes. The results of the cyclic experiments indicate that the soil properties are improved due to cyclic loading, as both secant stiffness and ultimate bearing capacity are significantly increased.

Comparing the results of static tests performed in improved soil conditions after a cyclic test indicates the stiffness of the curves being the same as the one predicted by the design code recommendation, however the design code significantly underestimates the bearing capacity.

Number of pages	93
Number of copies	5
Attachments	Appendix report and programs are enclosed on CD

Titel	Horisontalt belastet monopæl i tørt og vandmættet sand- statisk og cyklisk belastning *Eksperimentelle og numeriske studier*
Forfattere	Ida Folke Møller Tina Højgaard Christiansen
Vejledere	Ronnie Refstrup Pedersen Lars Damkilde
Periode	1. februar – 17. Juni 2011

Resumé

Denne rapport vedrører statisk og cyklisk horisontal belastning af monopæle, som er anvendt til fundering af offshore vindmøller. I dag anvendes p-y metoden til bestemmelse af vandret bæreevne og flytninger af pæle. Imidlertid sættes der spørgsmålstegn ved troværdigheden af p-y metoden i forbindelse med pæle med lavt stivhedsforhold, dvs. pæle med stor diameter i forhold til deres længde.
I dette projekt testes p-y metoden for en sådan pæl, og de teoretiske p-y kurver undersøges. For at kunne gennemføre disse undersøgelser gennemføres et antal statiske pæleforsøg, samt en række p-y forsøg.
Alle gennemførte forsøg er 1g tests. Forsøg med både tørt og vandmættet sand gennemføres.
P-y forsøgene indikerer, at de teoretiske p-y kurver overestimerer den initiale stivhed og generelt underestimerer den ultimale bæreevne. Når de teoretiske p-y kurver anvendes som ikke lineære fjedre i en 2D Winkler model, underestimeres flytningen til en given last og den ultimale bæreevne beregnes for lav.
Når de eksperimentelle p-y kurver anvendes i en 2D Winkler model bliver det globale respons sammenfaldende med forsøgsresultaterne fra de statiske pæleforsøg. Dette tyder på, at p-y metoden er en fornuftig model tilnærmelse når der anvendes korrekt input.
Alternative design metoder testes også for statiske lasttilfælde. Det drejer sig om 3D modellering i Plaxis 3D Foundation og Abaqus. I Plaxis anvdendes en jordmodel med ikke associeret plasticitet. I Abaqus anvendes en jordmodel med associeret plasticitet. Begge modeller bygger på Mohr Coulomb, og i Abaqus er en brugerdefineret metode for implementering af Mohr Coulomb anvendt.
9 cykliske forsøg gennemføres med en flytningsstyret forsøgsopstilling. Pælen belastes med 12,000-24,000 cykler. I forbindelse med de cykliske forsøg observeres steady state. Steady state er et stadie, hvor jordens egenskaber har opnået deres maksimale potentiale og ikke længere forandres. Resultaterne af de cykliske forsøg indikerer, at jorden egenskaber forbedres i takt med en cyklisk belastning, idet både sekant stivhed og ultimal bæreevne øges markant.
Resultaterne fra statiske tests gennemført i forbedrede jordforhold efter cyklisk belastning er sammenlignet med løsningen fra 2D Winkler modellen med de teoretiske p-y fjedre. Af sammenligningen fremgår det, at kurvernes initialstivhed er sammenfaldende, dog underestimeres bæreevnen markant når de teoretiske p-y fjedre anvendes.

Sideantal	93
Oplag	5
Vedlagt	Appendiks rapport og programmer er vedlagt på CD

Preface

This project is our master thesis. The project is based on laboratory experiments carried out on the Esbjerg University Campus.
The project is the first of its kind in Esbjerg and therefore a lot of work and time has been invested in developing, establishing and testing the experimental setups used in this project. This has been a most interesting and challenging assignment.
Despite the simplicity of the experimental setup, we are convinced that the results presented in this project are fully reliable and the tendencies described can be trusted.

The project consists of a main report, an appendix report and two MATLAB programs. The appendix report and the programs are enclosed on a CD, which is attached in the back of this main report.
The appendix report and the programs are referred to directly when relevant, but the main report can stand alone.

Electronic as well as literary references are also referred to directly, and a complete list of references can be found in the end of this report. Electronic references are referred to by [W.nr.] and literary references by [nr.].
Some references have not been possible to procure but these are referred to by other authors. As it might be of interest for the reader to know about this material, a reference has been made: [U.nr.]

All illustrations and tables are work of the authors unless a reference indicates otherwise.

Acknowledgements
Many people have been helpful throughout the process.

We would like to thank supervisors professor Lars Damkilde and associate professor Ronnie Refstrup Pedersen for their support and involvement throughout the whole procedure. This is most appreciated.

Thanks to Ph.D student Søren Lambertsen and associate professor Sven Krabbenhøft for setting up the Labview measuring program and assisting in the laboratory in general. The experimental work presented in this project had not been possible without their help.

For great help on processing the piles, welding, grinding, drilling etc. and competent guidance based on practical experience we would like to thank Aksel Christiansen and Flemming Holm.

The research presented in this report is financially supported by the SUC Fund Esbjerg under grant 2010-5745.

Tina Højgaard Christiansen

Ida Folke Møller

Table of Contents

1 Introduction

Since the late 1980's wind turbines have been installed offshore. The World's first offshore windfarm, Vindeby (DK) with a total capacity of 4.95 MW evenly distributed between 11 wind turbines was inaugurated in 1991. Denmark and United Kingdom are leading countries in the wind technology and installation of offshore windfarms, for instance Horns Rev I and II, in Denmark and Thanet in the UK [W.1].

The primary producers of wind turbines are Vestas and Siemens, and until recently the greatest offshore wind turbines had a capacity of 2.3-3.6 MW.
Currently the greatest offshore windfarm project is London Array, the project phase 1 is under construction and when finished 175 3.6 MW wind turbines are expected to supply 480,000 British homes with electricity saving the environment for 925,000 tonnes of CO_2 a year, [W.2]. In April 2010 the first German offshore wind farm was inaugurated with 5 MW turbines [W.3] and with both Siemens and Vestas, launching new offshore wind turbines with capacities up till 7 MW, there is no doubt that offshore wind turbines provide a great potential for the future renewable energy production.

Figure 1.1: To the left: Monopile foundations and transition piece ready for shipping. The piles have diameters of about 4 m [W.4]. In the middle: 2.3 MW wind turbine from Horns Rev, founded on a monopile foundation [W.4]. To the right: 5 MW turbine from Hooksiel offshore windfarm in Germany. The turbine is founded on a tripod foundation with three monopiles [W.5].

The most widely used type of foundation for offshore wind turbines is monopile foundation. With the offshore turbines continuously increasing in size, also the foundation increases. In the future it is believed that alternative foundation designs using several monopiles will be applied, see figure 1.1. Today the foundation costs amount to approximately 20-25 % of the total installation cost of an offshore wind turbine, [1], [W.6]. With increasing size of the foundation it is therefore important to secure a cost-efficient design.

At seas the dominating loads are lateral loading and corresponding bending moment from wind and waves. The foundation should be able to carry the loads without causing unacceptable deformations. The most widely used method of calculating laterally loaded piles is the so-called p-y method. Lately the reliability of the method has been questioned. The main reason is that monopiles originally was used by the petroleum industry in founding of fixed offshore platforms. Therefore the p-y method is developed for another type of piles, than the ones used in wind turbine foundation. Monopiles used in wind turbine foundation are often short rigid piles whereas piles used in platform foundations often are long and slender.

This project focuses on the p-y method applied to modern offshore wind turbine monopile foundations also alternative designing methods are investigated.

1.1 Historical review of the p-y approach for sand

Monopile foundation was originally used in the offshore oil and gas industry. From the 1950s and 60s the American Petroleum Industry began installation of fixed offshore platforms in the Mexican Gulf, and from the 1970s installation of fixed platforms in the North Sea took place. Many of these platforms were installed on monopile foundations. Therefore a lot of experience regarding monopile foundation is related to the type of piles used for fixed platforms, i.e. often long and slender piles.

Lack of computer capacity and knowledge was the reason why a pile-soil system had to be modelled with simple tools. In many cases the design criteria is related to the lateral displacement of the piles when exposed to lateral loading and bending moment caused by wind and waves. The p-y approach has been widely used to design piles subjected to lateral static or dynamic loading [2]. Based on the p-y approach the lateral soil-structure interaction can be modelled using empirically derived nonlinear uncoupled springs, so-called p-y curves, as boundary conditions in structural analysis. Hence the p-y method is based on soil being an elastoplastic material, see figure 1.2.

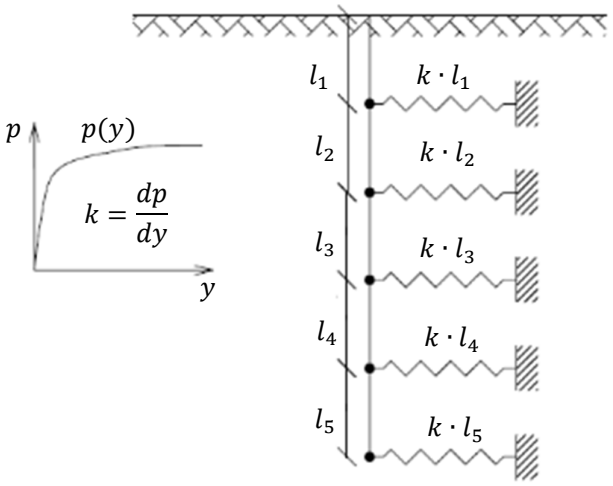

Figure 1.2: Illustration of p-y method. Here p is the soil resistance and y is the displacement.

Modelling of soil behaviour with springs was cf. [3] introduced by Winkler [4] in 1867. Hence, the principle is often referred to as a beam on nonlinear Winkler foundation.

According to [5], the concept of nonlinear p-y curves was first introduced by Reese and Matlock in 1956 and McClelland and Focht in 1958. Ever since, p-y curves have been an issue of discussion and regularly updated. Different methods of calculating the p-y curves are used for different types of soil and a distinction is made between sand, soft clay and stiff clay. In this project only the theory concerning p-y curves in sand is treated.

We are familiar with five formulations of p-y curves in sand. In the literature [5] these are referred to as methods A to E, see figure 1.3. The methods are shortly introduced below.

- **Method A**
  The p-y curve consists of two straight lines connected with a parabola. The method was introduced by Reese et al. [6] in 1974 and was incorporated in the API RP2A [U.1]. The ultimate soil resistance, p_u, is calculated from theory of wedge and flow failure, later described in section 1.2.1. An empirical adjustment factor, A, that differs for static and cyclic loading is also used. A varies with pile diameter and depth and forces p_u to match results from full scale tests on Mustang Island from 1967.

- **Method B**
  According to [5] Method B was presented in an unpublished report, [U.2], by Bogard and Matlock in 1980 among others. In principle the method B is the same as method A, but the expression of p_u, has been simplified.
- **Method C**
  Cf. [2] Scott presented the p-y curve as idealized by two straight lines in an API research report from 1980, [U.3]. The method, referred to as the bi-linear method, differs remarkably from the other definitions; especially as it never assumes a horizontal tangent.
- **Method D**
  Method D is the hyperbolic method and a continuous tangent hyperbolic function is used for the p-y curves. Cf. [5] the method was formulated by Parker and Reese in 1970, [U.4]. The ultimate soil resistance, p_u, was calculated from theory of wedge and flow failure as in method A and B, but the empirical adjustment factor A is given by a simplified expression. The principles of wedge and flow failure are described in section 1.2.1.
- **Method E**
  Method E was developed by O'Neill and Murchison in 1983. It is an extension of method D and it is referred to as the extended hyperbolic model. It differs from method D in:
  1. The simplified theoretical expressions for p_u from method B are adopted.
  2. A correction factor that applies to tapered and H shapes is included.

The principals of the five methods are illustrated in figure 1.3.

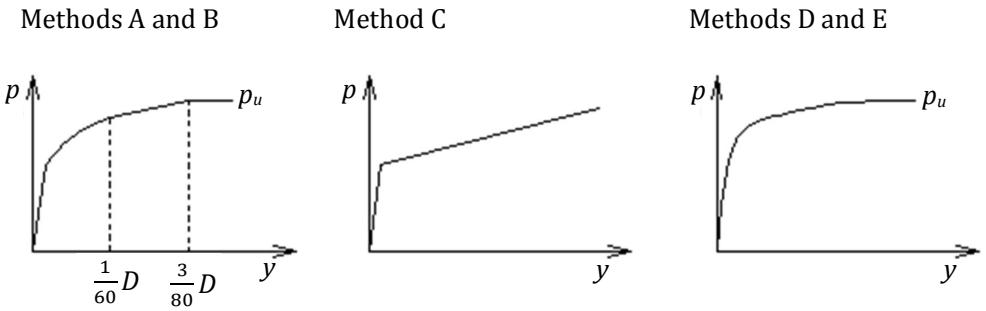

Figure 1.3: Sketching of the different p-y curves.

In the research report by O'Neill and Murchison from 1983 [5] results of these five different methods are compared with results from an experimental data base consisting of 15 full scale and laboratory tests. The database is presented in in table 1.1, cf. [5].

From the table the pile width and length can be read. The relation between width and length has to do with the pile slenderness. The slenderness ratios L/D vary from app. 27 – 48 with exception of the Bhushan piers, see figure 1.4, where the slenderness ratio is varying from app. 4.5 – 6. The results from the piers are not weighted as heavily as results from the other tests. The reason for this is that the pier response differed from that of a typical long pile.

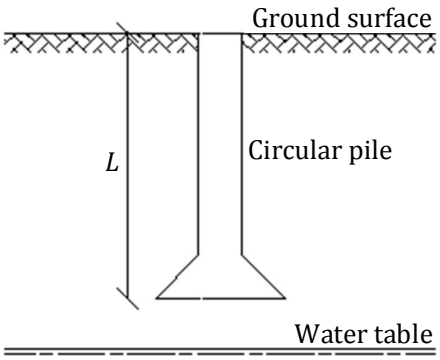

Figure 1.4: Sketching of Bhushan pier. The short pile is non-slender and has a big footing. [2] p. 69.

Monopiles used in wind turbine foundations are usually short and rigid with slenderness ratios of 5 to10, cf. [7] and section 2.2.
As can be seen from the table, the database is rather small and the database piles differ in size and material and the tests are not standardized.

Year	Test	type	pile	Avg. φ	Soil
1954	Mason-Bishop	Static	H-pile 0.4 m width 12.2 m long	35°	Medium sand, above WT
1964	Arkansas River	Static	Two steel pipes, 0.4 m diameter 16.2 m long	42°	Sand, below WT
		Cyclic	Concrete square pile, 0.51 m width 15.9 m long		
1964	Padre Island	Static	Steel pipe, 0.51 m diameter, 19.2 m long	37°	Medium sand, below WT
1967	Mustang Island	Cyclic Static	Steel pipe, 0.61 m diameter, 21 m long	38°	Sand with clay and sandy silt deposits, below WT
1971	Parker –Reese (Laboratory test-ing, small scale)	Static	Several steel pipes, 0.051 m diameter, 2.44 m long	40°	Medium sand below WT
1978-1979	Locks and Dam 26	Cyclic Static	Tapered timber 0.3 m (top), 13.7 m long		Medium sand, below WT
		Cyclic Static	H-pile 0.35 m width, 15.9 m long		Medium sand, below WT
1963-1979	Bhushan	Cyclic Static	Drilled pier, 0.9-1.2 m diameter, 5.5 m long	36°	Sand, above WT
1979	Robinson	Static	Tapered timber 0.3 m (top), 18.3 m long	34°	Sandy silt, below WT
1981	Leicht and Reese	Static	Concrete square pile, 0.35 m width, 9.5 m long.	23°	Sand, above WT

Table 1.1: Experimental database used in research report by O'Neill and Murchison, 1983 [5].WT = water table.

From the comparison O'Neill and Murchison concluded, that method E fits the experimental data the best and the p-y curves based on method E were adopted by the API.
From this it is clear that the recommended p-y curves are verified by comparison with piles that differ significantly in size and slenderness ratio from today's monopiles. Nevertheless, method E is recommended for designing offshore monopile foundation in the DNV [8].

1.2 Method E in detail

The expression for p-y curves in sand defined by method E is given in equation (1.1):

$$p = \eta \cdot A \cdot p_u \cdot \tanh\left(\frac{k \cdot z}{A \cdot p_u} \cdot y\right) \tag{1.1}$$

This formulation is the one presented in DNV [8] and API [9] with exception of the shape factor, η. This is due to the fact that $\eta = 1$ for circular cross sections. The value k represents the initial modulus of subgrade reaction and z is the depth below ground surface (GS). p_u is the ultimate bearing capacity, p is the resistance of the soil and y is the displacement of the pile in the considered level.
The initial modulus of subgrade reaction is usually determined from figure 1.5.

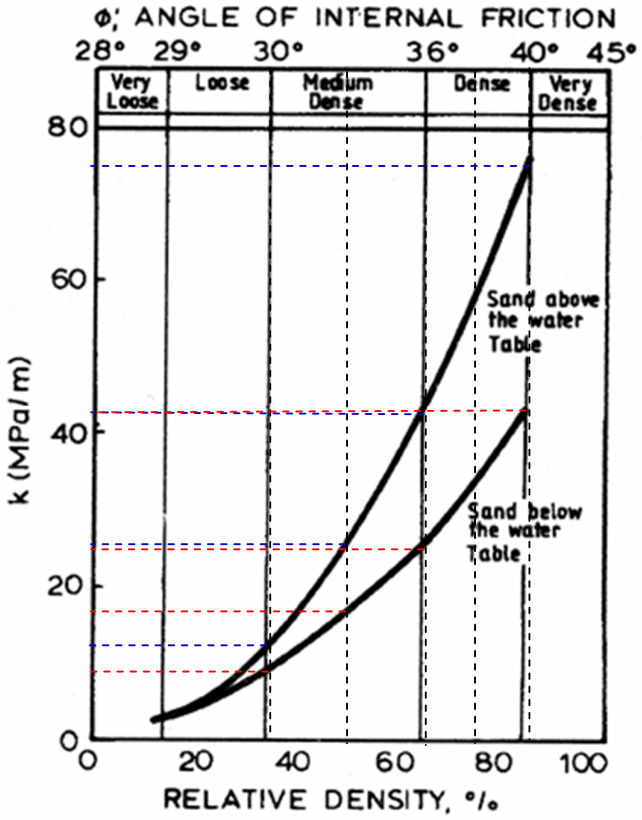

Figure 1.5: Variation of k with friction angle, cf. [8] appendix F. The points used for fitting k are shown.

As we intend to use the p-y curves in a computer program, this is not very efficient. Therefore power functions have been fitted to the curves, see figure 8.4.

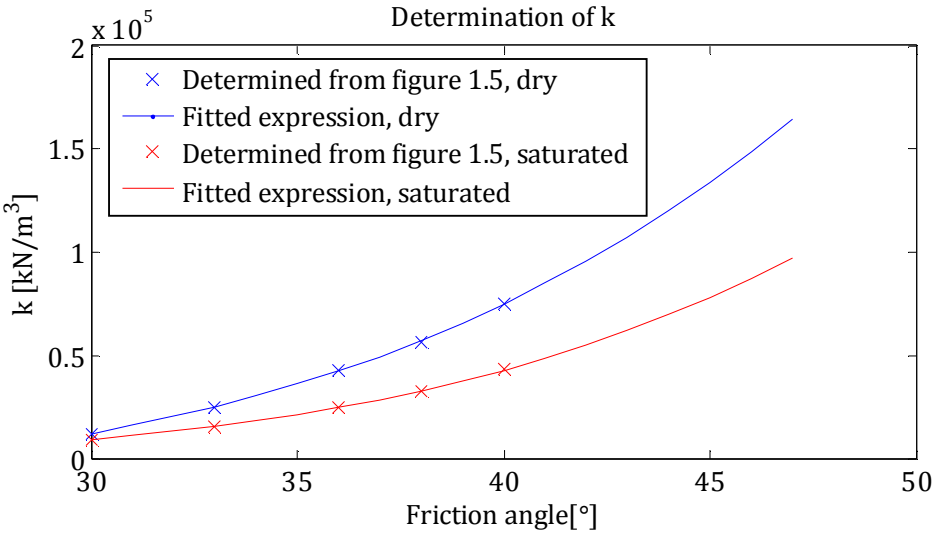

Figure 1.6: The fitted functions for k for dry and saturated sand. The fitting points are marked in figure 1.5.

For sand above the water table, k is therefore determined from:

$$k = 0.00829 \cdot \varphi^{4.384} - 12710 \tag{1.2}$$

For sand below water table, k is determined from:

$$k = 0.0005433 \cdot \varphi^{4.94} - 1663 \tag{1.3}$$

The ultimate soil resistance, p_u, is calculated from considerations of the type of failure that develops as a cylinder is moved laterally into a soil continuum, see section 1.2.1.
The empirical adjustment factor, A, depending on the depth below GS, z, and the pile diameter, D, is determined from equation (1.4):

$$A = \begin{cases} 3.0 - \dfrac{0.8 \cdot z}{D} \geq 0.9, \text{for static loading} \\ 0.9, \text{for cyclic loading} \end{cases} \tag{1.4}$$

1.2.1 Failure mechanisms

The methods A, B, D and E are basically the same and all methods use the concept of ultimate soil resistance, p_u. The expression for the ultimate soil resistance in frictional soils is based on considerations of a cylinder moving laterally into the soil without rotating, see figure 1.7.

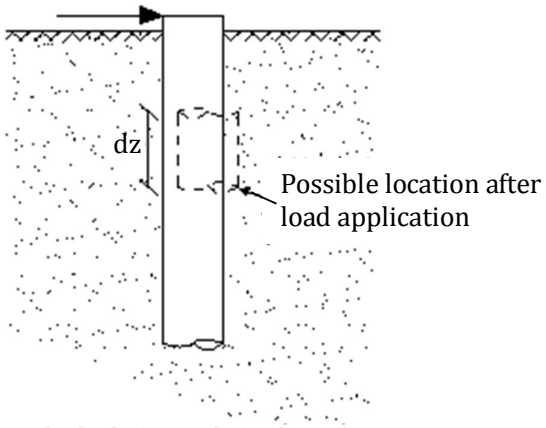

Figure 1.7: Cylinder before and after lateral movement.

The formulation of p_u given in the present API [9] is in accordance with method E and originates from the research report by O'Neill and Murchison [5] who reviewed an article by Reese from 1962 [U.5]. In the formulation, two types of soil resistance are assumed to exist. Near the ground surface and in moderate depths a passive wedge develops to resist the lateral movement of the pile, and in greater depths the soil moves horizontally around the pile. The two failure mechanisms are referred to as wedge failure and flow failure and are further explained in sections 1.2.1.1 and 1.2.1.2.

1.2.1.1 Wedge Failure

Near the ground surface and in moderate depths a failure wedge is assumed to occur when the load reaches the maximum capacity of the soil, and the ultimate resistance of the soil is then computed from this wedge. The assumed failure wedge is shown in figure 1.8.

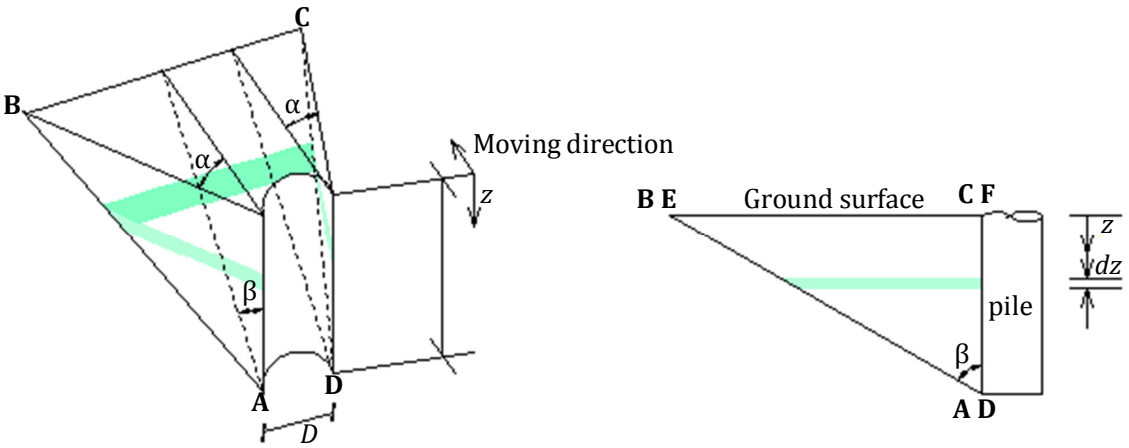

Figure 1.8: Assumed failure wedge, cf. [5].The green area is the considered differential area.

In figure 1.8 the angles α and β are given by equations (1.5) and (1.6):

$$\alpha = \frac{\varphi}{2} \tag{1.5}$$

$$\beta = 45° + \frac{\varphi}{2} \tag{1.6}$$

According to Gwizdala and Jacobsen [10], a lower bound solution assumes $\alpha = 0$ whereas an upper bound solution assumes $\alpha = \varphi$. Therefore, when using the value of α as given in equation (1.5) the wedge corresponds to something in between a lower bound and an upper bound solution for a smooth pile.

In wedge failure a mass of sand shaped as a wedge is pushed in front of the pile hence the planes ABC, DEF and ABED are failure planes and the Mohr-Coulomb failure criterion is used. Forces acting on a differential area, the green area sketched on figure 1.8, with height, dz, in the depth, z, are considered. Based on these considerations p_u is determined from equation (1.7):

$$p_u = (C_1 z + C_2 D)\gamma' z \tag{1.7}$$

In equation (1.7) D is the pile diameter and γ' is the effective soil weight. C_1 and C_2 are coefficients determined from considerations of the wedge. Traditionally these coefficients are determined from graphs [9] to simplify the calculation of the p-y curves, but in [5] they are given by expressions, see equations (1.8) and (1.9):

$$C_1 = \frac{K_0 \tan\varphi \sin\beta}{\tan(\beta-\varphi)\cos\alpha} + \frac{\tan^2\beta \tan\alpha}{\tan(\beta-\varphi)} + K_0 \tan\beta\,(\tan\varphi \sin\beta - \tan\alpha) \quad (1.8)$$

$$C_2 = \frac{\tan\beta}{\tan(\beta-\varphi)} - \tan^2(45° - \alpha) \quad (1.9)$$

In equations (1.8) and (1.9), φ is the angle of internal friction. K_0 is the earth pressure coefficient at rest. K_0 varies with φ but in equation (1.8) and (1.9) it is taken as a constant, $K_0 = 0.4$. The considered wedge has sharp edges; which contradicts field conditions, where the failure surfaces will be curved.

1.2.1.2 Flow failure

At some depth below the surface, it requires less work for the soil to move horizontally around the pile instead of moving upwards in a wedge. This type of failure is referred to as flow failure, see figure 1.9.

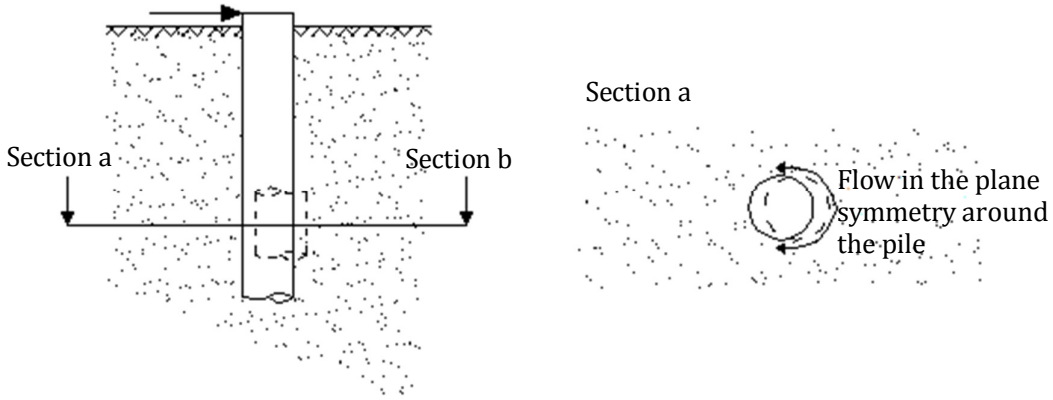

Figure 1.9: Flow failure.

The ultimate bearing capacity for horizontal flow failure is given in equation (1.10).

$$p_u = C_3 D \gamma' z \quad (1.10)$$

Where

$$C_3 = 0.4 \tan\varphi \tan^4\beta + \tan^2(45° - \alpha)\,(\tan^8\beta - 1) \quad (1.11)$$

1.3 Limitations of the p-y approach

Due to its simplicity the p-y method generally provides results easy and fast compared to more advanced 3D models and the offshore standards, API [9] and DNV [8] still recommend the use of p-y curves for describing pile-soil interaction.

The API and DNV recommendations are based on a limited amount of field and laboratory tests where most of the tested piles differ from piles used for offshore wind turbine foundations in size and slenderness, see section 1.1.

Lately concerns related to the p-y curves and the p-y method are growing. In the DNV from 2007 [8] this is expressed in a guidance note, see quotation 1.1 and in the API supplement 3 from 2008 [9] it is outlined, that the p-y method is intended as a guideline only.

Therefore offshore engineers argue whether results based on the p-y method are reliable. If this is not the case there is a risk of underestimating the pile displacement to a given force, which for

some constructions can be devastating. Furthermore the boundary conditions need to be modelled correctly in order to determine the system frequencies, which are of great interest when handling dynamically loaded structures.

> **402** Caution must be exercised when the recommended nonlinear p-y curves are used in other contexts than for evaluation of lateral pile capacity in the ULS. Such contexts include, but are not limited to, SLS analysis of the pile, ***determination of equivalent spring stiffnesses to represent the stiffness of the pile-soil system as boundary condition in analyses of the structure that the pile-soil system supports***, and in general all cases where the initial slope of the p-y curves may have an impact.
>
> **403** Caution must be exercised regardless of whether the recommended nonlinear p-y curves are applied directly as they are specified on closed form or whether piece-wise linear approximations according to some discretisation of the curves are applied.

Quotation 1.1: cf. [8] p. 127. The part of the warning that concerns the p-y method is emphasized.

1.4 Research areas

With a view towards developing efficient engineering methods for static and dynamic analysis of the pile foundations for offshore wind turbines a lot of research has been made within the last decades.

The research is concerned with investigating the opportunities of establishing efficient 3D models and with investigating the p-y method and the recommended p-y curves.

Today the opportunity of using advanced finite element method, which allows application of soil constitutive modelling and soil-pile nonlinear interaction, exists and cannot be neglected. Leading companies are using three dimensional finite element modelling in offshore foundation design, among others the Danish company GEO, [2].

Regarding the p-y curves some of the main points of interest are according to DONG Energy [W.4] to:

- Investigate the definition of initial stiffness of the recommended p-y curves.
  This is primarily concerned with investigating a potential diameter effect.

- Investigate effects of cyclic loading

Using the recommended p-y curves the initial stiffness of the soil in a given depth is independent of the pile diameter, see figure 1.10. This might seem surprisingly, but Terzaghi 1955, [11] approves this. The validation of the recommended p-y curves relies on a small experimental data base and the method has to some extend been calibrated to the data.

Probably no problem exists taking the initial stiffness as a constant for piles of similar diameter as the database piles, but nowadays piles are about 10 times wider than the reference piles described in table 1.1. An uncertainty whether this leads to a scale effect not accounted for in the recommended p-y curves exists. Therefore research in this area continues.

Among others Ashford and Juirnarongrit 2003, [12] and a group of graduate students at Aalborg University [13] recently investigated the subject. Asford and Juirnarongrit refer to studies made in the 1980'es by Carter and Ling, [U.6], [U.7], where the modulus of subgrade reaction is con-

cluded linearly proportional to the pile diameter. Themselves however having found the modulus of subgrade reaction independent of pile diameter. The graduate students found that the initial modulus of subgrade reaction is highly dependent on the pile diameter by numerical analysis and laboratory experiments.

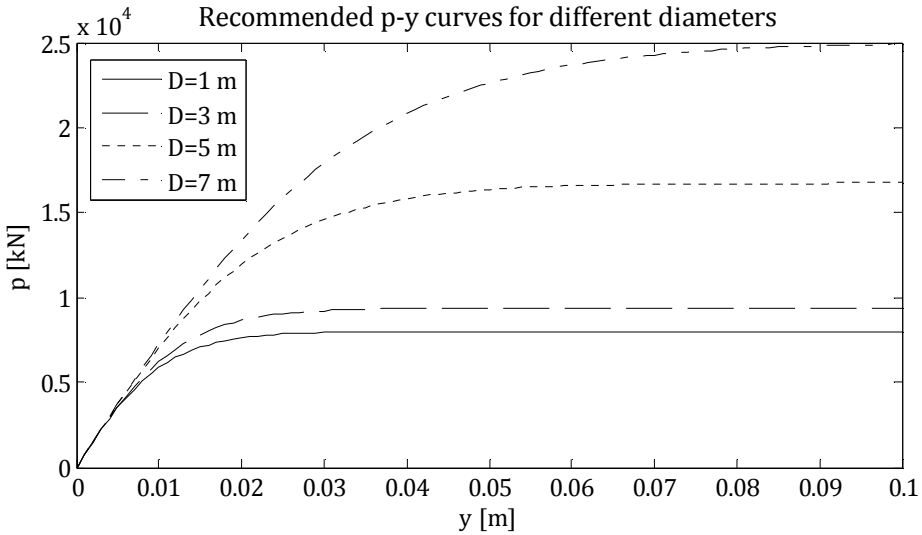

Figure 1.10: P-y curves based on API [9] for different diameters. φ=40°, γ=17.54 kN/m³ and z=10 m.

Until very recently it has been believed, that a dynamic load case would cause a decrease in soil strength and stiffness in the upper soil layers, see figure 1.11. This behaviour is accounted for in the recommended p-y curves by the empirical factor, *A*, in the p-y curve formulation, se equations (1.1) and (1.4), p. 5.

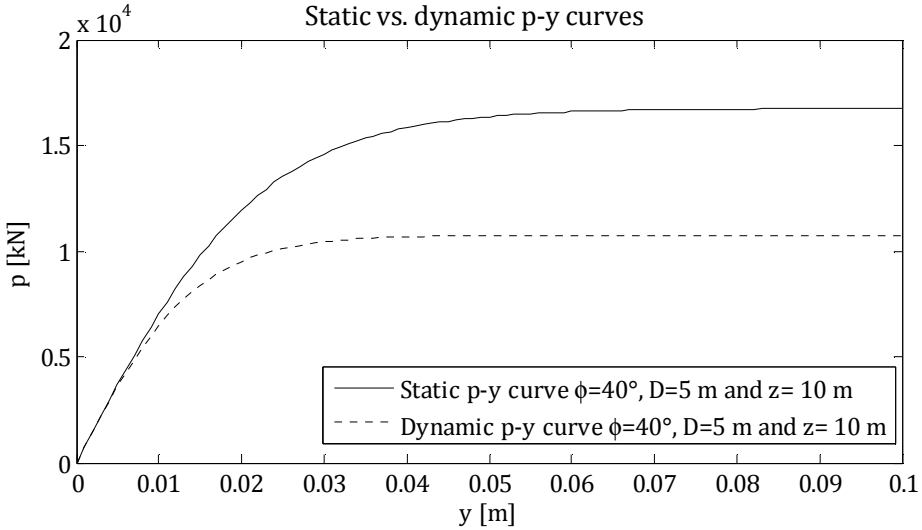

Figure 1.11: Static vs. dynamic p-y curves after API [9]. φ=40°, γ=17.54 kN/m³ and z=10 m.

From equation (1.4) p. 6 it is seen that dynamic p-y curves are independent of loading frequency, number of cycles etc. Some articles question this current methodology. For instance Klinkvort et al. from 2010 [14] were an increase in secant stiffness due to cyclic loading was found in connection with centrifuge testing of a rigid pile in dry sand. Another article from 2010 by LeBlanc et al. [7] describes a similar tendency also found from experimental work with a rigid pile in dry sand.

1.5 Scope of this report

Clearly more research needs to be done on both the above described topics.
In this project the effect of cyclic loading is experimentally examined. Failure estimate of soil stiffness leads to failure estimate of the construction frequencies. Both over- and underestimating the soil stiffness will be a problem in relation to dynamic analyses.
Since monopiles are often used in offshore foundation this project is concerned with cyclic testing of a rigid pile in both dry and saturated sand. It is furthermore investigated whether loading frequency has an impact on the soil conditions.
Static testing of the same pile in both dry and saturated sand is performed after the cyclic loading. Therefore following experiments are carried out:

- pile experiments with cyclic horizontal load for three different frequencies in dry sand
- pile experiments with cyclic horizontal load for maintained frequency in saturated sand
- pile experiments with static horizontal loading immediately after cyclic experiments in disturbed soil conditions.

As reference also static experiments in dry and saturated sand for undisturbed soil conditions are conducted:

- pile experiments with static horizontal load in dry and saturated sand for undisturbed soil conditions

With a view towards investigating the principle of the p-y method following experiments are carried out:

- p-y experiments in dry sand

The results of the p-y experiments are compared to the theoretical p-y curves hereby discussing the shape of the theoretical p-y curves. In MATLAB a 2D beam model is established. The model is supported by nonlinear springs, a so-called beam on nonlinear Winkler foundation. The p-y curves obtained from experiments are used defining the nonlinear springs. The results from the program are compared to results of pile experiments with static load, hereby evaluating the principle of the p-y method.

Also, we find it interesting to work with 3D modelling of the problem. At Aalborg University a numerical material model based on Mohr Coulomb's failure criterion has been developed by Clausen et al [15]. In the present project this model is applied in Abaqus to establish a 3D finite element model.
Plaxis 3D foundation is a commonly used finite element program in geotechnical engineering. Therefore a model is also established in this program. The Abaqus model is based on associated plasticity whereas the Plaxis 3D model is based on non associated plasticity.

- 3D modelling using Abaqus with user defined soil model (associated plasticity).
- 3D modelling using Plaxis 3D foundation with integrated soil model (non associated plasticity).

The main reasons for working with the two models are to highlight qualities and disadvantages and compare to laboratory results.

2 Experimental planning

The research performed in this project considers three different types of experiments:

- P-y experiments
- Static pile experiments
- Cyclic pile experiments

All experiments are related to each other. The static and cyclic pile experiments are performed using the same scale pile and the p-y experiments are carried out with a piece of the scale pile profile.

2.1 Soil domain

As soil domain a rectangular box filled with sand is used. The same box is used in connection with all three types of experiments. It is chosen to use dense sand in the experiments with relative density, $I_D = 0.84$.

The type of sand used is Esbjerg sand. The sand characteristics are accounted for in an in house unpublished article by Krabbenhøft et al [16], see table 2.1.

Parameter	Value
Relative density in tests	0.84
Dry unit weight in tests [kN/m³]	17.54
D_{50} [mm]	0.50
Specific density, $d_s = \frac{\gamma_s}{\gamma_{water}}$	2.621
Maximum void ratio, e_{max}	0.733
Minimum void ratio, e_{min}	0.449

Table 2.1: Characteristics of Esbjerg Sand. γ_{water} is set to be 10 kN/m^3 in [16].

2.1.1 Preparation of soil domain

The box has to be emptied and filled by hand before each test. To secure a homogenous relative density within the box, sand is filled in layer by layer and compressed with a weight for each 5 cm, see figure 2.1. Same procedure for all types of testing is used.

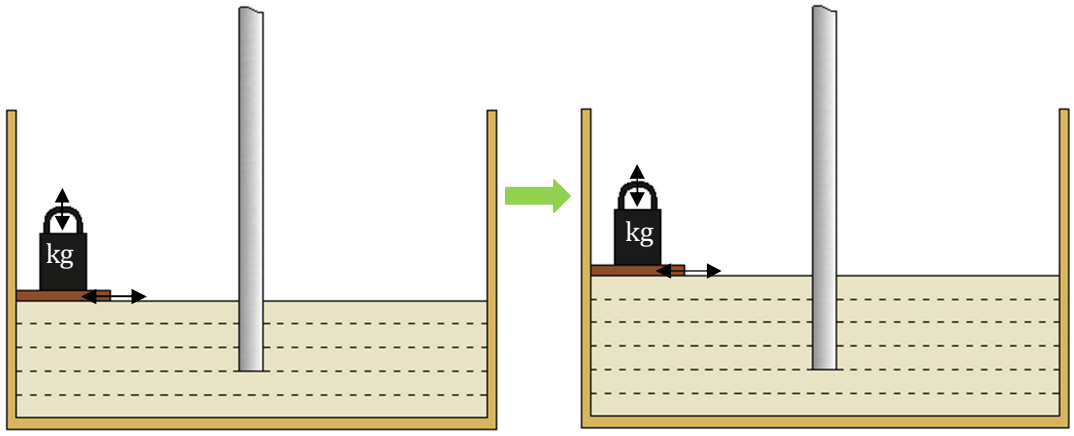

Figure 2.1: Preparation of the soil domain.

With regard to the preparation time the box cannot be too big. Dimensions are chosen as follows: length 1.000 m, width 0.500 m and height 0.6500 m, leaving 10-15 cm in the top making compressing easier and preventing water from overflowing in connection with saturation. With a relative density of 0.84 the sand weighs 17.54 kN/m³.

The amount of sand for each layer is:

$$m_{sand,layer} = 17540\frac{\mathrm{N}}{\mathrm{m}^3} \cdot 0.05\ \mathrm{m} \cdot 0.5\ \mathrm{m} \cdot 1\ \mathrm{m} \cdot \frac{1}{9.82\frac{\mathrm{N}}{\mathrm{kg}}} = 44.654\ \mathrm{kg} \tag{2.1}$$

From equation (2.1) it is seen that each layer must consist of 44.654 kg sand to secure the wanted relative density. The sand is weighed using a weight with an accuracy of 0.001 kg. The sand is filled into small buckets with approximately 20 kg in each. To fill the box completely 25 buckets are needed. This procedure causes a negligible error of ± 0.050 kg.

Deformation of the sides of the box due to earth pressure has effectively been prevented by stabilizing with steel beams so the box volume is not expanding during compressing. It has been controlled that the box does not expand by measuring the distance between the edges before and after filling the box.

In connection with the pile experiments no sand is filled into the pile, therefore a reduction is made corresponding to the submerged pile volume.

$$m_{reduction} = 17540\frac{\mathrm{N}}{\mathrm{m}^3} \cdot \frac{0.0508^2}{4}\ \mathrm{m}^2 \cdot \pi \cdot 0.4\ \mathrm{m} \cdot \frac{1}{9.82\frac{\mathrm{N}}{\mathrm{kg}}} = 1.460\ \mathrm{kg} \tag{2.2}$$

Therefore the total amount of sand to be filled into the box for the pile tests is:

$$m_{pile\_experiments} = 10 \cdot 44.654\ \mathrm{kg} - 1.460\ \mathrm{kg} = 445.080\ \mathrm{kg} \tag{2.3}$$

For the tests in dry sand the sand is weighed one time, and between the tests the sand is filled back into the buckets. From this procedure there is some waste. After finishing the last pile experiment the sand left had a total weight of 444.418 kg, so the total waste is 0.662 kg through all the tests in dry sand.

Relative density is calculated from equation (2.4).

$$I_D = \frac{e_{max} - e}{e_{max} - e_{min}} \tag{2.4}$$

Here e is the actual void ratio which can be calculated from equation (2.5):

$$e = \frac{V_p}{V_s} \tag{2.5}$$

In equation (2.5) v_p is the pore volume and v_s is the soil volume.
The soil and pore volumes with the minimum assessed amount of sand in the box and the maximum height of the ground surface are determined from:

$$v_{s,lower} = \frac{m_{soil,min}}{d_s \cdot \frac{\gamma_w}{9{,}82\ N/kg}} = \frac{445.080\ \mathrm{kg} - 0.662\ \mathrm{kg} - 0.050\ \mathrm{kg}}{2.621 \cdot \frac{10{,}000\ \mathrm{N/m^3}}{9.82\ \mathrm{N/kg}}} = 0.1665\ \mathrm{m}^3 \tag{2.6}$$

$$\begin{aligned} V_{p,max} &= V_{box} - V_{pile} - V_{s,lower} \\ &= 0.5 \cdot 0.502 \cdot 1\ \mathrm{m}^3 - \frac{0.0508^2}{4}\mathrm{m}^2 \cdot \pi \cdot 0.4\ \mathrm{m} - 0.1665\ \mathrm{m}^3 = 0.0837\ \mathrm{m}^3 \end{aligned} \tag{2.7}$$

The soil and pore volumes with the maximum assessed amount of sand in the box and the minimum height of the ground surface are determined from:

$$v_{s,upper} = \frac{m_{soil,max}}{d_s \cdot \frac{\gamma_w}{9{,}82\ N/kg}} = \frac{445.080\ \text{kg} + 0.050\ \text{kg}}{2.621 \cdot \frac{10{,}000\ \text{N/m}^3}{9.82\ \text{N/kg}}} = 0.1668\ \text{m}^3 \tag{2.8}$$

$$V_{p,min} = V_{box} - V_{pile} - V_{s,upper} = 0.5 \cdot 0.498 \cdot 1\ \text{m}^3 - \frac{0.0508^2}{4}\text{m}^2 \cdot \pi \cdot 0.4\ \text{m} - 0.1668\ \text{m}^3 = 0.0814\ \text{m}^3 \tag{2.9}$$

Hence the minimum and maximum relative densities are expected to be:

$$I_{D,min} = \frac{e_{max} - \frac{V_{p,max}}{V_{s,lower}}}{e_{max} - e_{min}} = \frac{0.733 - \frac{0.0837}{0.1665}}{0.733 - 0.449} = 0.8109 \tag{2.10}$$

$$I_{D,max} = \frac{e_{max} - \frac{V_{p,min}}{V_{s,upper}}}{e_{max} - e_{min}} = \frac{0.733 - \frac{0.0814}{0.1668}}{0.733 - 0.449} = 0.8626 \tag{2.11}$$

From these considerations the average relative density is believed to vary within the interval of [0.8109 ; 0.8626] which is very acceptable.

In some of the tests the sand is saturated. The saturated tests are performed after completion of all dry tests (both p-y, static and cyclic tests in dry sand). In connection with the saturated tests the sand is replaced from time to time. The sand is filled in exactly as described in the dry tests. With a garden hose water is filled in from the bottom afterwards. Water is filled in, so that the waterline is placed in level +0.05 above GS, see figure 2.2, and a test is not performed before a period of 1 h. This is to secure complete saturation.

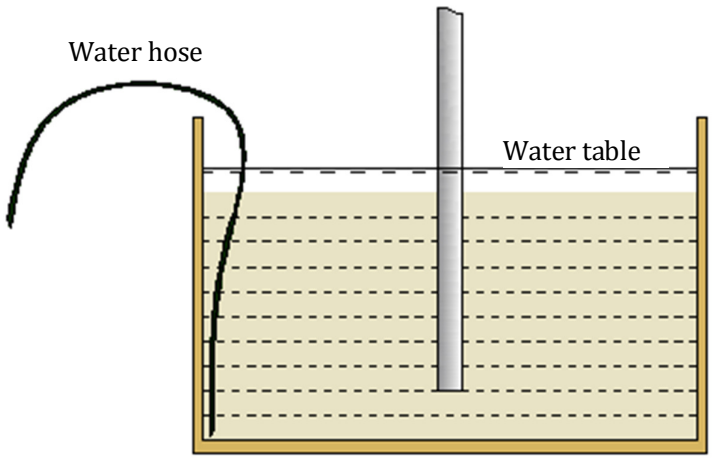

Figure 2.2: Saturation of soil domain.

The saturated density of the sand is determined by the values in table 2.1. First, the void ratio, *e*, is determined as:

$$I_D = \frac{e_{max} - e}{e_{max} - e_{min}} \Longrightarrow e = e_{max} - I_D \cdot (e_{max} - e_{min}) \tag{2.12}$$

The void ratio is

$$e = 0.733 - 0.84 \cdot (0.733 - 0.449) = 0.4944 \tag{2.13}$$

The saturated density, γ_s, of the sand is determined as:

$$\gamma_s = \frac{d_s + e}{1 + e} \cdot \gamma_w \tag{2.14}$$

Where:

d_s is the specific density
γ_w is the density of water

The saturated density is:

$$\gamma_s = \frac{2.621 + 0.4944}{1 + 0.4944} \cdot 10\frac{kN}{m^2} = 20.85\frac{kN}{m^2} \tag{2.15}$$

2.1.2 Friction angle

Sand is a granular material. In an article [17] from 2007 Cerato and Lutenegger discuss scale effects in such materials and friction angle dependency on stress level is mentioned as a scale effect. The association between internal friction angle and stress level for Esbjerg sand has been determined from triaxial tests with variable confining pressures, σ_3, ranging from 1.5 kPa to 100 kPa. The results are accounted for in [16]. In the triaxial testing σ_1 is increased until failure meanwhile the corresponding axial strain is registered. In figure 2.3 a sketching of some test results from triaxial tests with Esbjerg sand are shown.

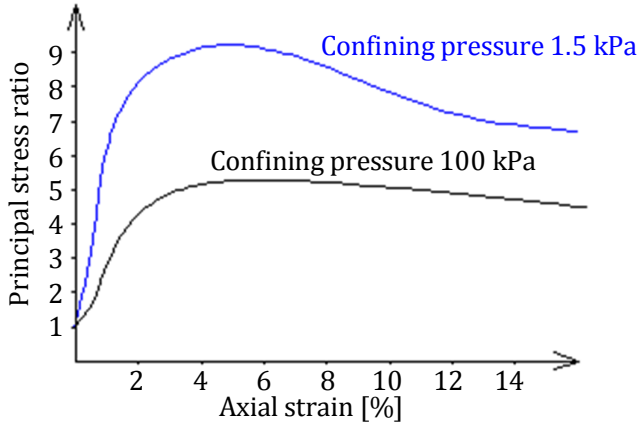

Figure 2.3: Sketching of some test results for Esbjerg sand – I_d = 0.84, cf. [16]

The principal stress ratio is defined as shown in equation (2.16).

$$principal\ stress\ ratio = \frac{\sigma_1}{\sigma_3} \tag{2.16}$$

$$\left(\frac{\sigma_1}{\sigma_3}\right)_{max} = \frac{1 + \sin(\varphi_{peak})}{1 - \sin(\varphi_{peak})} \tag{2.17}$$

The point of maximum principal stress is the failure point. From the Mohr's circle or from equation (2.17) the peak friction angle can be determined. This is illustrated in figure 2.4 for a confining pressure of 1.5 kPa or 100 kPa.

From figure 2.3 and equation (2.16) σ_1 in failure for a confining pressure of 1.5 kPa is determined to be approximately 13.5 kPa hence the failure envelope is 53.3°. For a confining pressure of 100 kPa, σ_1 in failure is determined to be approximately 500 kPa. Hence the failure envelope is 41.3°.

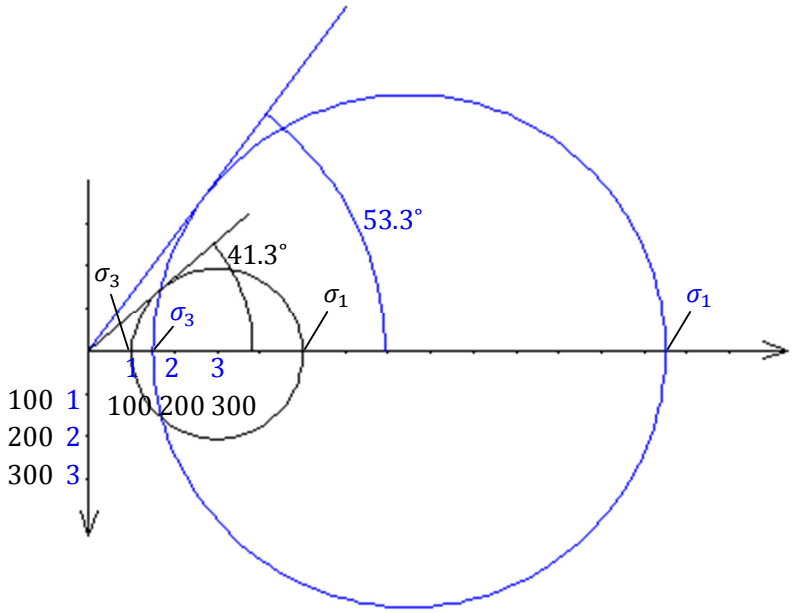

Figure 2.4: Determination of peak friction angle. Black circle corresponds to black axis values and confining pressure 100 kPa. Blue circle corresponds to blue axis values and confining pressure 1.5kPa.

The failure envelope is referred to as the peak friction angle, φ_{peak}.
The dilatation angle is also determined from experimental results. According to [16] there are several different suggestions of how to calculate the dilatation angle, but the data presented in [16] is based on the formula presented in equation (2.18):

$$\sin\psi_{max} = \left(-\frac{d\varepsilon_1 + 2d\varepsilon_3}{d\varepsilon_1 - 2d\varepsilon_3}\right)_{max} \tag{2.18}$$

In many cases failure theories are based on associated plasticity theory. In associated plasticity the friction angle and the dilatation angle are equal. This leads to an overestimate of the bearing capacity if using the peak friction angle. To avoid this overestimate of bearing capacity a modified friction angle is determined.

The modified friction angle, φ_{mod}, is in [16] determined from equation (2.19).

$$\tan\varphi_{mod} = \frac{\sin\varphi\cos\psi}{1 - \sin\varphi\sin\psi} \tag{2.19}$$

In table 2.2 the results of the triaxial tests with relative density 0.84 are shown.

Confining pressure, $\boldsymbol{\sigma_3}$	Relative density, $\boldsymbol{I_D = 0.84}$	Peak friction angle, $\boldsymbol{\varphi_{peak}}$	Dilatation angle, $\boldsymbol{\psi_{max}}$	Modified peak friction angle, $\boldsymbol{\varphi_{mod}}$
1.5 kPa	0.84	53.3°	* 23.0°	47.0°
5.3 kPa	0.84	48.6°	18.3°	43.0°
20 kPa	0.84	46.1°	15.5°	40.1°
50 kPa	0.84	42.4°	14.8°	38.7°
100 kPa	0.84	41.3°	13.7°	37.6°

Table 2.2: Test results for Esbjerg sand, *estimated value, cf. [16].

In this project small scale tests are performed in a box with a depth of 0.65. In the p-y experiments the maximum depth of the sand is 0.55 m. With a relative density of 0.84 the effective soil weight is 17.54 kN/m³, this means that the pressure varies from 0 kPa in the top layer to 9.65 kPa in the bottom. To determine φ_{peak}, ψ_{max} and φ_{mod} in the considered depths, functions have been fitted to the data from table 2.2, see figure 2.5.

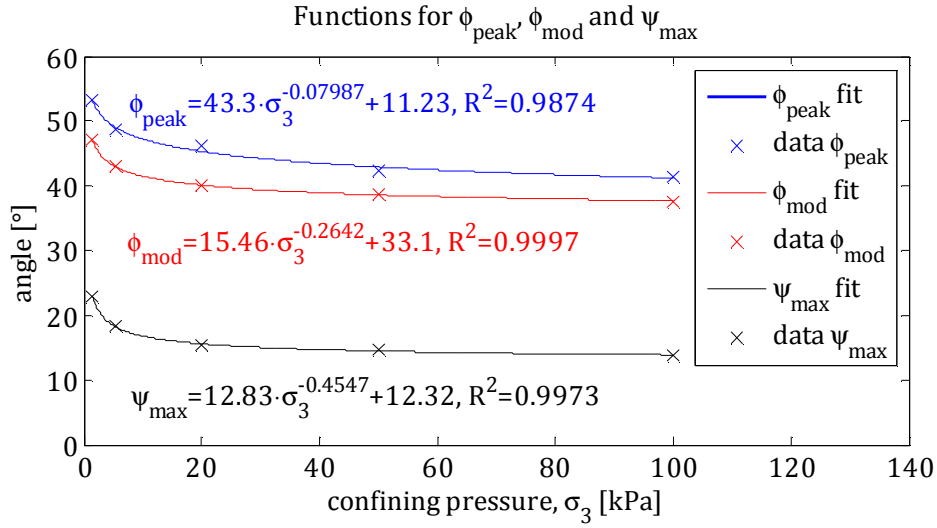

Figure 2.5: Fitted functions for φ_{peak}, ψ_{max} and φ_{mod}.

For greater stress levels, the friction- and dilatation angles do not depend on the size of σ_3. However in the considered depths there is a strong dependency when no outer pressure is applied. Consequently this scale effect cannot be neglected but is expected to have an impact on the test results. In figure 2.6 the variation of φ_{peak}, ψ_{max} and φ_{mod} with depth is shown. It is chosen not to use values that exceed the maximum values from the triaxial tests.

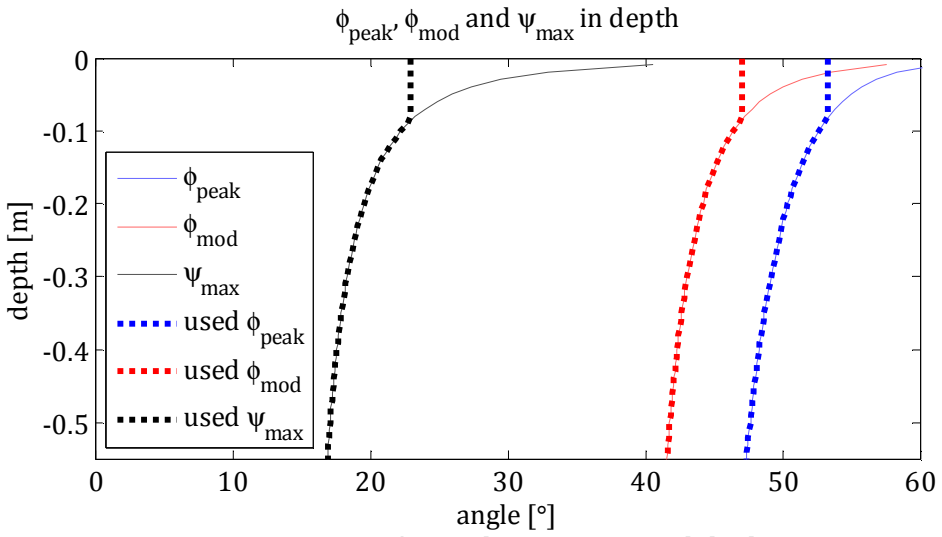

Figure 2.6: φ_{peak}, ψ_{max} and φ_{mod} variation with depth.

2.2 Scale pile

A proper pile profile must be chosen as scale pile. In order to make the scale pile somewhat realistic, the dimensions of the pile profile are chosen based on the dimensions of a typical offshore wind turbine supported by a monopile foundation.

On Horns Rev II all wind turbines are supported by monopiles. The wind turbines on Horns Rev II have a height from sea level to blade centre of approximately 68 meters. An additional 30-40 meters are below sea level. The monopiles have a diameter of 3.9 meters and a length of 30-40 meters. That is slenderness ratio of approximately 8-10.

The chosen scale is 1:75 resulting in the dimensions listed in table 2.3.

	Height above mudline	Depth below mudline	Pile diameter
Full scale	68 m + 30 m = 98 m	30 m	3.9 m
Small scale	1.30 m	0.40 m	0.052 m

Table 2.3: Primary scale model dimensions.

The chosen profile is a round tube from Sanistål, Sani nr. 395541. The profile has an outer diameter of $D = 0.0508$ m and a thickness of $s = 1.5$ mm, see figure 2.7.

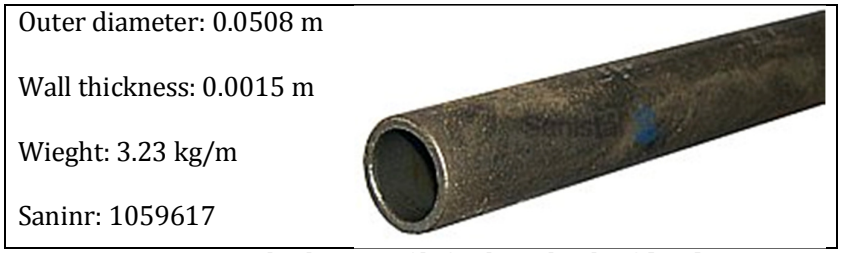

Figure 2.7: The chosen profile for the scale pile, cf. [W.7].

Cerato and Lutenegger mention another scale effect regarding particle size in the article [9]. Studies performed with circular footings indicate that by using the ratio $B/d_{50} > 50$ to 100 the particle size effect can be avoided. The average grain size, d_{50} is for Esbjerg sand 0.50 mm. [16]

$$\frac{B}{d_{50}} = \frac{0.0508\ \text{m}}{0.005\ \text{m}} = 102 \tag{2.20}$$

From equation (2.20) no particle size effect is expected. The profile is chosen to be open ended. The wall thickness of the profile however does not comply with the ratio which can lead to some problems.

2.2.1 Control of the pile dimensions

In this section a control of the pile cross section is made in order to make sure that no plastic deformations of the pile will occur during the experiments.
The expected maximum moment in the pile is determined by using the p-y curves from API, see section 1.2 p.5, in a nonlinear Winkler model, see section 6.4 p. 52.
The ultimate resistance of the pile is determined to be 127 N and the bending moment at this load is 173 Nm. The theoretical p-y curves are determined from modified friction angles.

The stress determined from the calculated moment is:

$$\sigma = \frac{M_{max}}{W_{pile}} = \frac{173\ Nm}{\frac{\pi}{32} \cdot \frac{D^4 - d^4}{D}} = \frac{173\ Nm}{\frac{\pi}{32} \cdot \frac{(0.0508\ m)^4 - (0.0478\ m)^4}{0.0508\ m}} = 62\ Mpa \tag{2.21}$$

The yield strength of the steel is 235 MPa. This means that the bending moment can be more than three times as large as expected before plastic deformations occur. Therefore the strength of the profile is concluded to be sufficient.
However the wall thickness is rather small and therefore it is examined whether local folding can occur in the pile. The cross section class is calculated according to [18]:

$$\frac{D_{pæl}}{t} = \frac{0.0508\,mm}{0.0015\,mm} = 34 < 50 \cdot \sqrt{\frac{235}{f_y}} = 50 \tag{2.22}$$

This means that the cross section is a cross section class 1 which means that local folding will not occur before yield.
During the experiments the submerged part of the pile will be subjected to large pressures from the soil. In appendix A it has been examined that these pressures do not induce plastic ovalization of the pile. The examination is made in Abaqus with a model of the pile segment used in the p-y experiments as this is expected to undergo the largest soil pressures. The model is loaded with a uniformly distributed load. The load is placed on a cape of an elastic material with very small stiffness which encloses the pile segment. The p-y curve at a depth of 0.45 m shows a maximum load of 20,000 N/m. This divided with the width of 0.0508 m gives a distributed load on the cape of about $4 \cdot 10^5$ N/m^2. The stresses in the pile section are shown in figure 2.8.

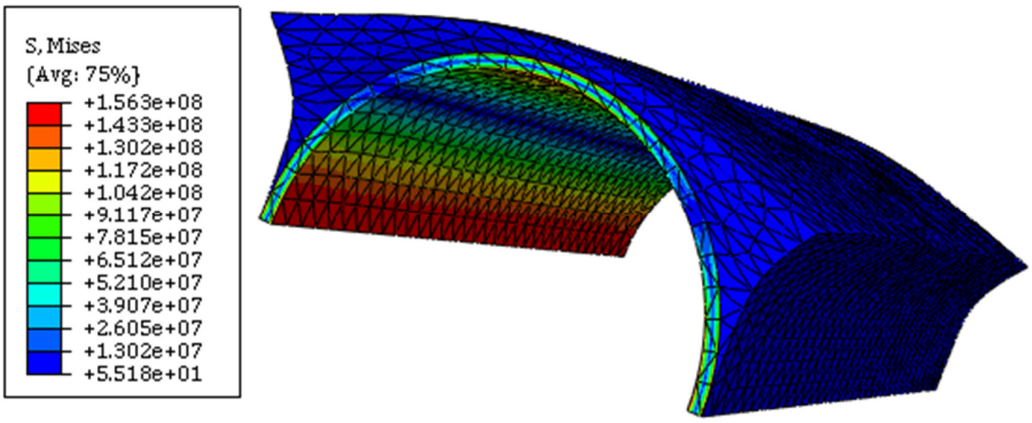

Figure 2.8: Von Mises stresses after solving the model.

The figure shows that the largest stress in the pile section is 156 MPa which is significantly less than the yield strength of the pile of 235 MPa.

The final cross section of the pile is shown in figure 2.9.

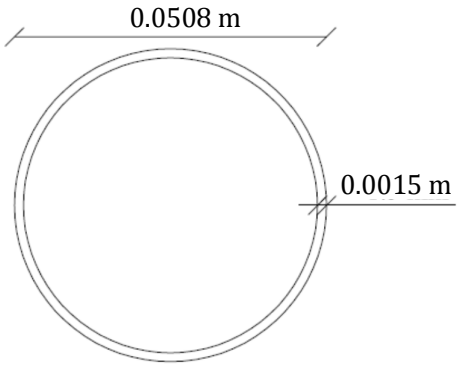

Figure 2.9: Cross section dimensions for the chosen profile.

3 P-y experiments

The p-y experiments have the following two purposes:

- Determination of experimental p-y curves to represent the stiffness of the soil in a 2D Winkler model, established in MATLAB.
- Discussion of the shape of the p-y curves by direct comparison of experimental p-y curves to theoretical p-y curves from method E.

3.1 Experimental setup for p-y experiments

The test setup for the p-y experiments is shown in figure 3.1. The test subject has a height of 0.1 m and the same cross sectional dimensions and surface as the pile used for the static and cyclic pile experiments.
During the p-y experiments the test subject is pushed horizontally trough the sand by the hydraulic piston, while connected values of load and displacement are measured. The displacements are measured in two points and the average of the two displacements is used. The force is measured by a force transducer placed behind the hydraulic piston. The travel of the piston has a maximum displacement of 0.03 m.

The test subject is placed 0.1 m above the bottom of the box and the box is filled with sand until e has the desired value. Tests are conducted with four different values of e: $e = 0.1$ m, $e = 0.2$ m, $e = 0.3$ m and $e = 0.4$ m.

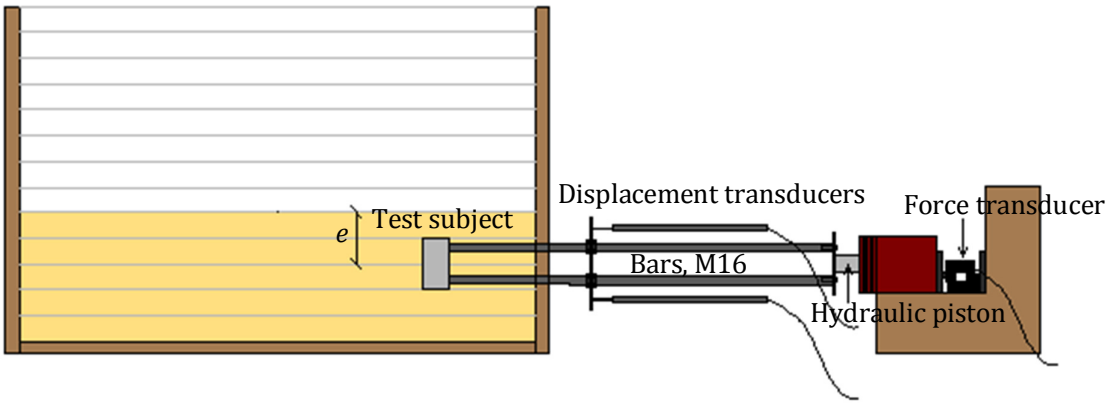

Figure 3.1: Test setup for the p-y tests.

3.2 Sources of the error for p-y experiments

In this section the sources of errors and uncertainties for the p-y experiments are evaluated.

3.2.1 Compactness of sand

The method of compacting the sand for the tests is a definite source of error, as the compactness and the homogeneity of the sand can vary from test to test. In section 2.1.1 the uncertainty concerning the average relative density of the soil domain is estimated to vary within the interval of [0.8109 ; 0.8626].

3.2.2 Measuring of force

The force transducer is placed behind the hydraulic piston which yields uncertainties due to the friction between the piston and its base. Friction between the bars and the holes in the box where the bars go through is also a concern. These uncertainties are estimated to have no significant effect on the results. The hydraulic piston has been activated with no sand in the box and the force varies from 0-10 N in this situation.

3.2.3 Measuring of displacements

In the p-y experiments the displacements are measured in two points outside of the box - one point below the centre of the test subject and one point above the centre of the test subject. The average of these two displacements is assumed to be the displacement at the midpoint of the test subject. The only uncertainty in measuring the displacements is the uncertainty of the displacement transducers which is small and assumed negligible.

3.2.4 Experimental setup

The test subject has a height of 0.1 m and is supposed to represent a point on the pile for the static experiments. It is an error that the sand is able to move above and below the test subject as this is not possible for a point on the pile in the static experiments.

3.2.5 Friction between end surfaces

The friction between the end surfaces of the test subject and the sand gives a false addition to the measured force. The size of this addition is estimated in appendix B and is negligible.

3.3 Expectations for p-y experiment

The expected ultimate resistances in the four p-y experiments are determined as the horizontal tangent of the theoretical p-y curves determined at the depth, *e*, multiplied with the height of the test subject. These ultimate resistances are shown in table 3.1.

Depth from soil surface to centre of test subject, *e* [m]	Expected ultimate resistance [N]
0.1	278
0.2	519
0.3	997
0.4	1595

Table 3.1: Expected ultimate resistance of the test subject for the four different depths.

3.4 Results of p-y experiments

The results of the p-y experiments are shown in figure 3.2 to figure 3.5. The experiments are repeated three times in order to determine average curves.
The displayed results are edited. As the loading speed varies from test to test it is not possible to determine the average curves unless the results are edited. The results for every 1/10 mm are used in the edited curves. The unedited results are shown in appendix C.

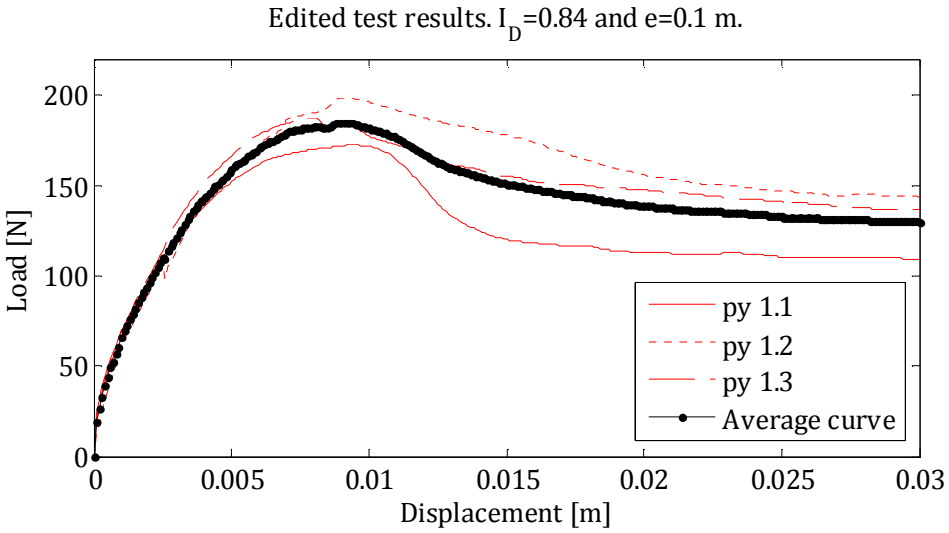

Figure 3.2: Edited test results for p-y experiments with a depth of 0.1 m to the centre of the test subject.

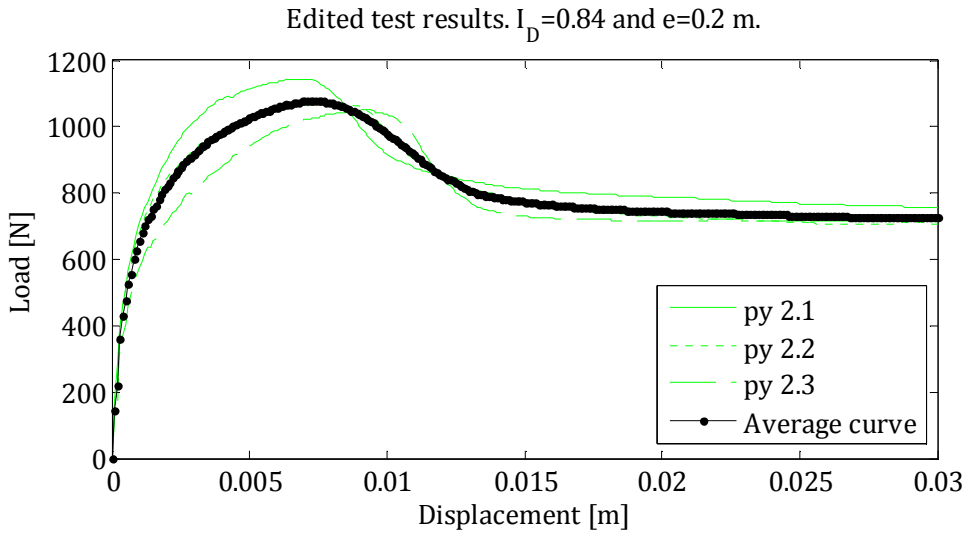

Figure 3.3: Edited test results for p-y experiments with a depth of 0.2 m to the centre of the test subject.

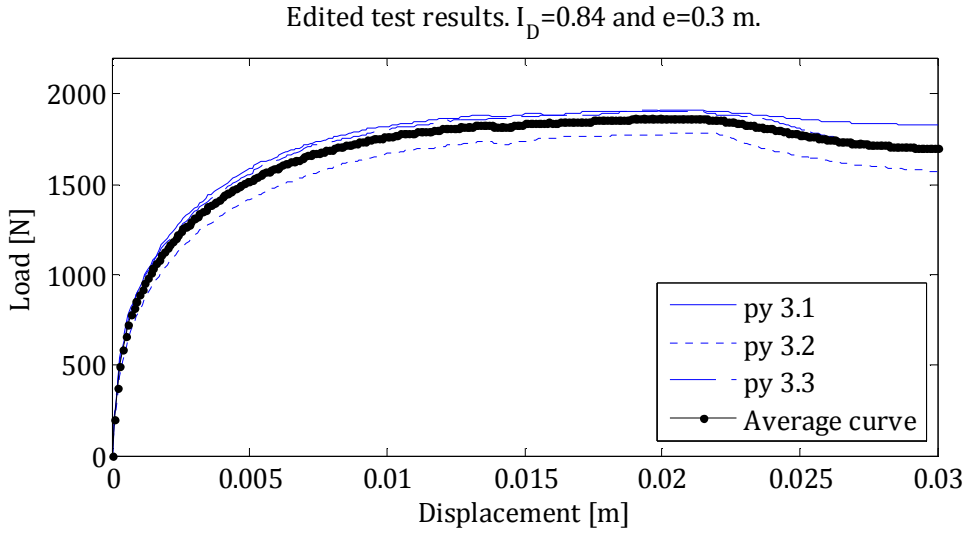

Figure 3.4: Edited test results for p-y experiments with a depth of 0.3 m to the centre of the test subject.

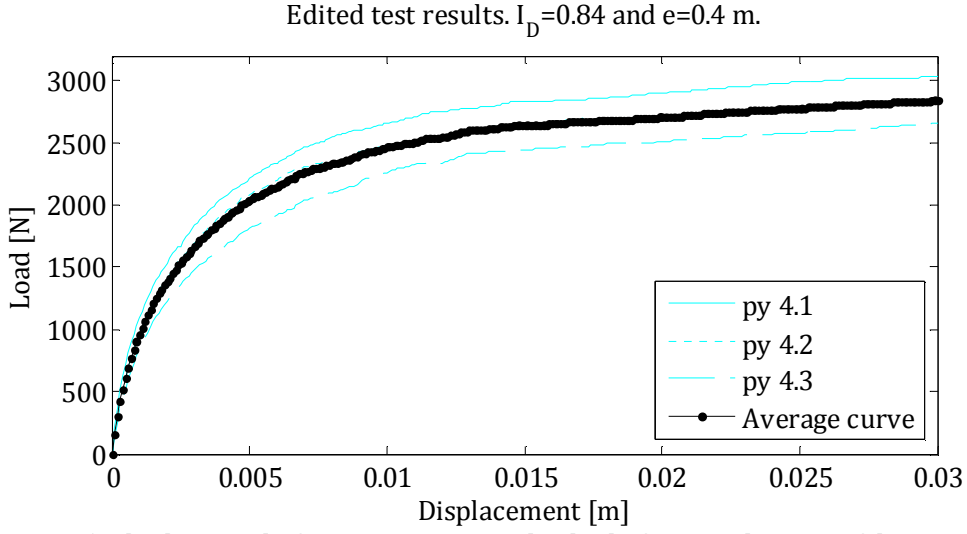

Figure 3.5: Edited test results for p-y experiments with a depth of 0.4 m to the centre of the test subject.

Figure 3.2 to figure 3.5 shows the same tendency in the three repetitions for all depths. For e = 0.1 m the peak force varies about 20 % from the highest to the lowest. For the rest of the depths this variation is 6-13 %. Therefore the results of the p-y experiments are considered reliable.

3.5 Evaluation of p-y experiments

The measured results presented in section 3.4 are expressions of the connection between the displacement of the test subject and the strength of the soil that the test subject displaces. In general the p-y curves are desired to be described in a single point. Consequently the average experimental curves are divided with height of the test subject, see figure 3.6.

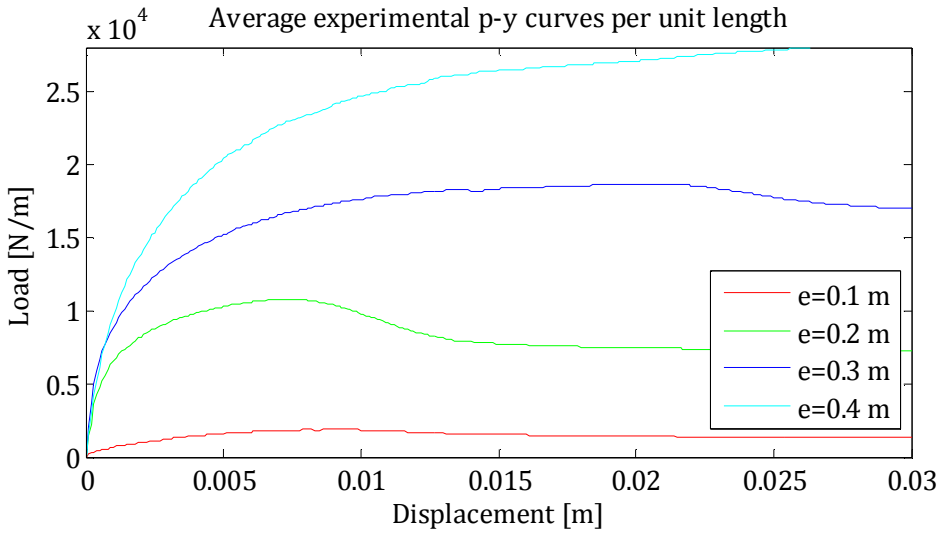

Figure 3.6: Average experimental p-y curves divided by the length of the test subject.

The figure shows that the larger the overburden pressure is the larger the ultimate resistance is. The displacement at which the ultimate resistance is reached also increases in general with the overburden pressure.
The experimental ultimate resistances compared to the expected are shown in table 3.2.

	Experimental ultimate resistance [N]	**Theoretical ultimate resistance [N]**
$\boldsymbol{e = 0.1\ m}$	185	278
$\boldsymbol{e = 0.2\ m}$	1050	519
$\boldsymbol{e = 0.3\ m}$	1800	997
$\boldsymbol{e = 0.4\ m}$	2800	1595

Table 3.2: Comparison of the ultimate resistance determined in the experiments and by the theoretical p-y curves.

The table shows that for e = 0.1 m the theoretical ultimate resistance is too large compared to the experiments. For the rest of the depths the experimental ultimate resistance is almost twice the size of the ultimate resistance of the theoretical curves.
Figure 3.7 to figure 3.10 shows the experimental and theoretical p-y curves for each of the four examined depths. Adjusted theoretical curves are also shown in the figures. These are determined by adjusting the initial modulus, k, so that the initial stiffness fits the experimental curves and the empirical adjustment factor, A, is adjusted so that the ultimate resistance fits.

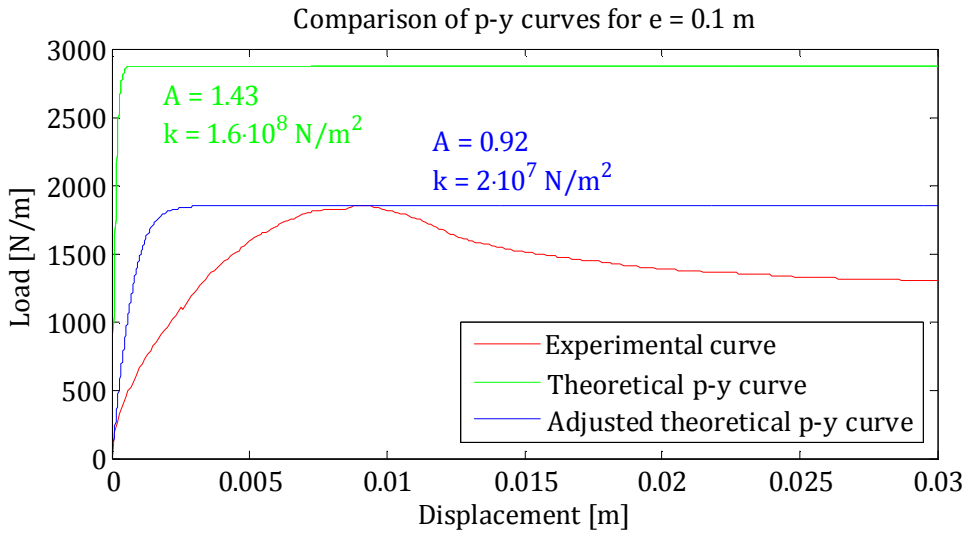

Figure 3.7: Comparison of p-y curves for e = 0.1 m.

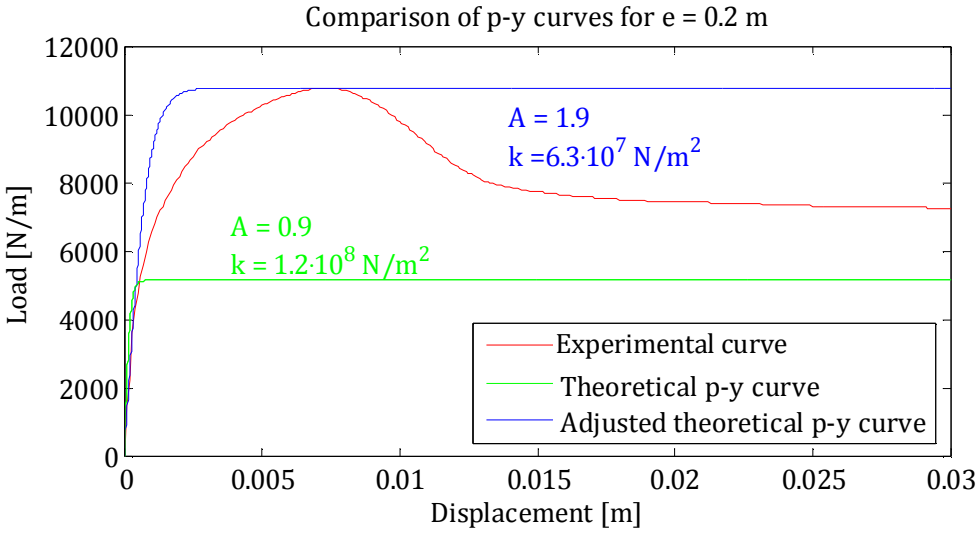

Figure 3.8: Comparison of p-y curves for e = 0.2 m.

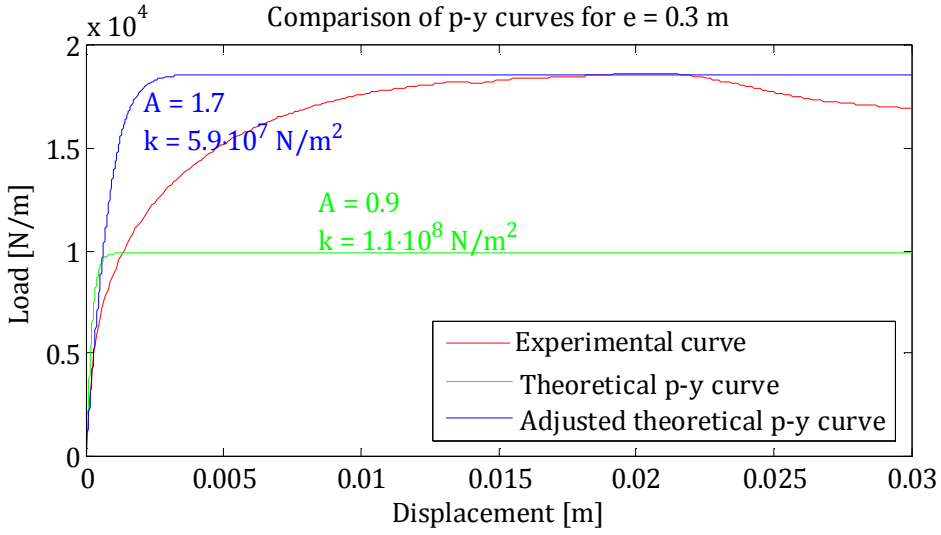

Figure 3.9: Comparison of p-y curves for e = 0.3 m.

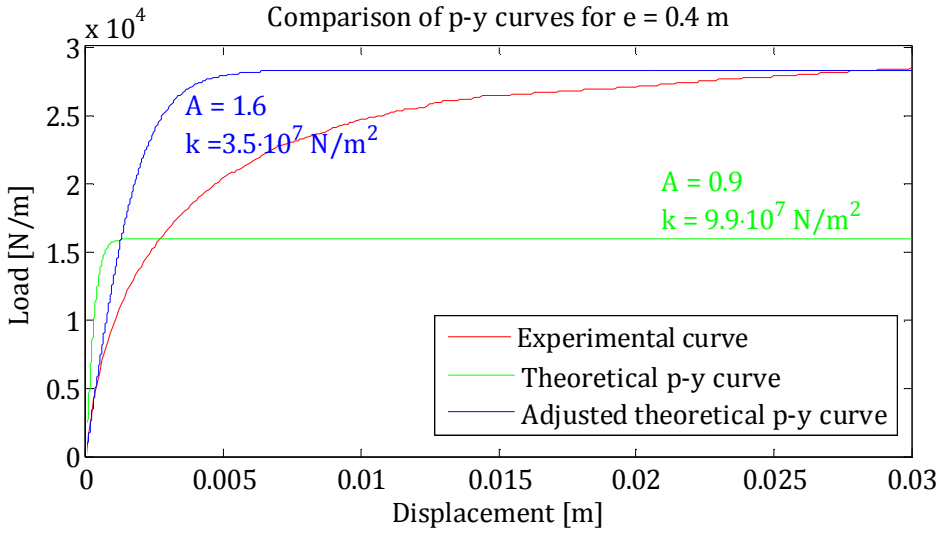

Figure 3.10: Comparison of p-y curves for e = 0.4 m.

The conclusion of the comparison is that there is a big difference between the shape, the initial stiffness and the ultimate resistance in the theoretical and experimental curves.
When the experimental curves are to be used in the beam program it is necessary to have functions to represent the curves. Therefore functions are fitted to the experimental curves. The curves should intersect the axes in (0,0), consequently a linear curve is fitted to the first part of the curves and a number of exponential functions are fitted to the rest. For example the fitted curve for e = 0.1 m is shown in figure 3.11. The rest of the fitted curves are shown in appendix D.

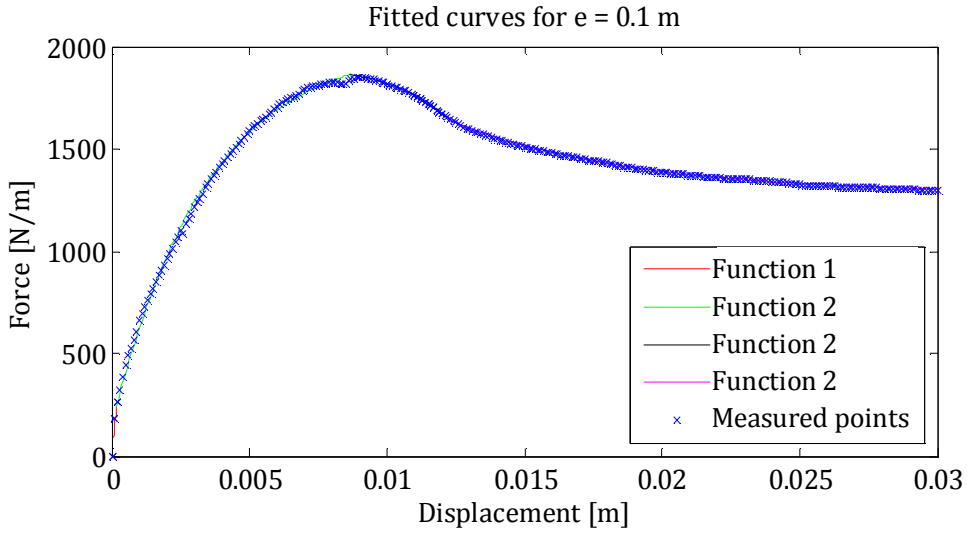

Figure 3.11: Fitted p-y curve for e = 0.1 m.

The expression for the fitted curve in figure 3.11 is:

$$p(y) = \begin{cases} 1.449996 \cdot 10^6 \cdot y & for\ 0 < y < 0.0001653 \\ 2009.13 - 1857.36 \cdot e^{-293.8 \cdot y} & for\ 0.0001653 \leq y < 0.008658 \\ 1907.95 - 0.60 \cdot e^{497.9 \cdot y} & for\ 0.008658 \leq y < 0.01224 \\ 1278.66 + 2315.60 \cdot e^{-150.4 \cdot y} & for\ 0.001224 \leq y \end{cases}$$

4 Static experiments

The static experiments have two primary purposes:

- Determining static load-displacement curves for comparison with nonlinear Winkler model and 3D solid models.
- Examining the effects of cyclic loading on the initial stiffness and ultimate resistance for dry and saturated sand.

The static pile experiments are listed in table 4.1. Most of the static tests are performed immediately after a cyclic test to obtain the changes in soil properties towards a static load due to a cyclic load. As reference, a number of static tests in undisturbed soil conditions are performed. Static tests performed after preceding cyclic tests are referred to with sc, whereas static tests performed in undisturbed domains are referred to with index s. The number of the static tests performed after a cyclic test is in accordance with the number of the preceding cyclic test. Cyclic experiments are described in section 5.

Test	Foundation depth	Instrumentation (Instr.)	Preceding cyclic test	Frequency [Hz]
Pile experiments static horizontal load on dry sands				
s.0.1	0.40 m	Fully instr.*	No	-
s.0.2	0.40 m	Fully instr.**	No	-
sc.1.1	0.389 m	No instr.	Yes	0.27
sc.1.2	0.390 m	No instr.	Yes	0.27
sc.1.3	0.387 m	No instr.	Yes	0.27
sc.2.1	0.394 m	No instr.	Yes	0.56
sc.2.2	0.395 m	No instr.	Yes	0.56
sc.3.1	0.380 m	No instr.	Yes	0.84
sc.3.2	0.395 m	No instr.	Yes	0.84
Pile experiments with static horizontal load on saturated sands				
sc.4.1	0.413 m	No instr.	Yes	0.27
sc.4.2	0.412 m	No instr.	Yes	0.27
s.0.3	0.40 m	Fully instr.**	No	-
s.0.4	0.40 m	Fully instr.**	No	-

Table 4.1: Overview of the 3 different Static pile experiments. Fully instrumented pile has strain gauges mounted. (*) Strain gauges in level -0.3 to -0.1 are out of order. (**) The strain gauge in level -0.3 is discarded, but the rest are fully functional.

From table 4.1 it shows that the foundation depth is not the same in all static tests. The reason for this is the vertical displacement of the pile during the cyclic tests as described in section 5.2.4. The results presented in this report are adjusted so they can be compared as if the foundation depth where 0.4 m in all tests. The adjustment method is described in appendix E.

4.1 Experimental setup for static experiments

The experimental setup for the static tests is shown in figure 4.1. The force is measured at the top of the pile with a force transducer and the displacements are measured at the top of the pile and at the soil surface.

The pile is loaded by turning the crank handle on which a cord is attached. The cord goes from the crank handle over the shaft and is attached to the pile. The crank handle is very long, which makes it easy to apply the load in a slow and steady pace.

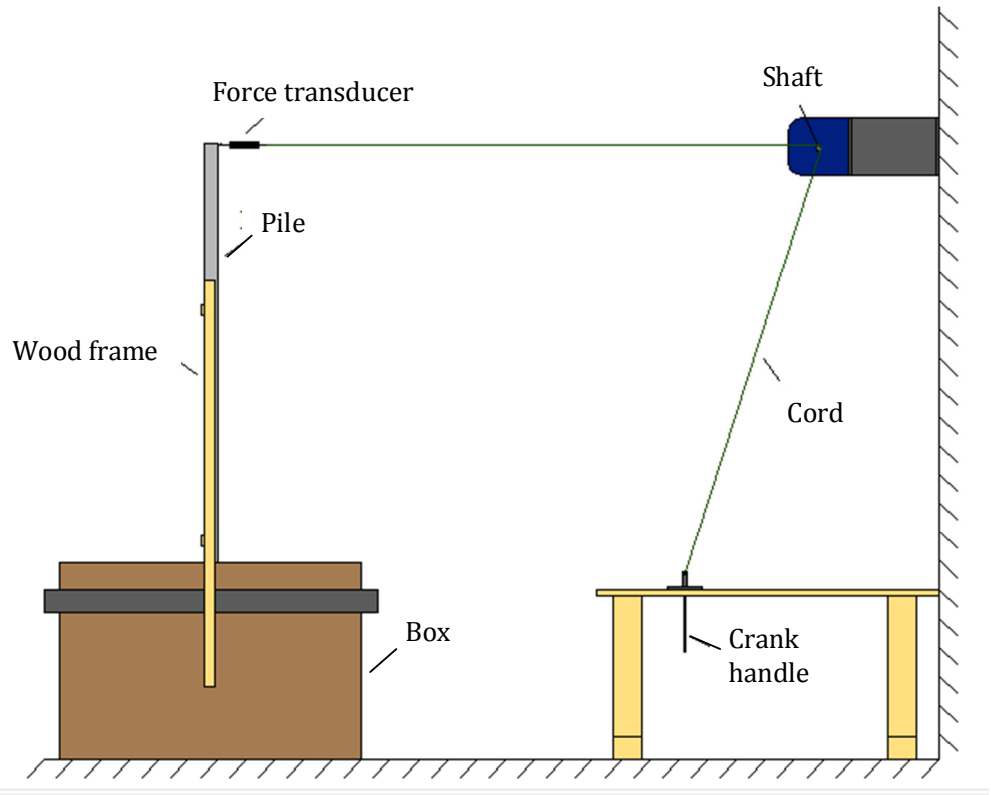

Figure 4.1: Experimental setup for static experiments.

The pile is fastened to the wood frame using clamps. After installing the pile, the box is filled with sand until the desired density is attained. The method of sand compacting is described in section 2.1.1.

Strain gauges are mounted per 5 cm on the lower part of the pile, see figure 4.2. The strain gauges are attached to the pile with special glue. Strain gauge and wires are soldered together and the wires are fixed to the pile with epoxy glue to protect the soldering.

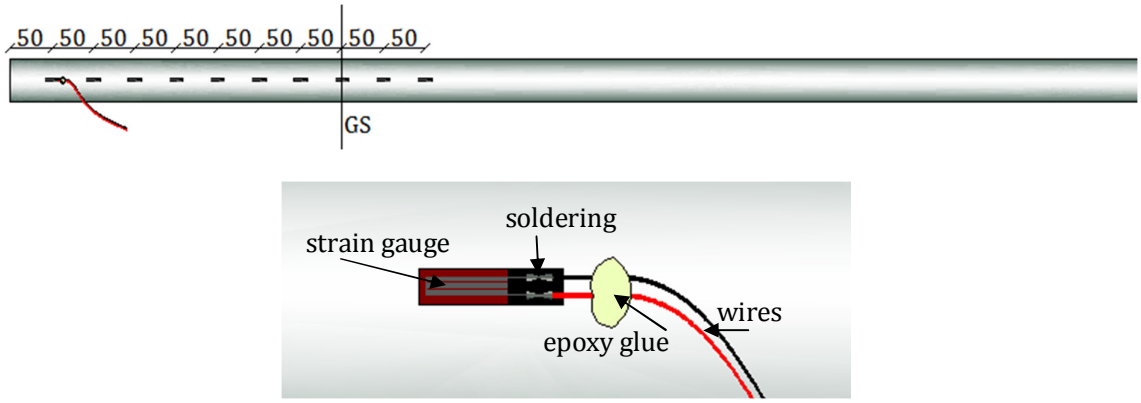

Figure 4.2: Strain gauge position and mounting.

Single strain gauges are used and they are placed in the loading direction. In appendix F it is shown, that the signal from single strain gauges is sufficient to determine the distribution of bending moment in the pile. One strain gauge is installed in the ground surface and two are placed above the ground surface. The bending moments in these three points are known from

theoretical solutions and therefore the functionality of the strain gauges can be controlled for each experiment by using these three strain gauges.

During the static experiments the displacements are measured in two points. At the top of the pile where the load is applied the displacements are measured using a wire displacement transducer and at the ground surface the displacements are measured using a laser displacement transducer. The exact locations of the displacement transducers are shown in figure 4.3.

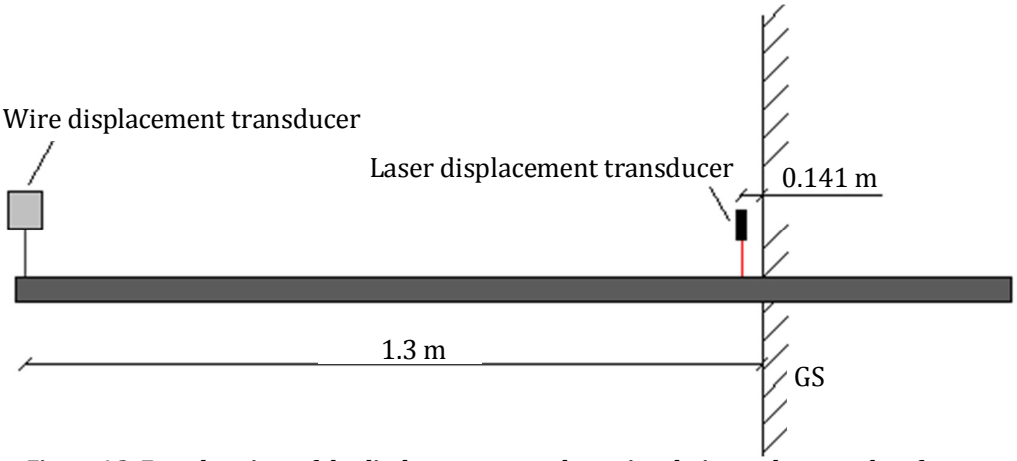

Figure 4.3: Exact locations of the displacement transducers in relation to the ground surface.

4.2 Sources of the error for static experiments

In this section the sources of errors and uncertainties for the static tests are evaluated.

4.2.1 Compactness of sand

The method of compacting the sand for the tests is a definite source of error, as the compactness and the homogeneity of the sand can vary from test to test. In section 2.1.1 the uncertainty concerning the average relative density of the soil domain is estimated to vary within the interval of [0.8109 ; 0.8626].

4.2.2 Measuring of force

The pile is loaded until the ultimate resistance of the soil is reached and therefore the displacement at the top of the pile will be rather large. This will entail that the load will be applied at an oblique angle. Therefore the box is placed with some distance to the engine shaft in order to reduce the angle of obliqueness. The box is placed 2.0 m from the engine shaft. In appendix G it is determined that at a displacement of the pile top of 0.5 m the horizontal component of the force equals 99.87 % of the total force. It is therefore assessed that the obliqueness can be considered negligible when the pile is placed 2.0 m from the engine shaft.
The displacement transducer at the top of the pile is a wire transducer. The wire provides some resistance when it is pulled. This means that the force transducer will measure this resistance as well as the resistance from the soil. It has been established that the resistance force varies from 0-4 N, which is considered negligible compared to the soil resistance.

4.2.3 Measuring of displacements

The displacements are measured at the soil surface with a laser displacement transducer. The laser measures in the same level during the entire test. This means that the point on the pile, in which the displacement is measured, moves upward when the pile is subjected to horizontal displacement. The error of this is estimated in appendix G to be 2.7 % at a measured displacement of 0.1 m.

The displacement at the top of the pile is measured using a wire displacement transducer. The wire is connected to the top of the pile, which means that the displacement is measured in the same point of the pile during the entire test. The spool of the wire transducer does not move downward during the tests but the top of the pile does when the displacement is large. This means that the wire will be drawn in an oblique angle. This is in appendix G estimated to result in a measured displacement that differs about 1.2 % from the horizontal displacement of the pile at a displacement of 0.5 m.
The errors in measuring the displacements are considered negligible compared to the inaccuracies of the displacement transducers themselves.

4.2.4 Strain gauges

In the static experiments 10 strain gauges are installed on the pile. They are installed on the back side of the pile to avoid them being subjected to large pressure from the soil.
As mentioned, three strain gauges are placed above the ground surface in order to control the functionality during the experiments. Therefore the accuracy of the strain gauges is evaluated after the tests. In appendix F it has been accounted for that a misplacement of the strain gauges of 5 mm to the sides causes an error of -0.1 %.

4.3 Results of static experiments

The results of the static experiments with cyclic loading are normalized in relation to the foundation depths at the time of the execution of the static experiment. The method for normalization is described in appendix E.

4.3.1 Load-displacement curves

The load-displacement curves from the static experiments are shown in figure 4.4 and figure 4.6. In the figures the repetitions of the experiments are represented with similar colours. It is seen that the curves for the repetitions for the tests in both dry and saturated sand are very similar, which verifies the test setup and to a large extend the preparation of the soil domain.

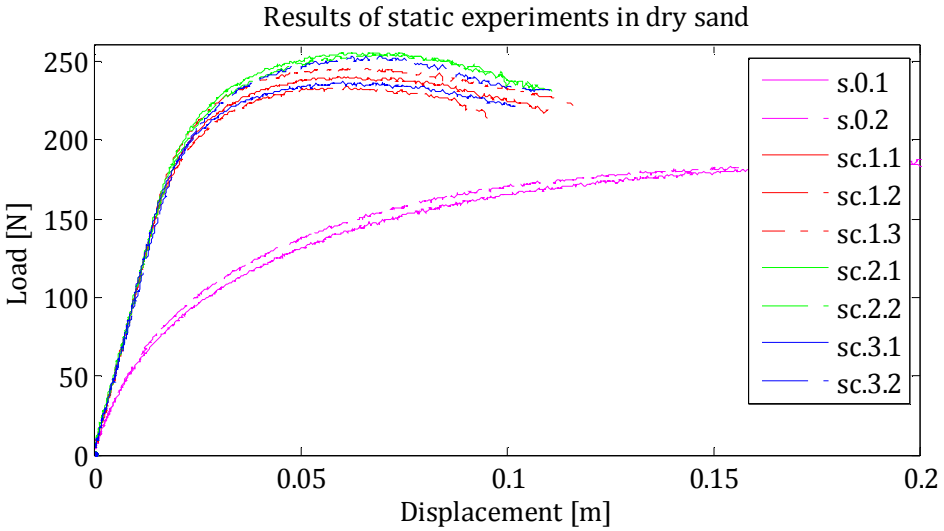

Figure 4.4: Load-displacement curves for the static tests with the pile in dry sand. s.0.1 and s.0.2 are for untouched soil, the rest of the results are for previous cyclic loading with three different frequencies.

Figure 4.4 shows that when the pile is subjected to preceding cyclic loading that the ultimate resistance of the sand increases significantly. A zoom of the load-displacement curves within the first 0.015 m of displacement is shown in figure 4.5.

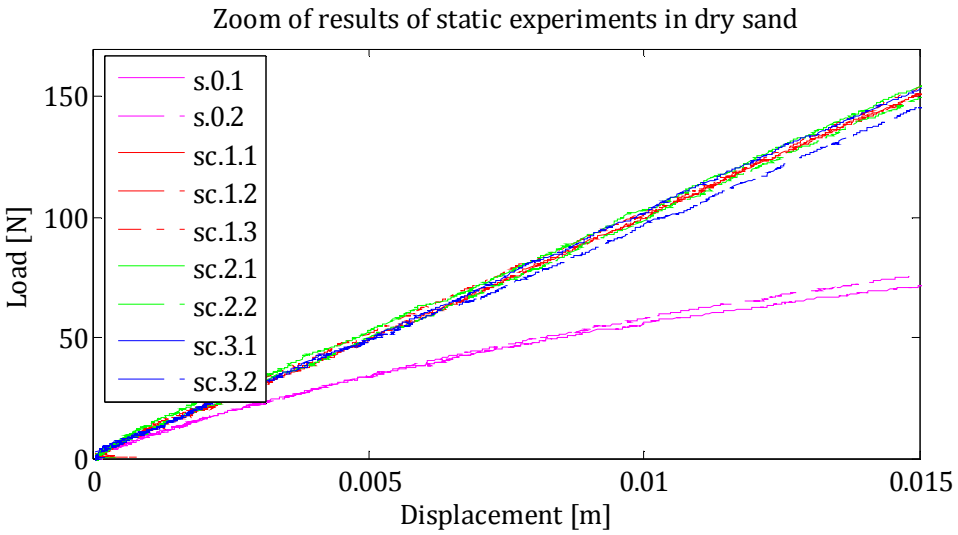

Figure 4.5: Zoom of the area of the initial slope of the load-displacement curves for static loading of pile in dry sand.

From figure 4.5 it is seen that the initial stiffness is improved as well.

The three different frequencies at which the pile has been cyclically loaded previous to the tests are represented by three different colours in the figure. Red is the lowest frequency, green is the middle frequency and blue is the highest frequency. It is seen that the frequency has no influence of the initial stiffnesses of the static curves. The ultimate resistance of the soil varies for the different tests and there is no clear tendency in the ultimate resistance with respect to the frequency of the cyclic loading.

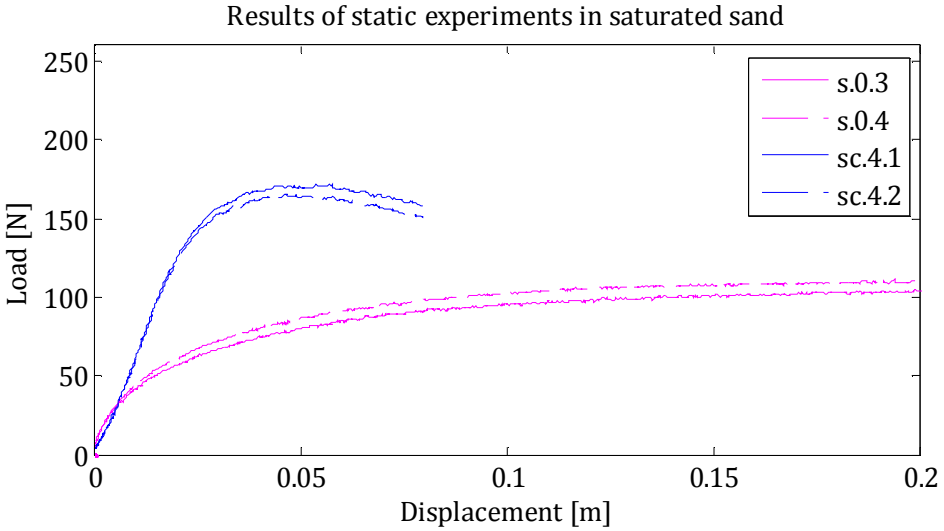

Figure 4.6: Load-displacement curves for the static tests with the pile in saturated sand. s.0.3 and s.0.4 are for undisturbed soil. sc.4.1 and sc.4.2 are for previous cyclic loading with a frequency of 0.27 Hz.

Figure 4.6 shows that also for saturated sand the stiffness and the ultimate resistance of the soil is increased when the sand is subjected to cyclic loading previous to the static tests. The load-displacement curve starts with a smaller slope when the sand is previously cyclically loaded. The maximum amplitude of the cyclic displacement load is 0.015 m. A zoom of the load-displacement curves within this displacement is shown in figure 4.7.

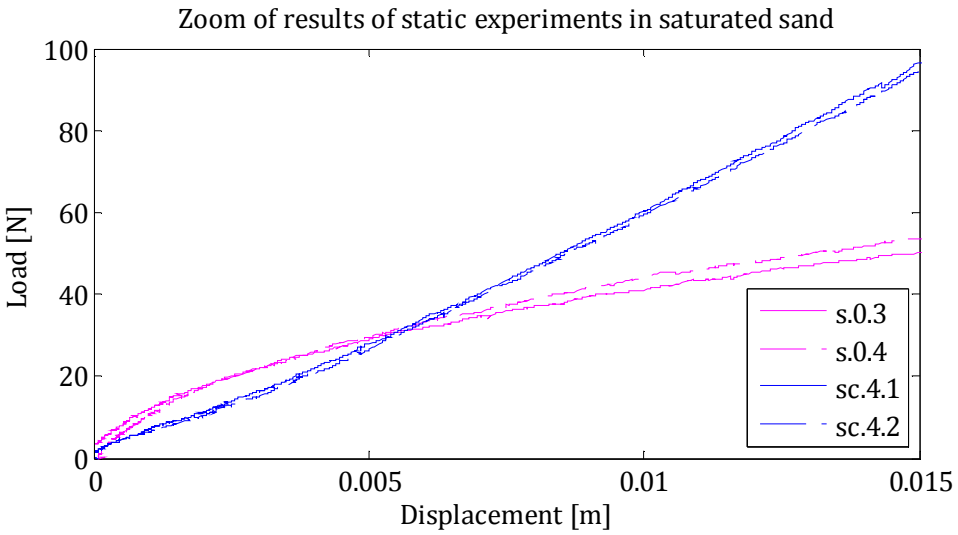

Figure 4.7: Zoom of the area of the initial slope of the load-displacement curves for static loading of pile in saturated sand.

The figure shows that already for a displacement at the top of the pile larger than 0.005 m the slope of the curves for previous cyclic loading is larger than for the curves with untouched sand.

4.3.2 Moment distribution and displacements

The results of the strain gauges and displacement transducers are used in a program designed to determine the displacements along the pile and the moment distribution. The program calculates the horizontal displacements of the pile at any point using the strains below the ground surface and two displacements above the ground surface. The procedure is further described in appendix H, and the program is enclosed on the CD: [CD\programs\piledisplacement].
Even though a decent moment distribution can be determined from the results of the strain gauges it is not possible to determine the pressure distribution below the ground surface from this. The reason for this is shown and explained in appendix I.

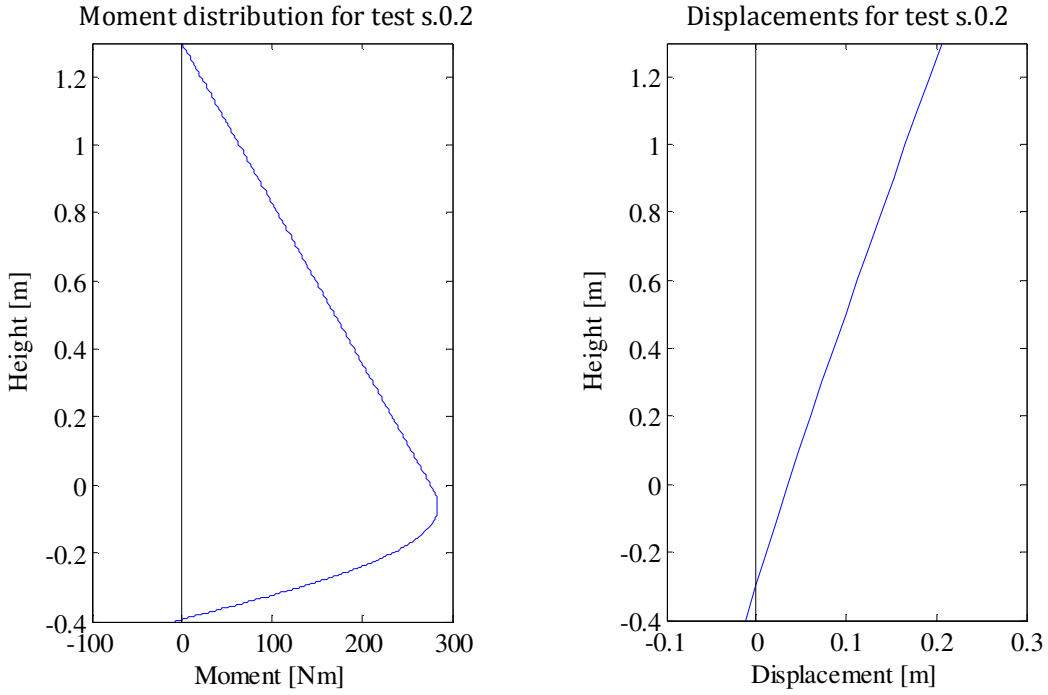

Figure 4.8: Moment distribution (to the left) and displacements along the pile (to the right) for test s.0.2.

The moment distribution in the pile at the ultimate load is determined for test s.0.2 and test s.0.4 where the pile is instrumented with 9 working strain gauges and two displacement transducers. Based on the moment distribution and the two measured displacements the displacements along the pile can be determined as well as the point of zero deflection.
The moment distribution and the displacements along the pile for the static experiment in dry sand are shown in figure 4.8.

The moment distribution and the displacements look realistic and the point of zero deflection is determined to be located 0.29 m below the ground surface. The point of maximum bending moment is located 0.064 m below GS.
The moment distribution and the displacements along the pile for the static experiment in saturated sand are shown in figure 4.9.

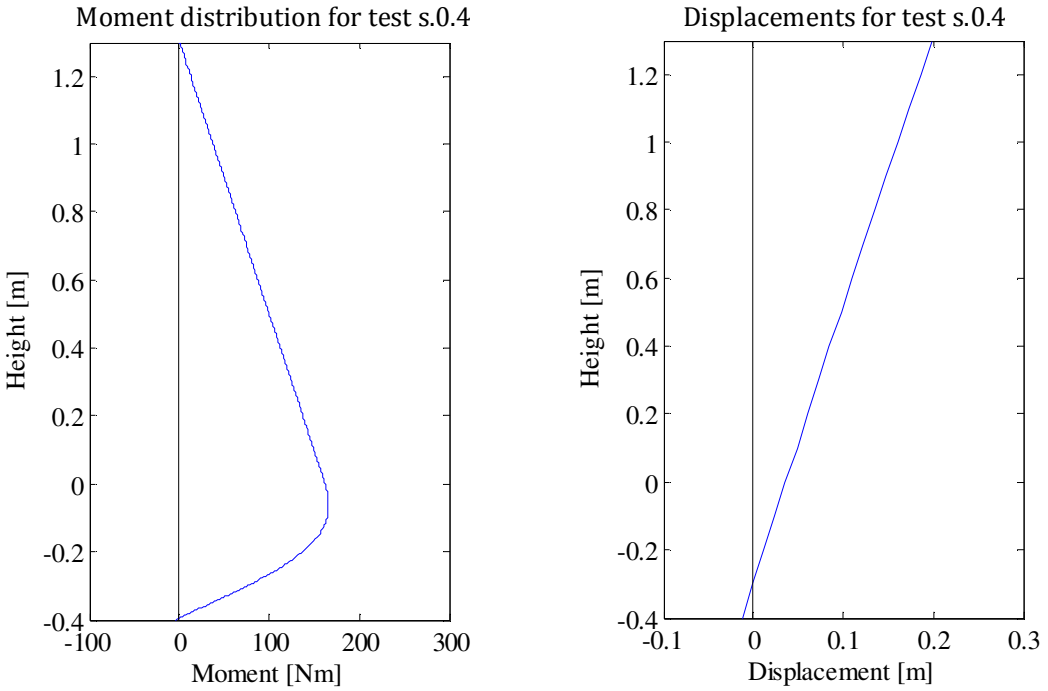

Figure 4.9: Moment distribution (to the left) and displacements along the pile (To the right) for test s.0.4.

The moment distribution and the displacements look realistic and the point of zero deflection is found at 0.30 m below the ground surface. The point of maximum bending moment is located 0.065 m below GS.

The maximum load applied in test s.0.2 is 185 N. In GS that should cause a bending moment of approximately 240 Nm. The strain gauges however, determine the value to be 276 Nm. The maximum load applied in s.0.4 is 120 which theoretically causes a bending moment of 156 Nm at GS. The value estimated from the strain gauges is 162 Nm. In both cases the strain gauges result in a value that is too large with deviations of 15 % and 4 % respectively.

It is observed that the deviation increases for increasing load. This can be seen from figure 4.10. The figure shows the bending moments determined from the strain gauge in the ground surface (GS) and the theoretically calculated moments in static test s.0.2. The same comparison for the two other above ground strain gauges can be seen in appendix F and they show approximately the same deviations.

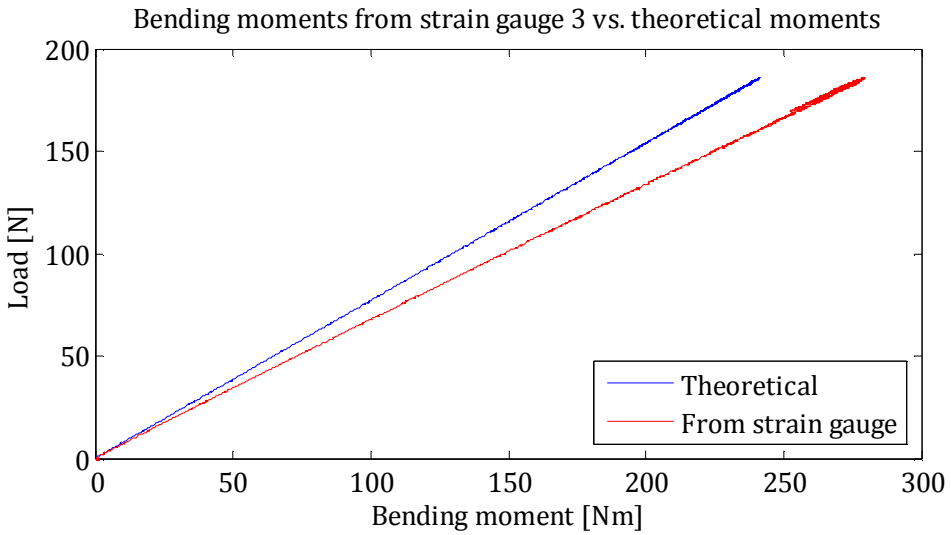

Figure 4.10: Bending moments calculated from the strains measured with the strain gauge in the soil surface compared to theoretically calculated moments.

The figure shows that the deviation between bending moments from the strain gauge in GS and theoretical bending moments is relatively large. The deviations in percent are plotted in appendix F from which it can be seen that the deviations vary with the force. This is a possible explanation of why the error of the same strain gauge differs between the tests s.0.2 and s.0.4.
The varying error makes correcting the results of the strain gauges difficult. Therefore the magnitudes of bending moments can be considered somewhat unreliable. However nothing indicates that the bending moment distribution and the displacement figures are wrong.

4.4 Conclusion for static experiments

The load-displacement curves from the static experiments are considered reliable due to the similarity of the repetitions. This indicates that the method for preparation of the soil domain is sufficient. The tests show that when a pile in dry and saturated sand is subjected to horizontal, cyclic loading, previous to static loading both the stiffness and the ultimate resistance of the sand is increased significantly.
It is seen that the pile moves as a rigid body which is in accordance with the full scale offshore monopiles used for wind turbine foundations.

5 Cyclic experiments

The purpose of the cyclic experiments is to examine the effects of cyclic loading on the sand.
The cyclic experiments are experiments with a pile subjected to cyclic horizontal load. Table 5.1 provides an overview of the cyclic experiments.

Test	Duration [s]	Amplitude [m]	Frequency [Hz]
Pile experiments with cyclic horizontal load on dry sands			
c.1.1	24 h	0.015	0.27 Hz
c.1.2	24 h	0.015	0.27 Hz
c.1.3	12 h	0.015	0.27 Hz
c.2.1	6 h	0.015	0.56 Hz
c.2.2	6 h	0.015	0.56 Hz
c.3.1	4 h	0.015	0.84 Hz
c.3.2	4 h	0.015	0.84 Hz
Pile experiments with cyclic horizontal load on saturated sands			
c.4.1	24 h	0.015	0.27 Hz
c.4.2	24 h	0.015	0.27 Hz

Table 5.1: Overview of the cyclic pile experiments.

5.1 Test setup for cyclic experiments

The experimental setup for the cyclic pile experiments is pictured in figure 5.1. The force is measured at the top of the pile with a force transducer and the displacements are measured 0.141 m above the soil surface with a laser displacement transducer.
The pile is fastened to the wood frame using clamps. After installing the pile, the box is filled with sand until the desired density is attained. The method of compacting the sand is described in section 2.1 p. 12. The straps are tightened to prevent upwards vertical displacement of the pile.

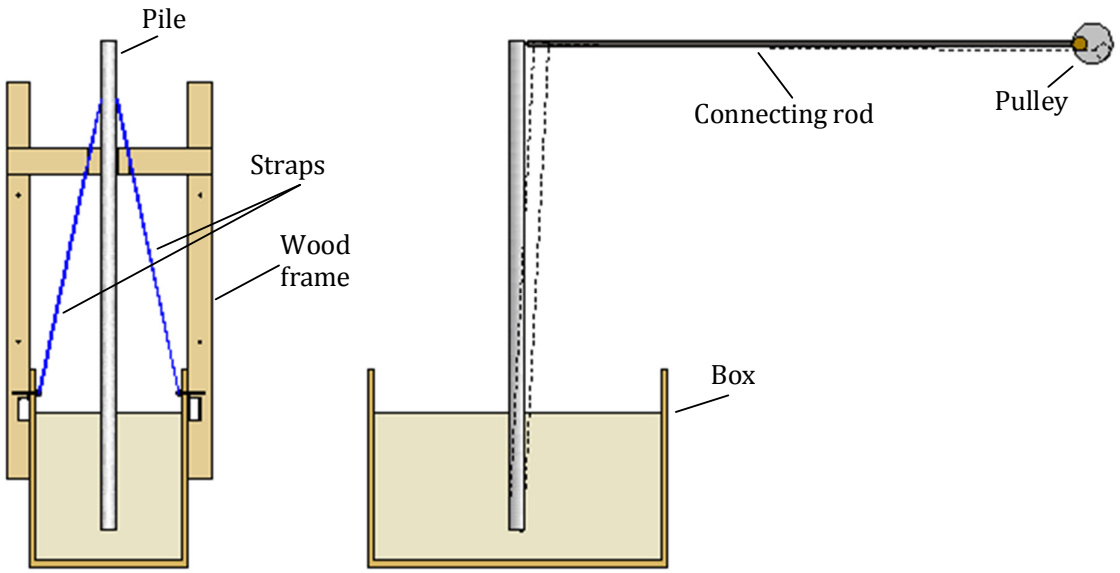

Figure 5.1: Experimental setup for cyclic pile experiments

A displacement controlled load application system is developed for the cyclic tests. An electrical engine is fastened to the concrete wall in the laboratory. A vertical pulley is driven by the engine and a connecting rod is fixed to the pulley with a certain eccentricity. The connecting rod is attached to the pile top as well. When the engine runs, the pile therefore will be exposed to a movement around its initial position with amplitude corresponding to the eccentricity. The principle is shown in figure 5.2.

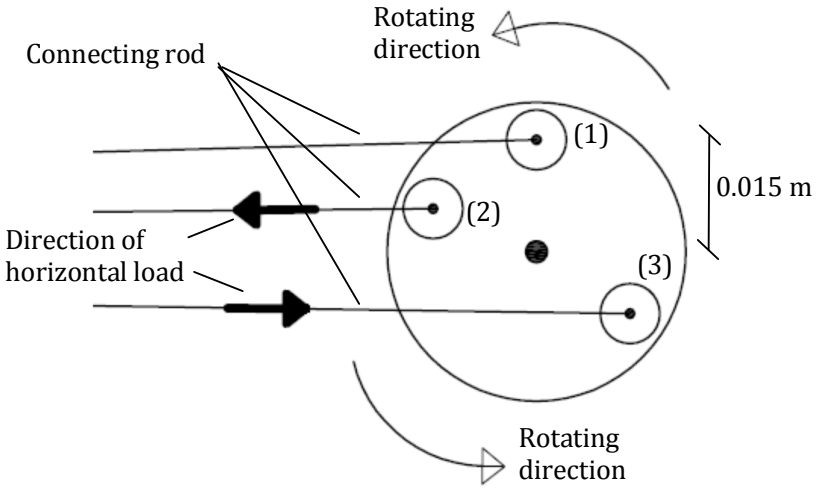

Figure 5.2: Principle of eccentric pulley. (1) The pile is standing vertically. (2) The pile is being pushed in the horizontal direction. (3) The pile is being pulled in the horizontal direction.

The connecting rod is assumed to work as a strut subjected to a bending moment from the eccentricity in connection with the joint between the rod and the pile. The connecting rod is dimensioned in appendix J.

The amplitude of the cyclic loading is 0.015 m, i.e. the prescribed displacement is varying between -0.015 m and 0.015 m. Figure 5.3 shows the movement of the pile assuming rigid body motion.

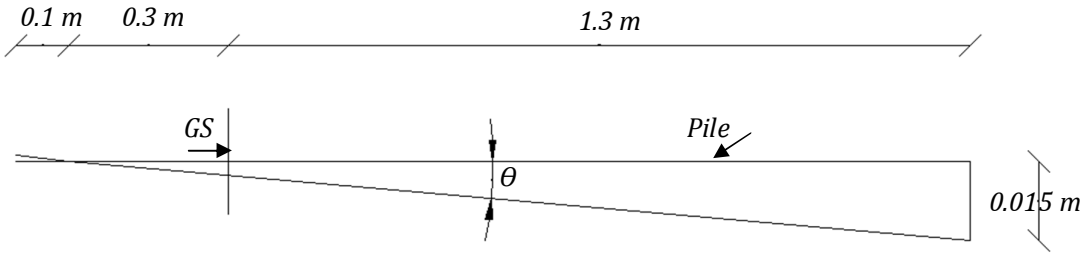

Figure 5.3: Determination of rotation angle.

Provided rigid body motion and point of no deflection located 0.3 m below GS, this corresponds to a rotation angle, θ, of:

$$\theta \approx tan^{-1}\left(\frac{0.015\ m}{1.6\ m}\right) = 0.5° \tag{5.1}$$

Between cyclic tests and the related static test the loading system has to be changed. This needs be done without touching the pile and thereby destroying the soil conditions. Also the pile needs to be in its initial position before changing the loading system. In order to do this the connection of loading system to pile is established as illustrated in figure 5.4.

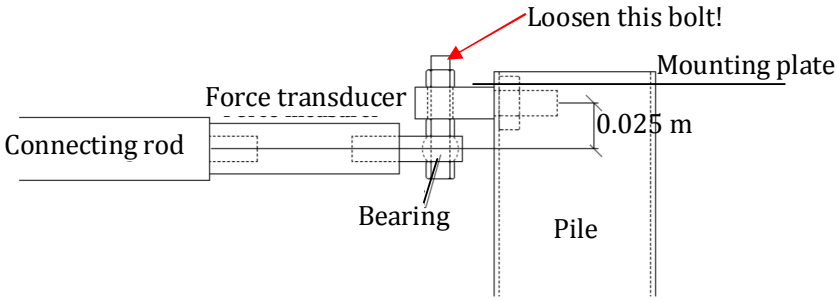

Figure 5.4: Joint between connecting rod and pile. Measurements are in mm.

The cyclic tests are run for a prescribed period of time resulting in the desired number of cycles. When the time is up the engine is turned off and the pile is brought to rest. One bolt is loosened in the joint between the connecting rod and the pile. Only in the initial position this will affect the loading system to fall out of the mounting plate. Therefore the pulley is carefully rotated until the loading system is disconnected.

When the loading system is disconnected the connecting rod is disconnected from the force transducer. After this, the cord used in the static tests is attached to the force transducer and the new loading system is assembled to the mounting plate and the bolt is fastened.
Using this procedure we secure changing the loading system the same way from time to time with a minimum of touching the pile

5.2 Sources of the error for cyclic experiments

In this section the sources of error and uncertainties for the cyclic experiments are evaluated.

5.2.1 Compactness of sand

The method of compacting the sand for the tests is a definite source of error, as the compactness and the homogeneity of the sand can vary from test to test. In section 2.1.1 the uncertainty concerning the average relative density of the soil domain is estimated to vary within the interval of [0.8109 ; 0.8626].

5.2.2 Measuring of force

When the eccentric pulley rotates the force is applied with an oblique angle corresponding to:

$$v = tan^{-1}\left(\frac{\text{Amplitude of the eccentricity}}{\text{Distance between pile top and eccentric pulley}}\right) = tan^{-1}\left(\frac{0.015\text{ m}}{2.0\text{ m}}\right) = 0.43°$$

This means that the maximum component of force in the vertical direction corresponds to 0.0 % of the horizontal force. Hence, this error is negligible.

5.2.3 Measuring of displacements

The displacements are measured with a laser displacement transducer at the ground surface. It has been observed that the transducer does not register change in the displacement as fast as the data logger is set to pick up the data or as fast as the force transducer registers change in force. This means that the load-displacement curves with the cyclic loading are not smooth as they should be. The tendencies of the load-displacement curves are still considered to be right.

5.2.4 Pile movement in vertical direction (straps)

During the cyclic tests some problems with pile movement in vertical direction is discovered. This has been sufficiently controlled though not completely prevented using straps. Different methods have been discussed and tested, see appendix K, and the method with the straps is considered the best. In figure 5.1 it is shown that vertical straps are fastened to the pile in order to keep it from moving upward during the cyclic loading. The effect of these straps depends on how much they are tightened before the load is applied. This can vary from test to test, as they are not tightened using a newton-meter. In the tests in dry sand the pile wants to move upward from the beginning and when the straps prevent this it moves downward instead. When the straps loosen because of the pile moving downward it starts moving upward instead.
In the tests in dry sand the depth of the pile can vary about 0.012 m as it can move 0.002 m down and 0.01 m up in proportion to its initial position. In the experiments in saturated sand the pile moves downward from the beginning and after about an hour it moves upward, but all through the experiments with saturated sand the pile is positioned lower than its starting position. The maximum downward displacement in the cyclic experiments in saturated sand is about 0.03 m.
The effect of the vertical displacements will be evaluated for each individual experiment and will be taken into consideration when reviewing the results.

5.3 Results of cyclic experiments in dry sand

The load as a function of number of cycles for test c.1.1 is shown in figure 5.5. The frequency is 0.27 Hz and the pile has been loaded for 24 hours corresponding to approximately 24,000 cycles. Figure 5.5 shows that the size of the measured load increases with the number of cycles. After about 12,000 cycles, corresponding to about 12 hours of loading, the size of the load has reached a steady state and does not increase additionally after this. Therefore the remaining tests in dry sand are loaded with 12,000 cycles.

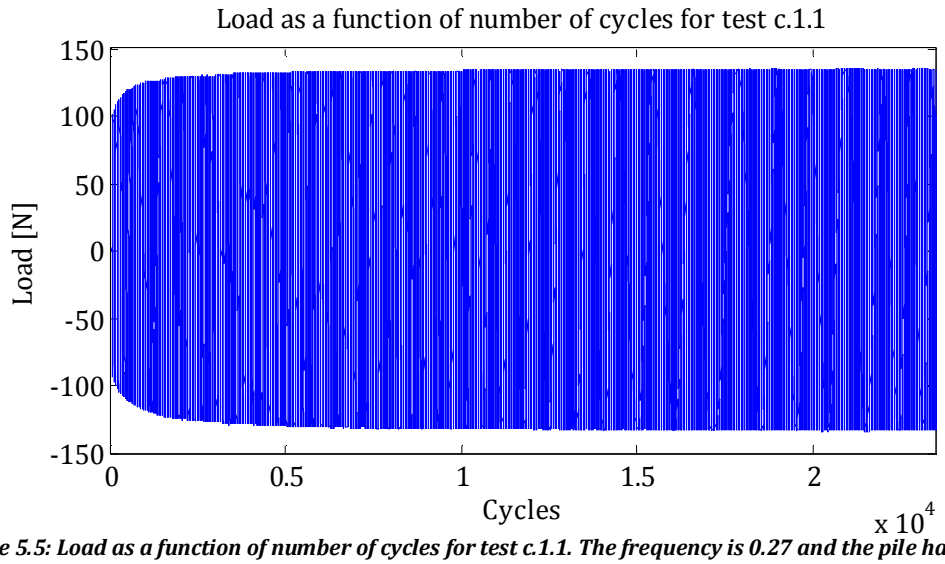

Figure 5.5: Load as a function of number of cycles for test c.1.1. The frequency is 0.27 and the pile has been loaded for 24 hours.

The curves for the load as a function of the number of cycles for the three repetitions with a frequency of 0.27 Hz are compared in appendix L, where it is concluded that the test results are very similar.
Figure 5.6 shows the load-displacement curve for different numbers of cycles.

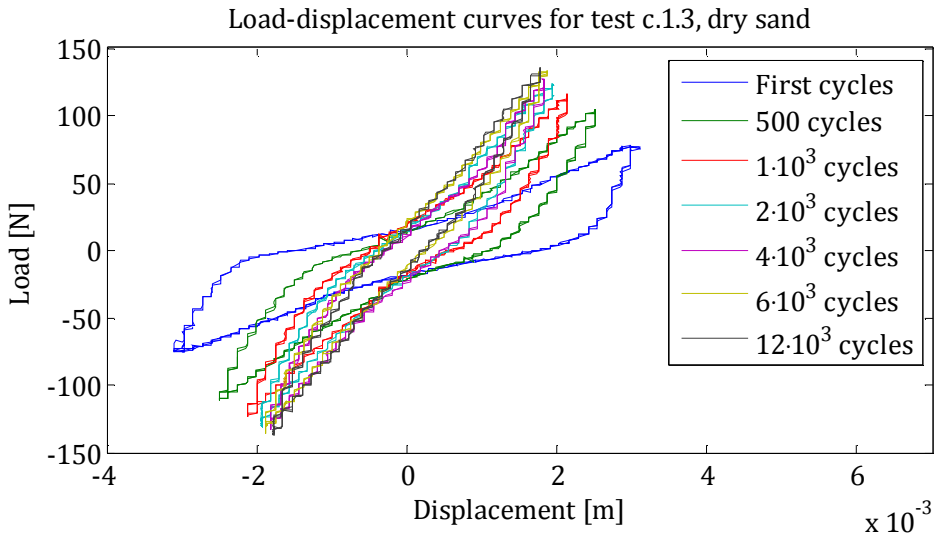

Figure 5.6: Load as a function of displacement for cyclic test c.1.3. The loading frequency is 0.27 Hz.

Figure 5.6 shows that the shape of the load-displacement curves changes with increasing number of cycles. The curves also show the increase in force with increasing number of cycles. The force for the first cycles is about 80 N and for the last cycles it has reached a value of about 140 N. This is an increase in force of about 80 %.
Experiments are made with two other frequencies as well. The load as a function of the number of cycles for these experiments is examined in appendix L and the conclusion is that the two repetitions of the experiments with each frequency are very similar. The load-displacement curves for the experiments with other frequencies are shown in figure 5.7 and figure 5.8.

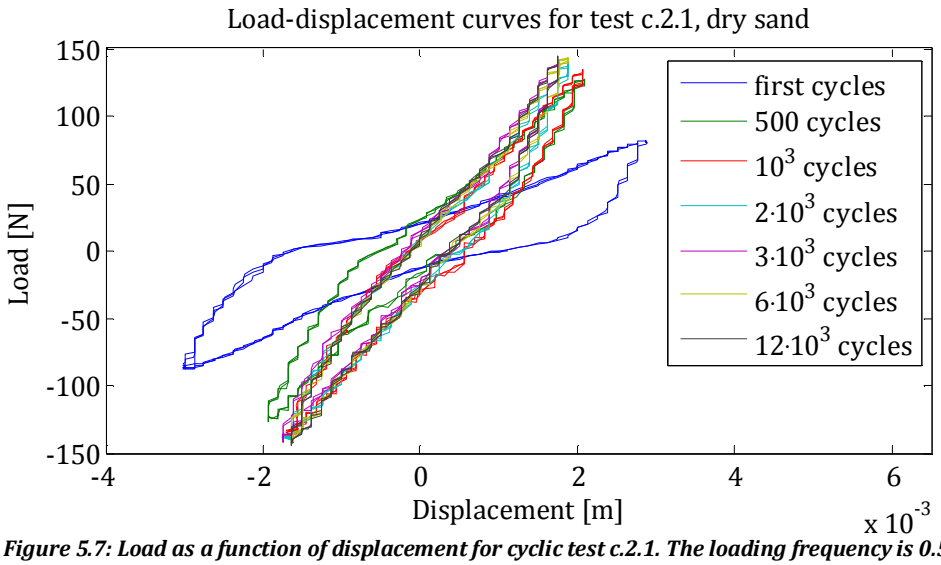

Figure 5.7: Load as a function of displacement for cyclic test c.2.1. The loading frequency is 0.56 Hz.

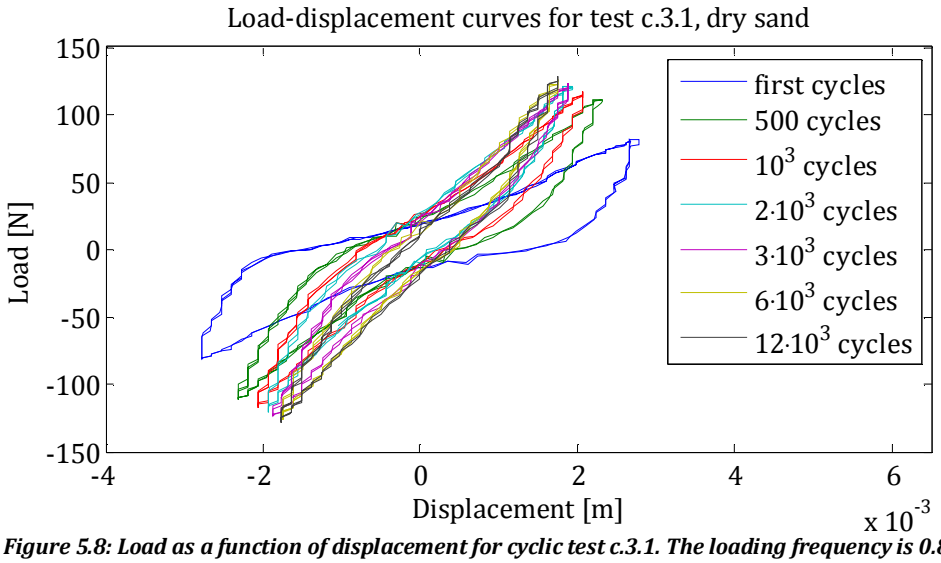

Figure 5.8: Load as a function of displacement for cyclic test c.3.1. The loading frequency is 0.83 Hz.

From the load-displacement curves for the three different frequencies it appears that the shape of the curves with at different numbers of cycles is independent of the loading frequency.

5.4 Results of cyclic experiments in saturated sand

In this section the results of the tests in saturated sand are shown and the repetitions are compared.

Figure 5.9 and figure 5.10 show the load with the number of cycles for the two cyclic tests in saturated soil. In the two figures it can be seen that the pile has moved downward in the beginning of test c.4.2, more than it did in test c.4.1. The pile is at approximately the same level in the end of both tests, where it has a foundation depth of about 0.41 m, see table 4.1, p. 26. Even though the development of the force is different in the two tests, the variations in the force when comparing the two tests are relatively small and therefore the results are considered credible.

Figure 5.11 shows the load-displacement curves at different numbers of cycles for one of the tests in saturated sand.

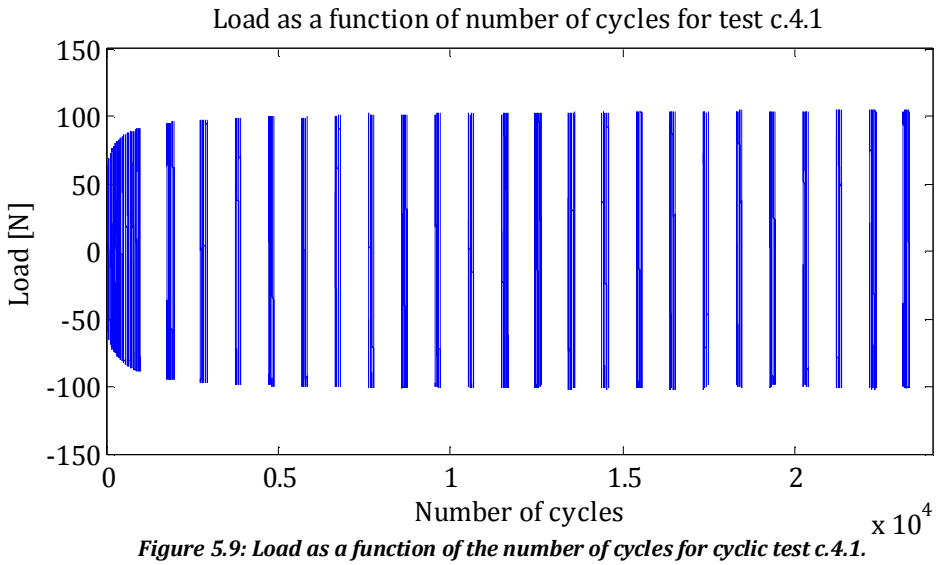

Figure 5.9: Load as a function of the number of cycles for cyclic test c.4.1.

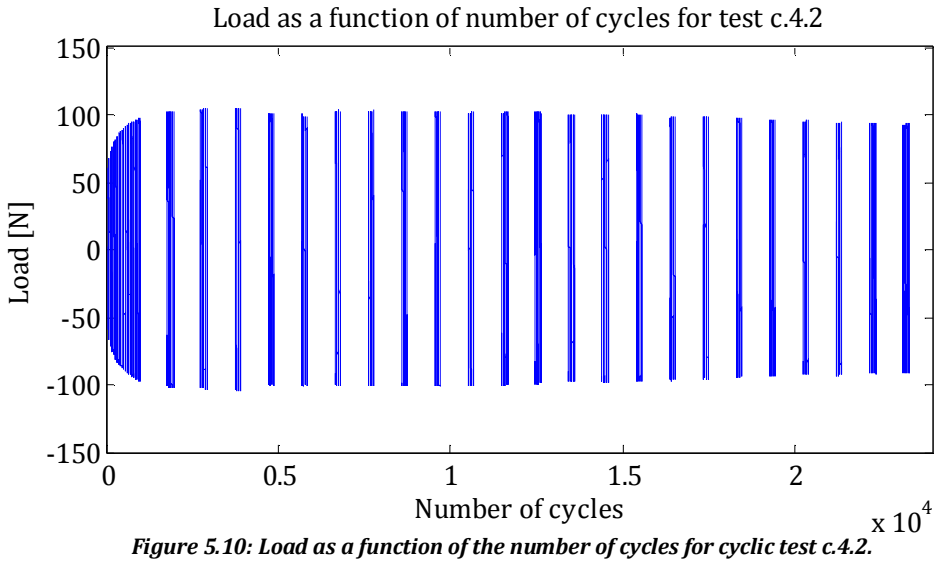

Figure 5.10: Load as a function of the number of cycles for cyclic test c.4.2.

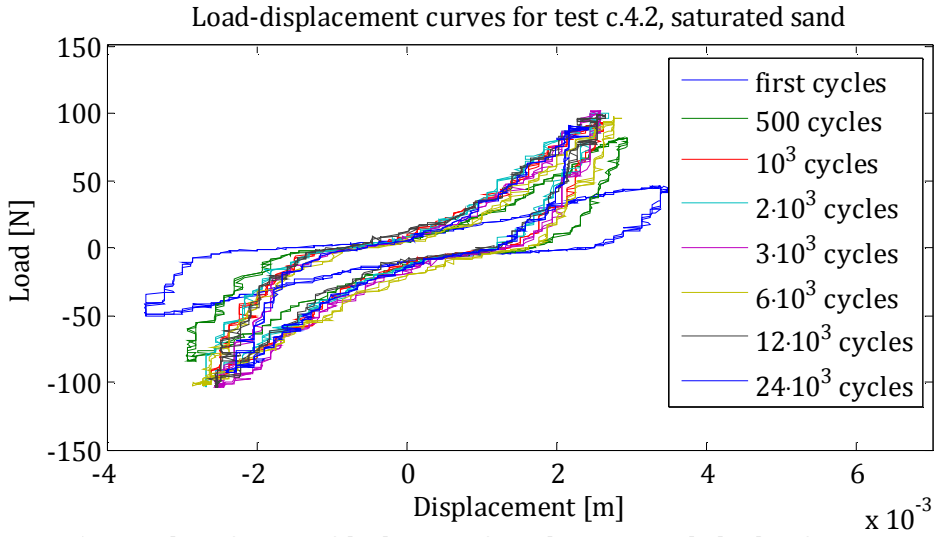

Figure 5.11: Load as a function of displacement for cyclic test c.4.1. The loading frequency is 0.27 Hz.

The shape of the load-displacement curves for the cyclically loaded pile in saturated sand show the same tendency as the curves in dry sand. It can be seen that the stiffness increases throughout the test as the curves become steeper. The effect of a significant increase of the load is also present in saturated sand, estimated to approximately 100 %.

5.5 Evaluation of cyclic experiments

The results for dry and saturated sand are compared with the same loading frequency. Figure 5.12 shows the load displacement curves for first cycles and after 12,000 cycles for test c.1.3 and test c.4.2.

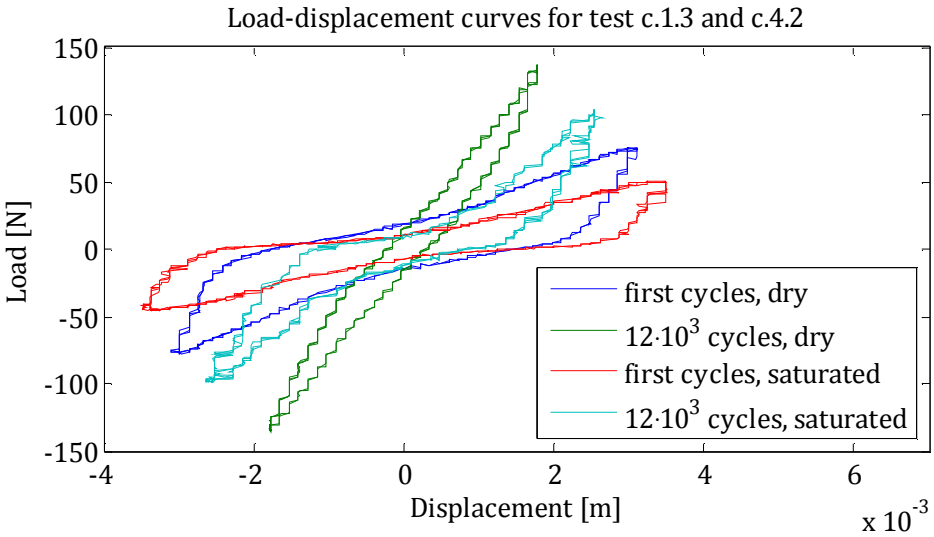

Figure 5.12: Load as a function of displacement for the first cycles and after 12,000 cycles for dry and saturated sand.

It can be seen from figure 5.12 that the stiffness of the soil is greater for dry sand than for saturated sand. The stiffness of the soil influences the shape of the load-displacement curves and this is the reason that the shapes for dry and saturated sand are different.

The curves in figure 5.12 are 'open'. The area of the opening is an expression of the damping in the system. It is a fact that when the stiffness of the soil increases the damping decreases. This explains why the shapes of the load-displacement curves are different for different soil stiffnesses.

It is obvious that the stiffness of the soil increases with the number of cycles. This is because the density of the sand increases near the pile when it is loaded with a cyclic load, see figure 5.13.

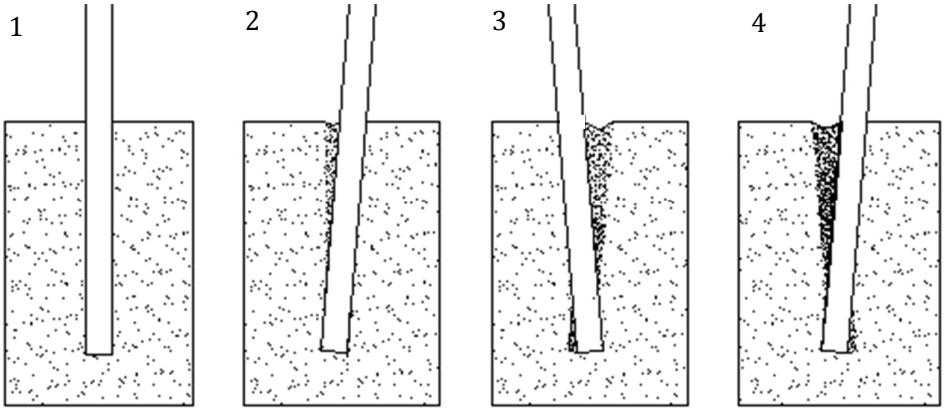

Figure 5.13: Illustration of what happens when the pile is cyclically loaded. 1: The pile is at rest. 2: the pile is loaded the first time and the surrounding sand collapses into the gap that is created behind the pile. This is also what happens in 3 and 4. Therefore each time the pile is loaded, more sand collapses into the gap. This causes the density of the sand near the pile to increase significantly.

Figure 5.12 also shows that the displacements at the soil surface are smaller when the stiffness is greater. This is because the stiffer the soil is, the larger the deformations of the pile itself, so when the top displacement is the same, the displacement at the soil surface will be smaller when the soil has larger stiffness. The principal is illustrated in figure 5.14.

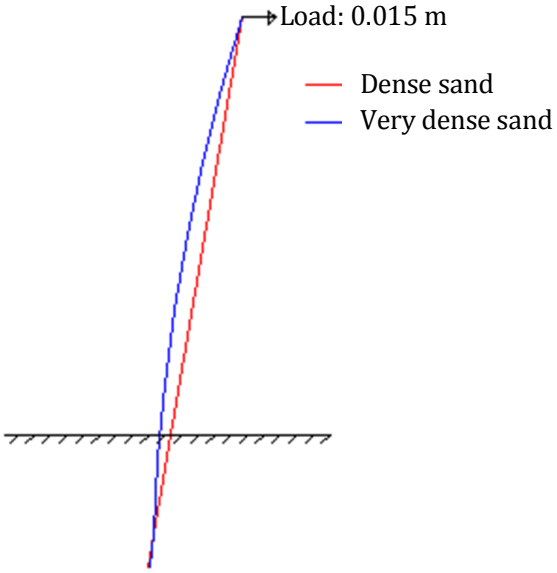

Figure 5.14: Illustration of the displacements at the soil surface becoming smaller as the density of the sand increases.

The force increases with the number of cycles, see figure 5.1. This increase in force is examined and compared for the three different loading frequencies in dry sand. The Load as a function of the number of cycles for all the cyclic experiments in dry sand is shown in figure 5.15, where the load is relative to its maximum value.

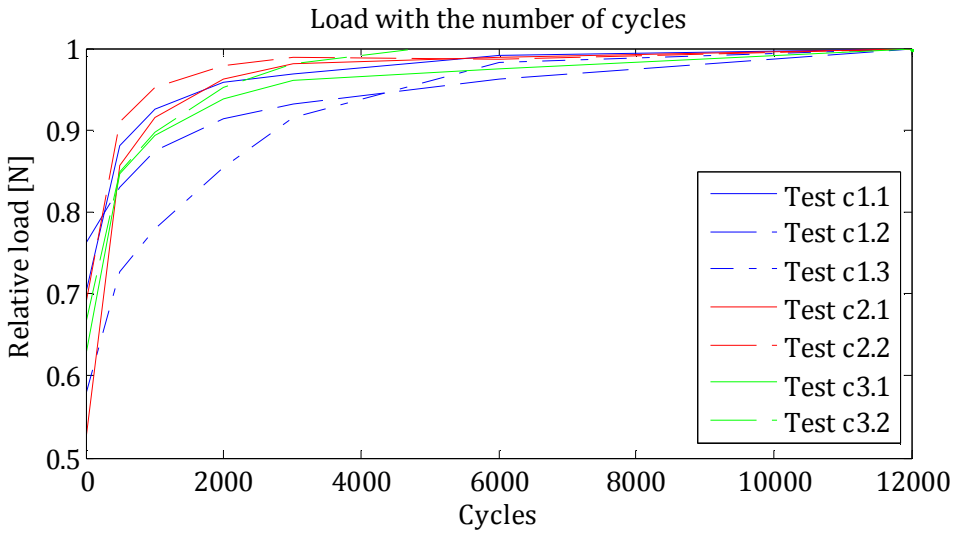

Figure 5.15: Load as a function og the number of cycles for all the cyclic experiments in dry sand. The load is relative to its maximum value.

Figure 5.15 shows that there is no clear tendency of the frequency having influence on the number of loading cycles which it takes to reach the steady state.
When the pile is subjected to cyclic loading a crater in the soil around the pile is created. The crater for dry sand is shown in figure 5.16.

Figure 5.16: Picture of the crater in sand around the pile after cyclic loading in dry sand. The boundaries of the crater are marked with a red line.

In saturated sand the water line is about five centimetres above the sand and this means that the crater cannot be seen very well. Therefore the water is drained out so that the crater can be seen. Both the drained and undrained image is shown in figure 5.17.

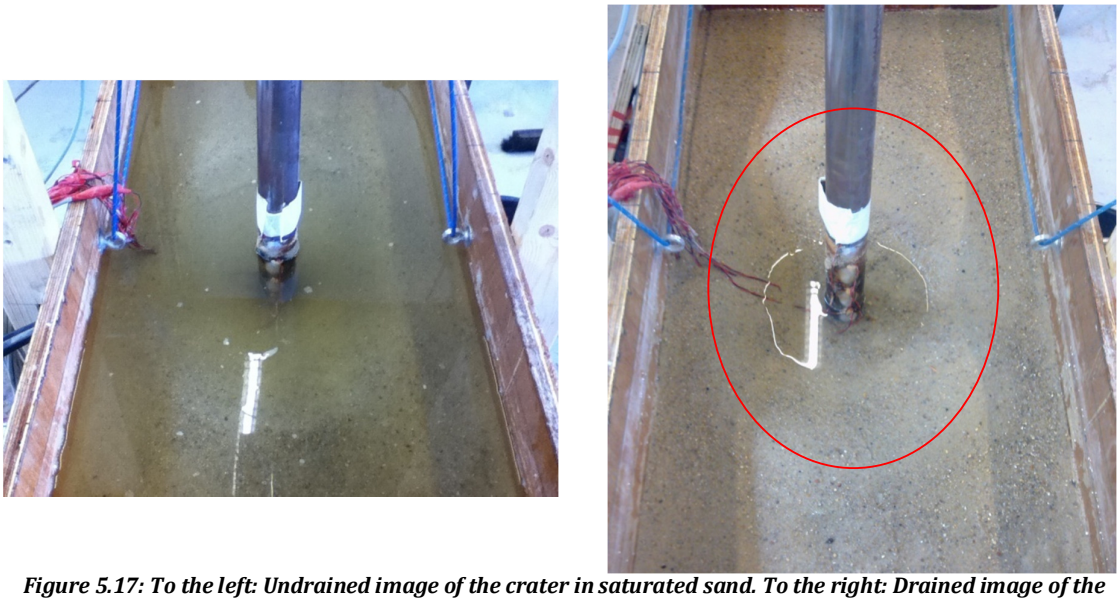

Figure 5.17: To the left: Undrained image of the crater in saturated sand. To the right: Drained image of the crater in saturated sand. The boundaries of the crater are marked with a red line.

The figure shows that the crater around the pile is larger for saturated sand than dry sand.

From experience with the cyclic tests we can see that the pile is not completely rigid as the displacement in GS differs from the first cycles throughout the last cycles. This is due to the increase in soil strength and stiffness. The displacement in the last cycles in the end of the tests is approximately 2/3 of the displacement in the first cycles.

That corresponds to a rotation angle of:

$$\theta \approx tan^{-1}\left(\frac{0.015}{1.6} \cdot \frac{2}{3}\right) = 0.35° \tag{5.2}$$

These rotation angles are reasonable, as an article of Kellezi and Hansen [2] specifies the maximum rotation angle of an offshore monopile to be 0.37-0.38°. In the same article dynamic loads of bending moment and lateral displacement are evaluated, where the predominant frequency for both loads is 0.25 Hz. In the cyclic tests load is applied with frequencies of 0.27-0.84 Hz which is in the same magnitude as the loads described in the article.

6 Beam on nonlinear Winkler foundation

A simple 2D beam model supported by a number of nonlinear springs is established. The model is implemented in MATLAB and a reference model is constructed in Abaqus.

The purpose of building the 2D beam model is to:

- Investigate the efficiency of the existing p-y method.
- Investigate the principle of the p-y method

In principle the model can be established with Abaqus, but a self-programmed code has some advantages compared to the Abaqus code, see section 6.1. Therefore only a reference model is established in Abaqus to verify the results of the MATLAB routine. The MATLAB routine is described in section 6.2 and is enclosed on the CD: [CD\programs\BEAM_NL], and can be executed from the m-file [CD\programs\BEAM_NL\main.m].

6.1 Abaqus reference model

A simple model with four nonlinear springs with an exponential relation between displacement and force is established in Abaqus. The model is assembled from 6 Bernoulli beam elements, and a prescribed displacement is given in the top node, as shown in figure 6.1.

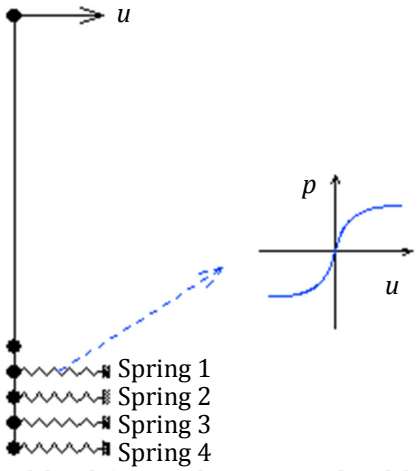

Figure 6.1: Reference model with four axial connectors placed directly in the nodes.

Abaqus provides nonlinear elastic springs to describe the material behaviour by use of connector elements. The characteristics of the connector elements are given as table input, defining the relation between displacement and spring force. In order to obtain reasonable results with highly nonlinear springs the force-displacement curve is discretized in many points. This procedure is rather time-consuming and therefore the model is not efficient, in case of many springs or calibration of spring elements. In case of unloading and reloading the force displacement curve is followed. This does not correspond to the behaviour of the soil in cyclic loading.

Two different sets of springs are used in the reference model:

- Set A consists of four similar exponential springs.
- Set B consists of four different exponential springs.

The expression of the spring forces is given by equation (6.1):

$$f_{spring} = -b \cdot exp(-a \cdot y) + b \text{ if } y \geq 0$$
$$f_{spring} = b \cdot \exp(a \cdot y) - b \text{ if } y < 0 \quad (6.1)$$

The constants, a and b, are given in table 6.1, and y is the displacement of the spring.

	a	b
Set A		
Spring 1, 2, 3 & 4	100	20,000
Set B		
Spring 1	1,000	5,000
Spring 2	1,200	7,500
Spring 3	1,400	10,000
Spring 4	1,600	12,500

Table 6.1: constants a and b used in the spring sets 3 and 4.

6.2 MATLAB routine

The MATLAB routine can handle models that consist of a number of 2D Bernoulli beam elements supported by nonlinear springs. The beam is considered linear elastic. To handle the nonlinear properties of the springs an incremental iterative solver is used.

6.2.1 Preprocessing

In a coordinate matrix the nodal points are defined. A topology matrix is also defined, telling the program how the nodal points are connected to each other. These two matrices define the geometry of the model.

As axial effects are of no interest the axial degree of freedom is left out and only lateral displacement and rotation are considered, see figure 6.2.

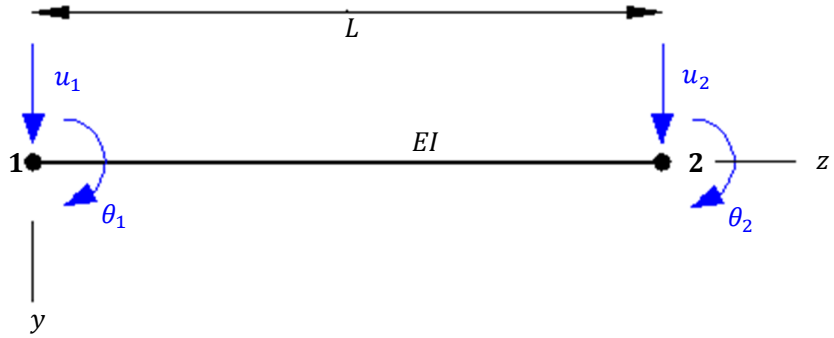

Figure 6.2. Beam element used in self-programmed MATLAB code.

Bernoulli-Euler beam theory is used. As each beam element has four degrees of freedom the stiffness matrix for a single beam element is a four by four matrix, given by equation (6.2):

$$\boldsymbol{K}_{\boldsymbol{beam,elem}} = \begin{bmatrix} 12EI/L^3 & 6EI/L^2 & -12EI/L^3 & 6EI/L^2 \\ 6EI/L^2 & 4EI/L & -6EI/L^2 & 2EI/L \\ -12EI/L^3 & -6EI/L^2 & 12EI/L^3 & -6EI/L^2 \\ 6EI/L^2 & 2EI/L & -6EI/L^2 & 4EI/L \end{bmatrix} \tag{6.2}$$

In equation (6.2), L is the element length and EI is the element bending stiffness.

The springs are attached to the beam elements in the nodes. It is decided that one spring can be attached to a desired element, and the spring should be added in the lower node of the element.

The spring is lateral to the beam and therefore the stiffness of the spring, k, is added to the beam stiffness in the considered degree of freedom.

This is done with help from a matrix, $\boldsymbol{K}_{spring,elem}$, given by equation (6.3):

$$\boldsymbol{K}_{spring,elem} = k \begin{bmatrix} 1 & 0 & 0 & 0 \\ 0 & 0 & 0 & 0 \\ 0 & 0 & 0 & 0 \\ 0 & 0 & 0 & 0 \end{bmatrix} \tag{6.3}$$

The spring stiffness is determined as the tangential stiffness to the load-displacement curve for the actual spring, see figure 6.3.

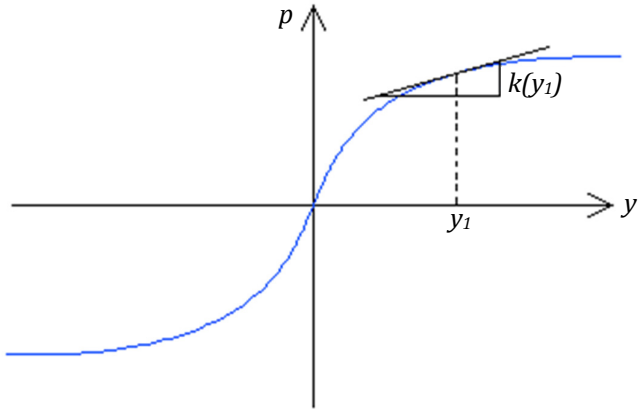

***Figure 6.3: Determination of spring stiffness,** k.*

The tangential stiffness matrix for each element is determined from equation (6.4):

$$\boldsymbol{K}_{tan,elem} = \boldsymbol{K}_{spring,elem} + \boldsymbol{K}_{beam,elem} \tag{6.4}$$

The elements are connected in the nodes and the global tangential stiffness matrix, $\boldsymbol{K}_{tan}$, is found by assembling the local tangential stiffness matrices for the elements. The principle of assembling is shown in figure 6.4 for 3 elements sharing 2 nodes: that is node 2 and node 3.

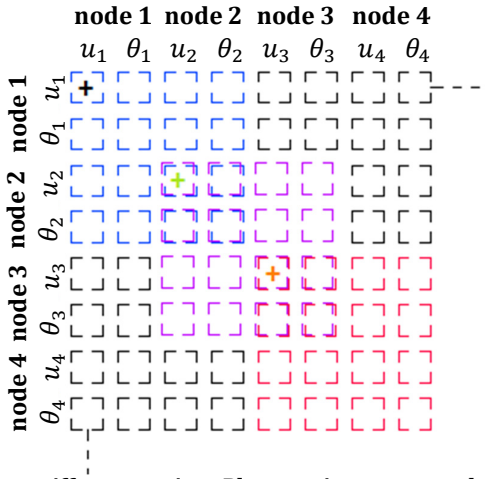

Figure 6.4: Assembling of element stiffness matrices. Blue matrix represents the element stiffness matrix of element 1 and the black + represents the contribution from the spring attached to the node 1 of element 1 (global node 1). The purple matrix represents element 2 and the green + is the spring attached to the node 1 of element 2 (global node 2). The red matrix is element 3 and the orange + is the spring attached to node 1 of element 3 (global node 3). The black squares contain zeros.

6.2.2 Boundary conditions

The program is displacement controlled, and a displacement can be prescribed in any node of interest.

As described in section 6.2.1 each node has two degrees of freedom (dof). The displacement and the dof in which it acts are prescribed. The dofs with a prescribed displacement different from zero are assembled in a vector denoted $\boldsymbol{l_{dof}}$. Dofs with a prescribed displacement of zero are supported.

$\boldsymbol{l_{dof}}$ is used to determine the reaction force vector, $\boldsymbol{f_{reac}}$. The reaction force vector is extracted from the internal force vector, $\boldsymbol{f_{int}}$.

The lengths of both $\boldsymbol{f_{reac}}$ and $\boldsymbol{f_{int}}$ correspond to the total number of dofs in the considered system. $\boldsymbol{f_{reac}}$ is given by equation (6.5).

$$\boldsymbol{f_{reac}}(\boldsymbol{l_{dof}}) = \boldsymbol{f_{int}}(\boldsymbol{l_{dof}}) \tag{6.5}$$

Additional two vectors are constructed in order to separate dofs with prescribed displacement (zero or not zero) from free dofs.

The vector with prescribed dofs is denoted $\boldsymbol{b_{dof}}$, and the vector which contains the values of the prescribed dof is referred to as $\boldsymbol{dp}$. Free dofs are collected in a vector as well, referred to as $\boldsymbol{f_{dof}}$.

6.2.3 Solution

We have an internal force vector, $\boldsymbol{f_{int}}$ and a reaction force vector, $\boldsymbol{f_{reac}}$. From these two vectors we find the residual force vector, $\boldsymbol{f_{res}}$, from equation (6.6):

$$\boldsymbol{f_{res}} = \boldsymbol{f_{reac}} - \boldsymbol{f_{int}} \tag{6.6}$$

The internal force vector consists of two contributions, one from the beam, $\boldsymbol{f_{int,B}}$, which is considered linear elastic, and one from the springs, $\boldsymbol{f_{int,S}}$, which is nonlinear. Hence, the internal force vector is given by equation (6.7):

$$\boldsymbol{f_{int}} = \boldsymbol{f_{int,B}} + \boldsymbol{f_{int,S}} \tag{6.7}$$

The beam contribution is computed from equation (6.8):

$$\boldsymbol{f_{int,B}} = \boldsymbol{K_{beam}} \cdot (\boldsymbol{u_j} + \Delta\boldsymbol{u_i}) \tag{6.8}$$

Where:

i refers to the number of the preceding iteration
j refers to the number of the preceding loadstep
$\boldsymbol{u}$ is the total displacement
$\Delta\boldsymbol{u}$ is the incremental displacement

The spring contribution is calculated from equation (6.9):

$$\boldsymbol{f_{int,S}} = \boldsymbol{S}(\boldsymbol{u_j} + \Delta\boldsymbol{u_i}) \tag{6.9}$$

The length of $\boldsymbol{S}$ corresponds to the total number of dofs in the system. In the dofs where a spring is attached, $\boldsymbol{S}$ contains a value equivalent the spring reaction for the given displacement of the dof. The spring reaction is directly defined from explicit expressions.

6.2.3.1 Incremental iterative solver

A first iteration is used to get the problem started.

Supposing we want to solve the problem in one loadstep, we have at this stage the tangential stiffness matrix, $\boldsymbol{K_{tan}}$, where the spring contribution has been computed from the spring initial stiffness corresponding to zero displacement of the springs.

In the first loadstep $\boldsymbol{u}_j = \boldsymbol{u}_0 = \mathbf{0}$. Furthermore in the first iteration $\Delta\boldsymbol{u}_i = \Delta\boldsymbol{u}_0 = \mathbf{0}$. Consequently, the beam has no deformations and the spring neither; therefore $\boldsymbol{f_{int}} = \mathbf{0}$ and $\boldsymbol{f_{reac}} = \mathbf{0}$, hence $\boldsymbol{f_{res}} = \mathbf{0}$

However, we have nodes with prescribed displacement. Therefore displacements in the other nodes most likely will differ from zero; these displacements need correction. To obtain a guess of the displacements in the other nodes, we solve for the part of the system concerning the free dofs, see equation (6.10). Equation (6.10) is only used in the first iteration:

$$d\boldsymbol{u}_{i+1,\boldsymbol{fdof}} = \boldsymbol{K_{tan}}\left(\boldsymbol{f_{dof}}, \boldsymbol{f_{dof}}\right)^{-1}\left(\boldsymbol{f_{res}}\left(\boldsymbol{f_{dof}}\right) - \boldsymbol{K_{tan}}\left(\boldsymbol{f_{dof}}, \boldsymbol{b_{dof}}\right)\boldsymbol{dp}\right) \tag{6.10}$$

From this we now have a guess of the displacements needed in all beam nodes, as the displacement in the rest of the dofs are prescribed.

$$d\boldsymbol{u}_{i+1,\boldsymbol{bdof}} = \boldsymbol{dp} \tag{6.11}$$

From this guess of displacement corrections we update the incremental displacement vector:

$$\Delta\boldsymbol{u_{i+1}} = \Delta\boldsymbol{u_i} + d\boldsymbol{u_{i+1}} \tag{6.12}$$

Based on equation (6.12) we go back and solve the equations (6.6) to (6.9). Here the second iteration starts. Unless the system is linear this will result in $\boldsymbol{f_{res}} \neq \mathbf{0}$. That is because the tangential stiffnesses of the springs has been used to calculate the guess, but the stiffness of the springs is not linear, so the actual force in the springs differ from what we assumed in the previous iteration.
So the system is not balanced, and consequently we have to make a correction of the displacements. To keep the iterative procedure going we solve equation (6.13):

$$d\boldsymbol{u_{fdof}} = \boldsymbol{K_{tan}}\left(\boldsymbol{f_{dof}}, \boldsymbol{f_{dof}}\right)^{-1}\boldsymbol{f_{res}}\left(\boldsymbol{f_{dof}}\right) \tag{6.13}$$

The displacement of the prescribed dofs is the same as in the present iteration. From this we have a new guess of the displacements, so we update the incremental displacement vector again, see equation (6.14):

$$\Delta\boldsymbol{u_{i+2}} = \Delta\boldsymbol{u_i} + d\boldsymbol{u_{i+1}} + d\boldsymbol{u_{i+2}} = \Delta\boldsymbol{u_{i+1}} + d\boldsymbol{u_{i+2}} \tag{6.14}$$

If we want to see how the solution develops, we need several loadsteps.
For the solver to remember the solution from previous loadstep we update $\boldsymbol{u}$ in the end of each loadstep, see equation (6.15):

$$\boldsymbol{u_{j+1}} = \boldsymbol{u_j} + \Delta\boldsymbol{u_{i+1}} \tag{6.15}$$

In equation (6.15) *j* refers to the number of the preceding loadstep.

The procedure of solving in several loadsteps is exactly the same as solving in one loadstep. Instead of starting from zero, the next loadstep is started from the converged point from the previous step. Note we now change the prescribed displacement as the total displacement is divided by the number of loadsteps, see figure 6.5.
This will again result in $\boldsymbol{f_{res}} = \mathbf{0}$ in the first iteration, because $\Delta\boldsymbol{u}_i = \Delta\boldsymbol{u}_0 = \mathbf{0}$. Therefore, again we solve equation (6.10) to obtain a start guess for the solution. Now the iterative procedure has been started.

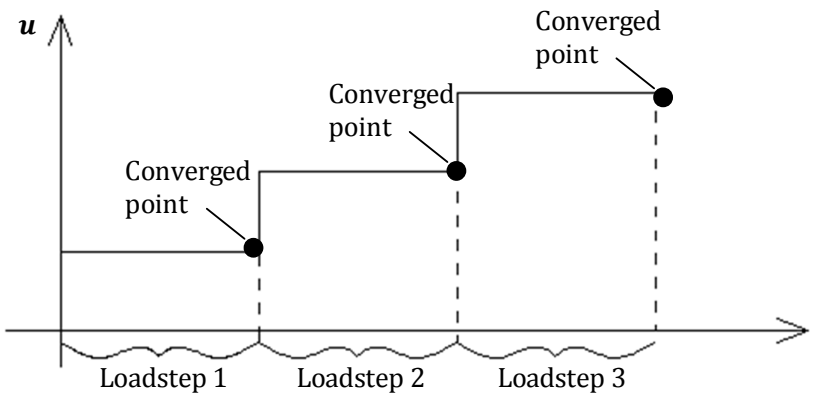

Figure 6.5: Illustration of the change in displacement load. The prescribed displacement in a loadstep is the total displacement divided by the number of loadsteps.

The iterative procedure continues until convergence is achieved. That is when $\boldsymbol{f_{res}} = \mathbf{0}$ within a reasonable tolerance. To achieve this, a standard for convergence must be defined.

6.2.3.2 Convergence

Many standards for convergence can be applied, what is important is to stop the iterative procedure, when further iterations do not result in changes of the result within some user defined tolerance. For instance the norm of $\boldsymbol{f_{res}}$ can be used directly as convergence criterion. In this program however, the L_2-norm of the correction displacements is used to define the convergence criterion:

$$\|d\boldsymbol{u_{i+1}}\|_2 \leq \varepsilon \cdot \|d\boldsymbol{u_i}\|_2 \tag{6.16}$$

The value of the convergence tolerance, ε, must be chosen carefully. If the tolerance is too loose the solution may be inaccurate, but if it is chosen to strict it will cost a lot of extra iterations and hardly improve the result.The ε parameter is set to $\varepsilon = 10^{-6}$ which is small enough to obtain a reasonably accurate solution. When the convergence criterion is fulfilled, equilibrium between external and internal forces is obtained, that is $\boldsymbol{f_{res}} = \mathbf{0}$.

6.2.4 Example

To illustrate the principles of an incremental iterative solver, a small example is made.

Figure 6.6: Model used for illustration of the solution principle.

A beam modelled with four elements is supported by four similar springs in the four bottom nodes. The beam is given a prescribed displacement in the top node, see figure 6.6.
The total load is applied in two loadsteps. The springs are non-linear so iterations are needed to solve the problem. As the displacement in the top node is maintained throughout the iterations the load will change until it reaches the equilibrium path. The displacements of the other nodes will change throughout the procedure as well as the reactions in the springs. The reactions of the springs balance the reaction in the top node. The principles are illustrated in figure 6.7.

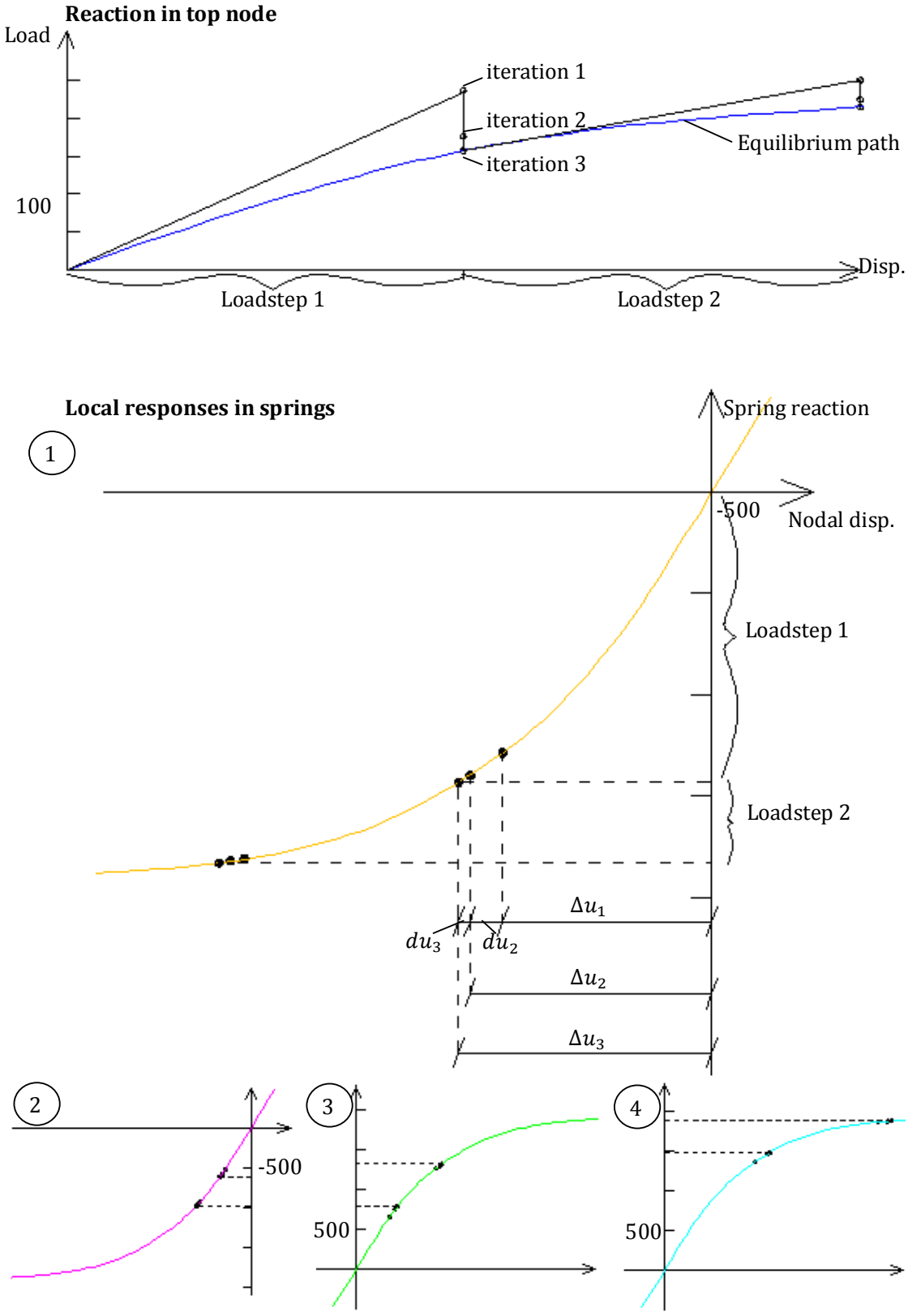

Figure 6.7: Top: Reaction in the top node, the displacement is maintained throughout the iterations, but the load is changed to follow the true equilibrium path. Mid and bottom: Reactions in the springs 1, 2, 3 and 4 cf. figure 6.6. Here the displacement is changed between the iterations causing a change in the spring reactions. The sum of spring reactions equals the reaction in the top node in all iterations. Axis index is the same for all the springs.

6.2.5 Flow diagram

Flow diagram, nonlinear FEM code

PREPROCESSING
The geometry is defined, nodes and elements. The pile section constants *E* and *I* are defined, and the load is defined.

SOLUTION
The total displacement vector $\boldsymbol{u}$ is initialized. $\boldsymbol{u}_0 = \boldsymbol{0}$

Load loop (looping over the number of loadsteps)
The incremental displacement vector $\Delta\boldsymbol{u}$ is initialized. $\Delta\boldsymbol{u}_j = \boldsymbol{0}$

Iteration loop
The internal force vector $\boldsymbol{f_{int}}$ and the reaction force vector $\boldsymbol{f_{reac}}$ are initialized.
$\boldsymbol{f_{int}} = \boldsymbol{0}$, $\boldsymbol{f_{reac}} = \boldsymbol{0}$
The corrector displacement vector $d\boldsymbol{u_i}$ is initialized. $d\boldsymbol{u}_i = \boldsymbol{0}$

Element loop (looping over the number of elements)
The local stiffness matrices are calculated from (6.2), (6.3) and (6.4).

The global stiffness matrices are calculated from locals.

$\boldsymbol{K_{beam}}(dof, dof) = \boldsymbol{K_{beam}}(dof, dof) + \boldsymbol{K_{beam,elem}}$
$\boldsymbol{K_{tan}}(dof, dof) = \boldsymbol{K_{tan}}(dof, dof) + \boldsymbol{K_{tan,elem}}$
Element loop ends

The internal force vector is determined, see equation (6.9).
$\boldsymbol{f_{int,B}} = \boldsymbol{K_{beam}} \cdot (\boldsymbol{u_j} + \Delta\boldsymbol{u_i})$
$\boldsymbol{f_{int,S}} = \boldsymbol{S}(\boldsymbol{u_j} + \Delta\boldsymbol{u_i})$
$\boldsymbol{f_{int,S}} = \boldsymbol{S}(\boldsymbol{u_j} + \Delta\boldsymbol{u_i})$

The reaction force vector is determined, see equation (6.5).
$\boldsymbol{f_{reac}}(\boldsymbol{l_{dof}}) = \boldsymbol{f_{int}}(\boldsymbol{l_{dof}})$

The residual force is determined.
$\boldsymbol{f_{res}} = \boldsymbol{f_{reac}} - \boldsymbol{f_{int}}$
The corrector displacement, $d\boldsymbol{u}_{i+1}$ is computed from (6.10) or (6.13) depending on the iteration.

The incremental displacement is updated, using $\boldsymbol{K_{tan}}$.
$\Delta\boldsymbol{u}_{i+1} = \Delta\boldsymbol{u}_i + d\boldsymbol{u}_{i+1}$

Convergence is investigated
Iteration loop ends

The total displacement is updated.
$\boldsymbol{u_{j+1}} = \boldsymbol{u_j} + \Delta\boldsymbol{u_{i+1}}$
Load loop ends

POSTPROCESSING
Figure plots and solution saves.

6.3 Verification of the MATLAB routine

A similar model to the reference model has been defined in the MATLAB program.
The results of the program are compared to the results from Abaqus for both the set of springs A and B.

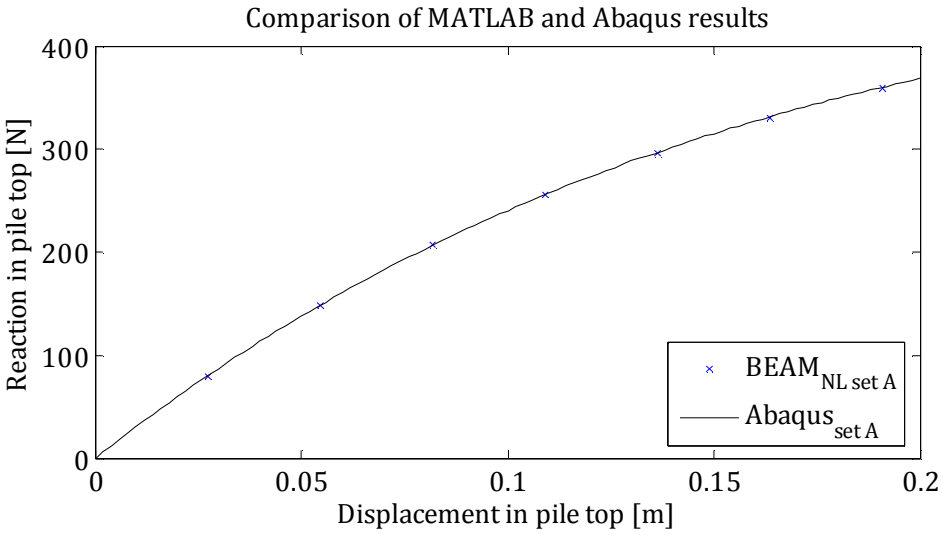

Figure 6.8: Comparison of solutions from Abaqus and MATLAB program using spring set A.

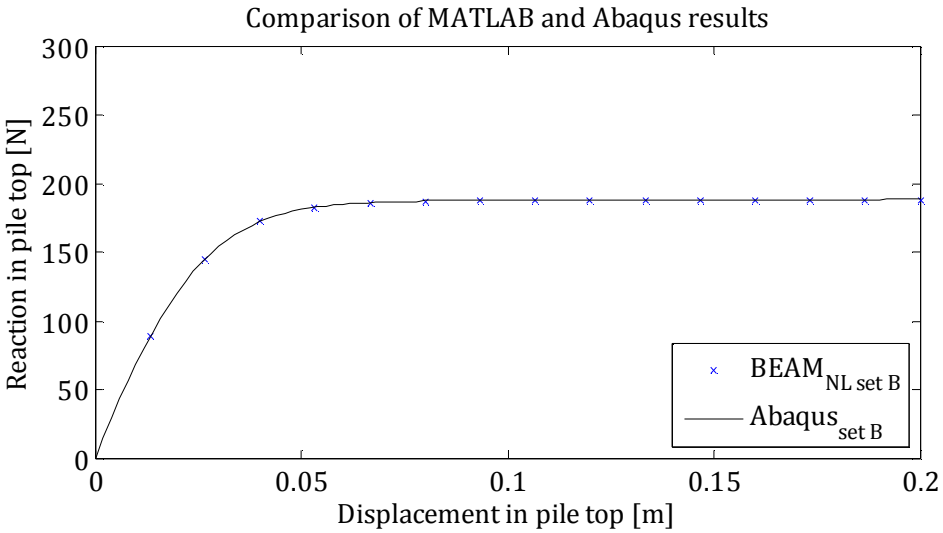

Figure 6.9: Comparison of solutions from Abaqus and MATLAB program using spring set B.

From figure 6.8 and figure 6.9 it shows that there is agreement between the solutions. Therefore it is concluded, that the MATLAB routine works properly and a more complicated model can be constructed.

6.4 Beam model

To describe the pile used in the experiments a model consisting of 41 elements is constructed. The model is referred to as the $BEAM_{NL}$ model. The model is used to investigate the p-y method and the principle of the method. 40 of the elements are evenly distributed below GS and are referred to as soil elements.
As in the reference model springs are attached to the elements directly in the nodes. Here the springs represent the soil, and in each soil element a spring is attached to the bottom node,

hence 40 springs are attached in the levels -0.40 to -0.01. The load is given as a prescribed displacement in the top node. The model is shown in figure 6.10.

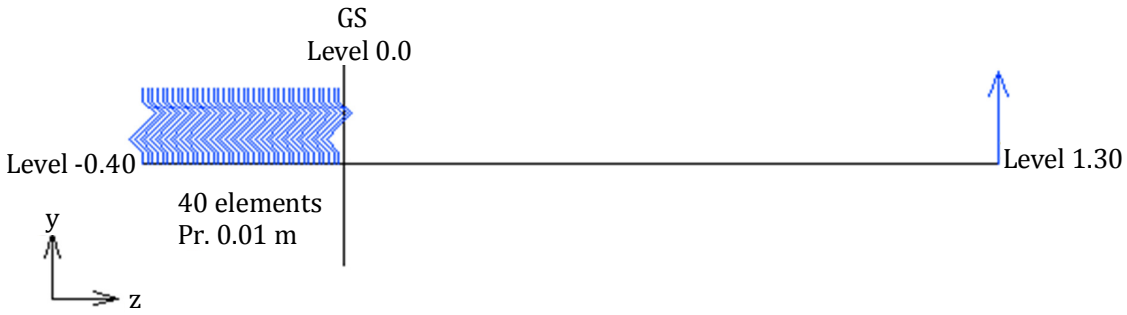

Figure 6.10: BEAM$_{NL}$ model supported by 40 springs and given a prescribed displacement in the top node.

Five sets of nonlinear springs are used as boundary conditions:

- Set 1: Based on the experimental p-y curves presented in section 0 p. 20.
- Set 2: Based on the theoretical p-y curves for dry sand and static lading, given by the API
- Set 3: Based on the theoretical p-y curves for saturated and static loading sand, given by the API
- Set 4: Based on the theoretical p-y curves for dry sand and cyclic lading, given by the API
- Set 5: Based on the theoretical p-y curves for saturated and cyclic loading sand, given by the API

An overview of these five different spring sets is given in table 6.2.

Spring set	Spring type	Soil type	Loading type
1	Experimental	Dry	Static
2	Theoretical (API)	Dry	Static
3	Theoretical (API)	Saturated	Static
4	Theoretical (API)	Dry	Cyclic
5	Theoretical (API)	Saturated	Cyclic

Table 6.2: Overview of the five different sets of springs used in the beam model.

From section 3.5 p. 23 it is seen, that the experimental p-y curves differ from the theoretical curves, both regarding initial stiffness and ultimate bearing capacity. This indicates that the theoretical curves are wrong for the considered depths and stress levels. To further investigate this tendency, the overall response of the 2D model using the theoretical p-y curves is compared to the results from the static tests. This is done for both dry and saturated sand for both static and cyclic loading.

To investigate the principle of the p-y method the overall response of the 2D model using the experimental p-y curves is compared to the results of the static tests. Only in case this response differs significantly from the static results the principle of the p-y method can be rejected.

6.4.1 Set 1 - experimental p-y curves

Experimental p-y curves were determined from laboratory results in the levels -0.4, -0.3, -0.2 and -0.1. In level 0.0 (GS) there is no resistance. For each 0.02 m, experimental p-y curves are interpolated between the measured results, providing 20 different experimental p-y curves to be used in the beam nonlinear Winkler model (BEAM$_{NL}$). The interpolated curves are shown in figure 6.11.

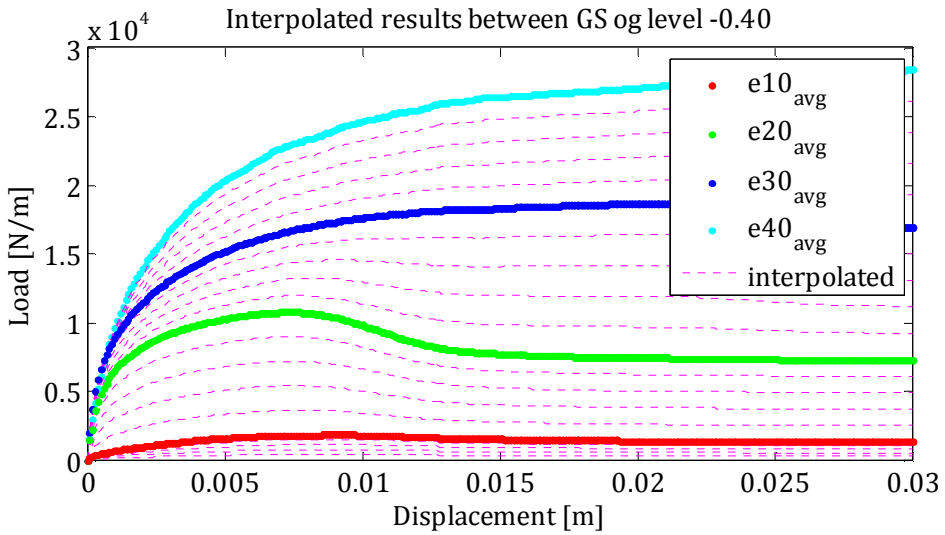

Figure 6.11: Experimental p-y curves interpolated between measured results. The bold curves are the average curves from the p-y experiments.

These 20 experimental p-y curves are approximated with a combination of linear and exponential functions as illustrated in section 3.5 p. 23. This is done for all curves in appendix D.

The approximated functions are all continuous in the intersection points but not differentiable. In the intersection points it is chosen to use the derivative from the left when determining the tangential spring stiffness.

The reason for interpolating new curves is to be able to make a fine discretization. Springs are applied pr. 0.01 m in the depth. Hence, 40 springs are applied but only 20 different springs are determined. It is assessed that applying the same spring in two points above each other is reasonable; for instance the experimental p-y curve determined in level -0.40 is applied in both level -0.40 and level -0.39.

6.4.2 Set 2, 3, 4 and 5 - theoretical p-y curves

Four different sets of theoretical p-y curves are applied in the beam nonlinear Winkler model, see table 6.2. Theoretical p-y curves are determined for both dry and saturated sands for static or cyclic loading respectively. The curves are determined in the depths -0.02 to -0.40 for each 0.02 m as with the experimental p-y curves. The springs are applied in the same way as the experimental p-y springs.

In section 1.2 p. 5 it is described how the theoretical p-y curves are dependent of the angle of friction. In section 2.1.2 p. 15 it is described how the angle of friction varies with depth under low stress levels. Therefore the scale effect associated with low stress level has been taken into consideration when determining the theoretical p-y curves.

The angle of friction consequently is determined for the 20 considered depths and p-y curves are determined in all depths.

The theoretical p-y curves are determined from equation (6.17):

$$p = A \cdot p_u \cdot \tanh\left(\frac{k \cdot z}{A \cdot p_u} \cdot y\right) \tag{6.17}$$

The constants p_u and k differ for dry and saturated conditions.

The empirical adjustment factor, A, differs for static and cyclic load cases in the upper layers:

$$A = \begin{cases} 3.0 - \dfrac{0.8 \cdot z}{D} \geq 0.9, \text{for static loading} \\ 0.9, \text{for cyclic loading} \end{cases} \tag{6.18}$$

In the sets 2 and 3, $A \neq 0.9$, for level -0.01 to level -0.12. In the sets 4 and 5, $A = 0.9$ for all depths. The constants, p_u and k, are not affected by cyclic loading.
In sets 2 and 4, the dry values of p_u and k are used and in sets 3 and 5, the saturated values are used.
p_u in dry sand is determined from an effective soil weight of $\gamma' = 17540$ N/m^3 whereas p_u in dry sand is determined from an effective soil weight of $\gamma' = (20850 - 10000)$ N/m^3, cf. section 2.1.1 pp. 12-15. The value of k is determined from functions fitted to the curves given in the DNV, see section 1.2 p. 5.

6.4.3 Results of the beam nonlinear Winkler model

The results of calculations with the beam nonlinear Winkler model (BEAM$_{NL}$) are used to evaluate the efficiency of the existing p-y method as well as the principle behind the p-y method.

6.4.3.1 Results from undisturbed soil conditions

The results of the BEAM$_{NL}$ model using spring set 1, 2 or 3 are compared to the laboratory results from the static tests s.0.1, s.0.2, s.0.3 and s.0.4 which are all performed in undisturbed conditions, i.e. with no preceding cyclic load. The results are shown in figure 6.12 and figure 6.13.

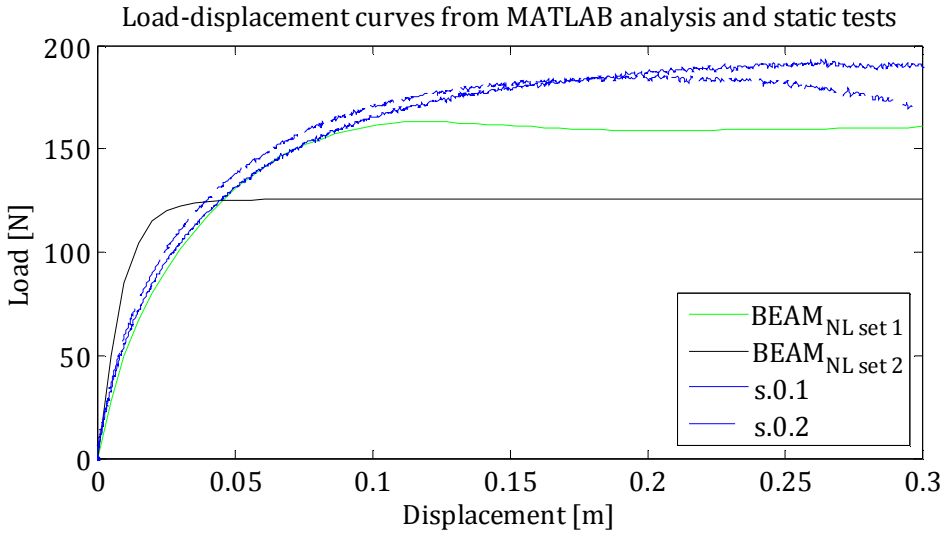

Figure 6.12: Results of BEAM$_{NL}$ model with set 1 (Experimental, dry sand) and 2 (Static loading, dry sand) compared to the experimental results from the static tests with dry sand. Displacement in the pile top.

From figure 6.12 and figure 6.13 it is seen that the p-y method with the theoretical p-y curves provides a solution which is not on the safe side when it comes to predicting displacements to a given load. The results are too steep both in connection with the saturated and the dry sand. However, from figure 6.12 it is seen that the principle of the p-y method is reasonable. This is concluded because the results of the BEAM$_{NL}$ model with the experimental p-y curves are in good agreement with the results of the static tests on dry sand, when comparing to a displacement of up till 0.07 m.
If only the ultimate bearing capacity is of interest, the p-y method using the theoretical p-y curves is on the safe side predicting a maximum load approximately 30 % lower than the actual value determined in the laboratory.

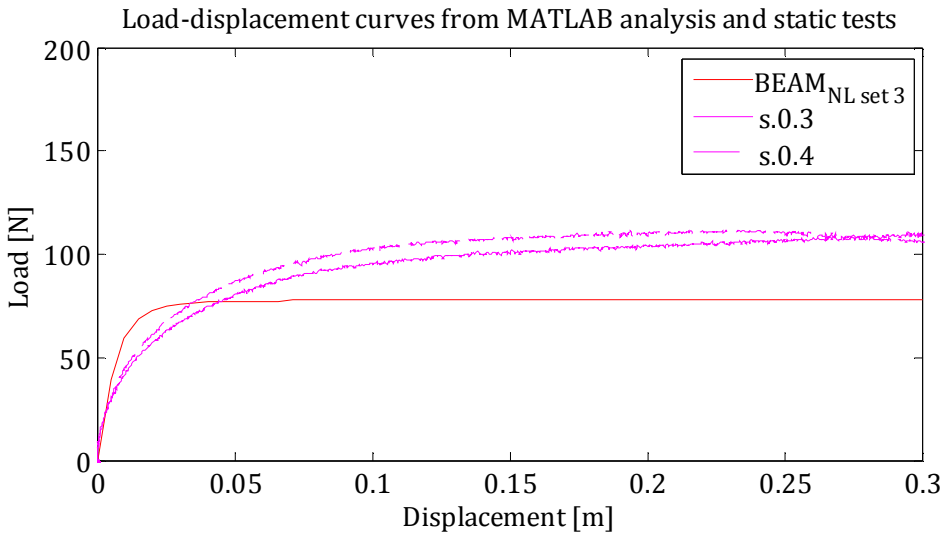

Figure 6.13: Results of $BEAM_{NL}$ model with set 3 (Static loading, saturated sand) compared to the experimental results from the static tests with saturated sand. Displacement in the pile top.

Based on the above observations, it is concluded, that the p-y method with the existing theoretical p-y curves is not in compliance with the experiments. Therefore the warning presented in the DNV, see section 1.3 p. 8, towards using the p-y curves appears to be legitimate. However, it seems that the principle behind the p-y method is very reasonable.

To further investigate the validity of the p-y principle, the bending moments in the pile are considered.

The reactions in the springs and the bending moment in the pile for a displacement of 0.07 m in the top of the pile are shown in figure 6.14.

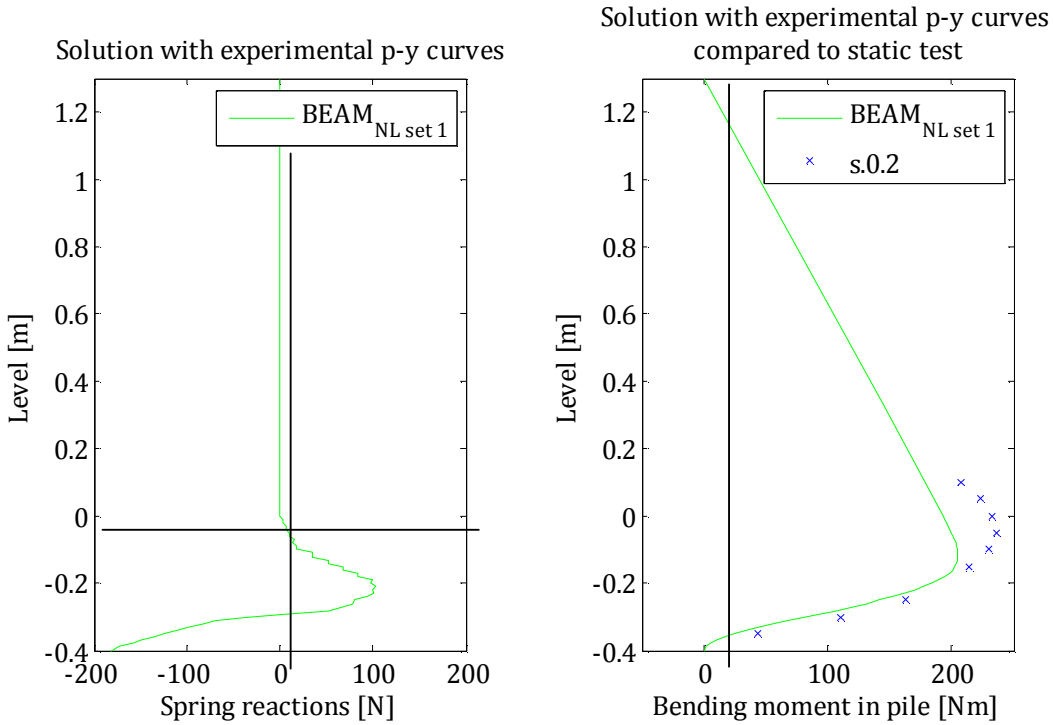

Figure 6.14: to the left: Spring reactions with depth. To the right: bending moment in the pile when displacement is 0.07 m in pile top.

Despite the fact that there is a good agreement between the measured force displacement relationship and the result from MATLAB, the calculated moment distribution differs from the measured. This can be seen from figure 6.14.

The measurements indicate that the maximum moment is located in level -0.05 whereas the MATLAB program indicates a maximum moment in level -0.13. From figure 6.14 it is seen, that the measured bending moment in GS is 232 Nm which is approximately 15 % to high compared to a theoretical value.

With a displacement of 0.07 m the load from the MATLAB program using $BEAM_{NL}$ with set 1 is 148 N. From the results of test s.0.2 the load by a displacement of 0.07 m the load is 153 N. This causes an expected difference between the two results of approximately 3 %. Therefore this does not explain the total mismatch between the results, and in section 4.3.2 p. 31 it is described how the strain gauges are not totally reliable.

When mounting the strain gauges a bit of material is removed due to grinding, but in order for this to explain the deviation, 0.2 mm material should have been removed. Another effect which has influence of the bending stiffness is ovalization during loading. It is assessed that neither of these two effects can explain the deviation in the point of maximum bending moment.

To achieve the measured distribution with the MATLAB program it requires an unrealistic increase in strength of the upper springs which is far more than can be justified by the dispersion of the experimental p-y curves. To illustrate this, the upper four springs have been increased in strength by multiplying with a constant, c. This is shown in figure 6.15.

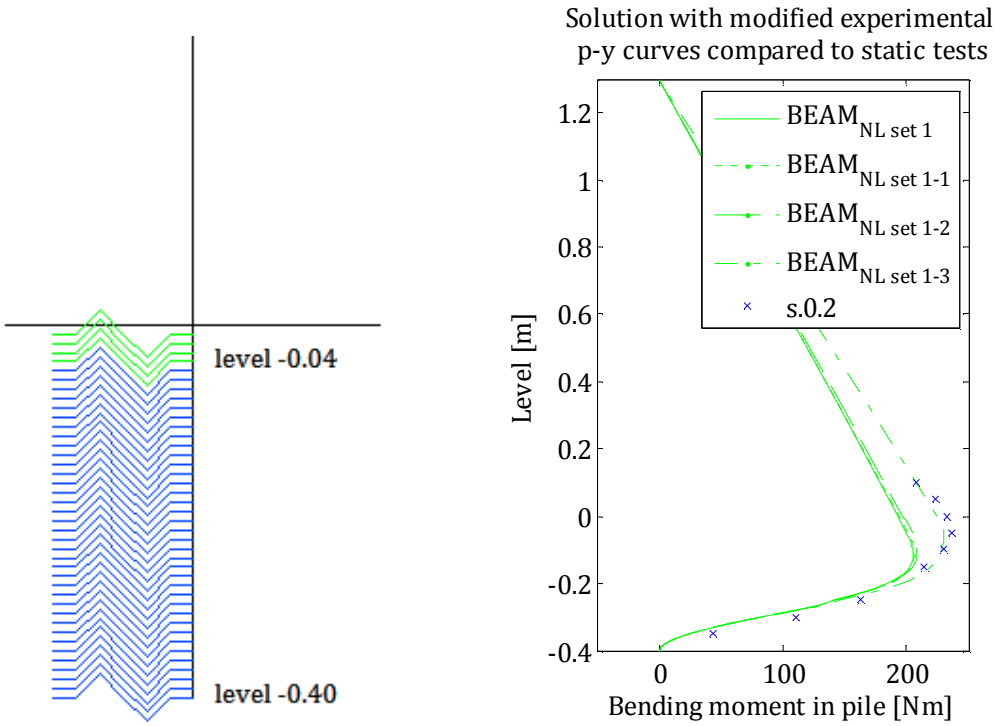

Figure 6.15: To the left: The four uppermost springs are placed in level -0.04 to -0.01 and marked with green. To the right: Distribution of bending moment in the pile when multiplying the uppermost four springs with a constant, c. $BEAM_{NL\ set\ 1}$: c=1, $BEAM_{NL\ set\ 1\text{-}1}$: c=1.3, $BEAM_{NL\ set\ 1\text{-}2}$: c=2, $BEAM_{NL\ set\ 1\text{-}3}$: c=8,

From figure 6.15 it is seen, that tuning the upper four springs of the model within reasonable margins does not change the distribution of the bending moment within the pile.
Therefore the deviation between the two curves is indeed hard to explain.

6.4.3.2 Results from disturbed soil conditions (preceding cyclic test)

The results of the beam nonlinear Winkler model ($BEAM_{NL}$) using spring sets 4 and 5 are compared to the laboratory results from the static tests sc.1.1- sc.1.3, sc.2.1, sc.2.2, sc.3.1, sc.3.2, sc.4.1 and sc.4.2, which are all performed in disturbed soil conditions from preceding cyclic tests.

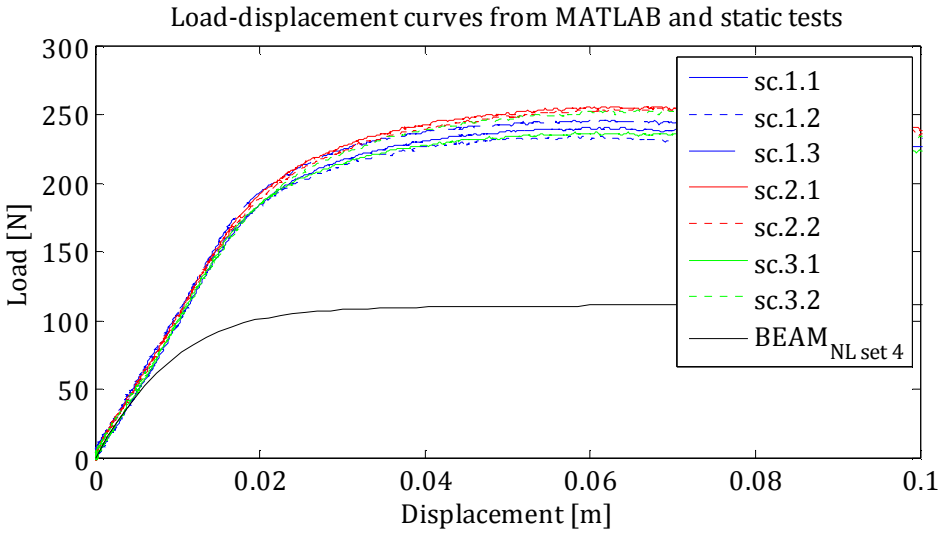

Figure 6.16: Results of $BEAM_{NL}$ model with set 4 (Cyclic loading, dry sand) compared to the experimental results from the static tests with dry sand. Displacement in the pile top.

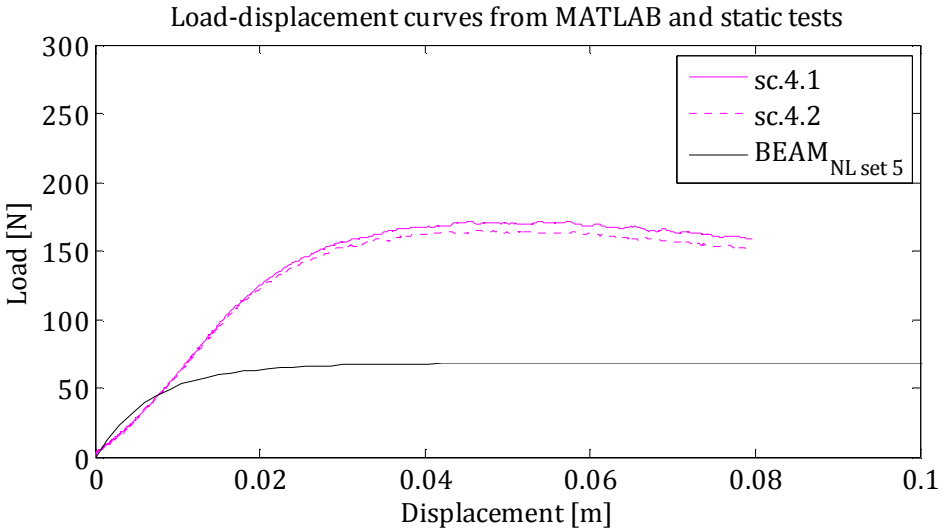

Figure 6.17: Results of $BEAM_{NL}$ model with set 5 (Cyclic loading, saturated sand) compared to the experimental results from the static tests with saturated sand. Displacement in the pile top.

From figure 6.16 and figure 6.17 it is seen, that the response curves calculated with the $BEAM_{NL}$ model using spring sets 4 or 5 almost have the same steepness as the experimental curves. However, the ultimate bearing capacity is highly underestimated using the theoretical p-y curves. It seems that in disturbed soil conditions, the theoretical solution is on the safe side.

6.5 Conclusions

The MATLAB routine is working as intended and is suitable for the considered type of problem. The response using the theoretical p-y curves does not correspond to the laboratory results. In

undisturbed soil conditions, the solution is not on the safe side considering the displacements because the calculated response is too steep.

The steepness of the response calculated from theoretical p-y curves agrees with the steepness of the measured response from the static tests performed after cyclic loading. Yet, the value of the ultimate bearing capacity is too low, and the decrease of the empirical adjustment factor, A, in the upper layers is only making this worse.

Using the experimental p-y curves we find perfect agreement between laboratory results and calculated response till a displacement of 0.07-0.10 m in the top of the pile. This displacement corresponds to a gradient of the pile of 2-3°, which is probably beyond application area. This reveals that the p-y approach is all-right.

7 3D model of a monopile

In this section the pile is modelled using two different commercial finite element programs. The programs are Abaqus/CAE and Plaxis 3D Foundation.
In both programs the material model for the soil is based on Mohr Coulomb's failure criterion. Therefore this section is introduced with a short description of this theory.

7.1 Mohr Coulomb's theory

The Mohr Coulomb material models are based on perfect plasticity. When a material model is perfectly plastic it means that it has a fixed yield surface, meaning that the parameters are fixed and not dependent on the amount of plastic straining. For stress states that are within the yield surface, the behaviour is fully elastic and therefore all strains are reversible.
The basic principle of elastoplasticity is that the strains are decomposed into elastic and plastic strains and strain rates:

$$\underline{\varepsilon} = \underline{\varepsilon}_P + \underline{\varepsilon}_e \tag{7.1}$$

$$\dot{\underline{\varepsilon}} = \dot{\underline{\varepsilon}}_P + \dot{\underline{\varepsilon}}_e \tag{7.2}$$

Substituting this in Hooks law gives:

$$\dot{\underline{\sigma}}' = \underline{\underline{D}}_e \cdot \dot{\underline{\varepsilon}}_e = \underline{\underline{D}}_e \cdot \left(\dot{\underline{\varepsilon}} - \dot{\underline{\varepsilon}}_p\right) \tag{7.3}$$

The plastic strain rates are proportional to the yield function derived with respect to the stresses. Therefore, the plastic strain rates can be represented as vectors perpendicular to the yield surface. An addition to the yield function has to be introduced in the material models in order to account for non associated plasticity, as associated plasticity overestimates the dilatancy. A more thorough description of this additional function in Plaxis 3D can be found in the Plaxis manual [19]. Figure 7.1 illustrates the basic principal of an elastic perfectly plastic model.

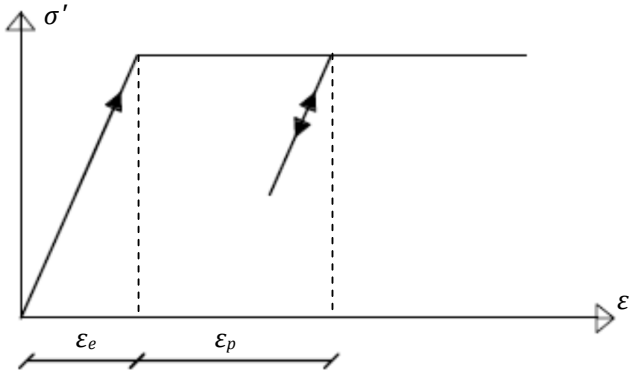

Figure 7.1: Illustration of the basic principal of an elastic perfectly plastic model.

Mohr Coulomb's failure criterion assumes that the failure is controlled by the maximum shear stress and that this depends on the maximum normal stress. The failure criterion with and without cohesion is illustrated in figure 7.2, where the line of failure increases with the friction angle, φ, and intersect the shear axis in the cohesion, c.

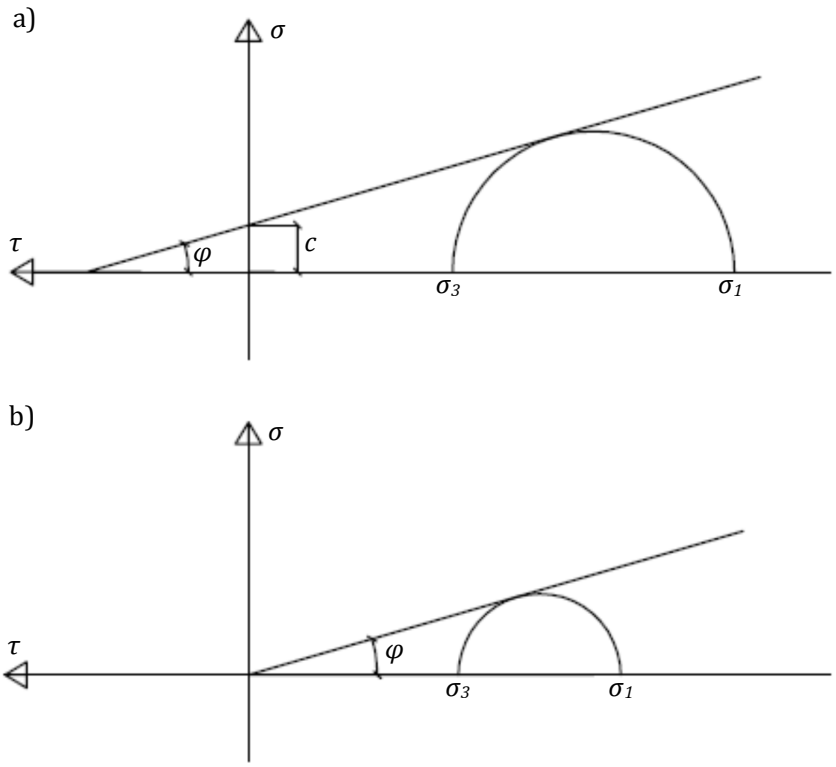

Figure 7.2: Mohr-Coulomb's yield criteria. a) with cohesion, b) zero cohesion. c is the cohesion, φ is the friction angle, τ is the shear stress and σ is the normal stress.

Therefore the yield criterion in one dimension is:

$$\tau = c - \sigma \cdot tan(\varphi)$$

The Mohr-Coulomb failure criterion ensures that the Coulomb friction law is obeyed in any plane within the elements. The full Mohr-Coulomb failure criterion in three dimensions:

$$f_{1a} = \frac{1}{2} \cdot (\sigma'_2 - \sigma'_3) + \frac{1}{2} \cdot (\sigma'_2 + \sigma'_3) \cdot sin(\varphi) - c \cdot cos(\varphi) \leq 0 \tag{7.4}$$

$$f_{1b} = \frac{1}{2} \cdot (\sigma'_3 - \sigma'_2) + \frac{1}{2} \cdot (\sigma'_3 + \sigma'_2) \cdot sin(\varphi) - c \cdot cos(\varphi) \leq 0 \tag{7.5}$$

$$f_{2a} = \frac{1}{2} \cdot (\sigma'_3 - \sigma'_1) + \frac{1}{2} \cdot (\sigma'_3 + \sigma'_1) \cdot sin(\varphi) - c \cdot cos(\varphi) \leq 0 \tag{7.6}$$

$$f_{2b} = \frac{1}{2} \cdot (\sigma'_1 - \sigma'_3) + \frac{1}{2} \cdot (\sigma'_1 + \sigma'_3) \cdot sin(\varphi) - c \cdot cos(\varphi) \leq 0 \tag{7.7}$$

$$f_{3a} = \frac{1}{2} \cdot (\sigma'_1 - \sigma'_2) + \frac{1}{2} \cdot (\sigma'_1 + \sigma'_2) \cdot sin(\varphi) - c \cdot cos(\varphi) \leq 0 \tag{7.8}$$

$$f_{3b} = \frac{1}{2} \cdot (\sigma'_2 - \sigma'_1) + \frac{1}{2} \cdot (\sigma'_2 + \sigma'_1) \cdot sin(\varphi) - c \cdot cos(\varphi) \leq 0 \tag{7.9}$$

The condition $f_i = 0$ for all yield functions together represent a hexagonal cone in principal stress space, see figure 7.3.

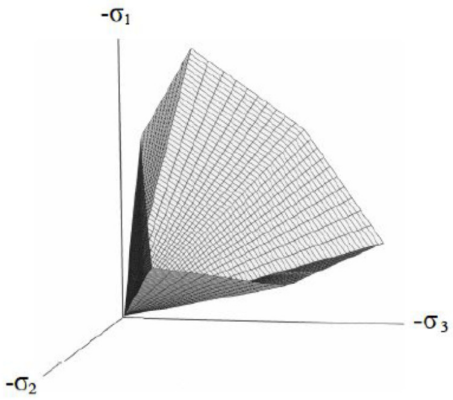

Figure 7.3: The Mohr-Coulomb yield surface in principal stress space, cf. the Plaxis manual [19].

7.2 Modelling the pile using Abaqus

In this section the pile is modelled using the commercial program Abaqus.

7.2.1 Geometry of the model

The modelled monopile is circular with a total length of 1.7 m with 0.4 m below the ground surface and 1.3 m above the ground surface. The diameter of the pile is 0.0508 m and the thickness is 0.0015 m. This is in accordance with the experiments, see section 2, p. 12.
Three different models are examined: One where the size of the soil domain is the same as the size of the box used in the experiments and two models where the soil domains are larger than the box. The models with the three different soil domains are shown in figure 7.4 where symmetry around the x-axis has been used.

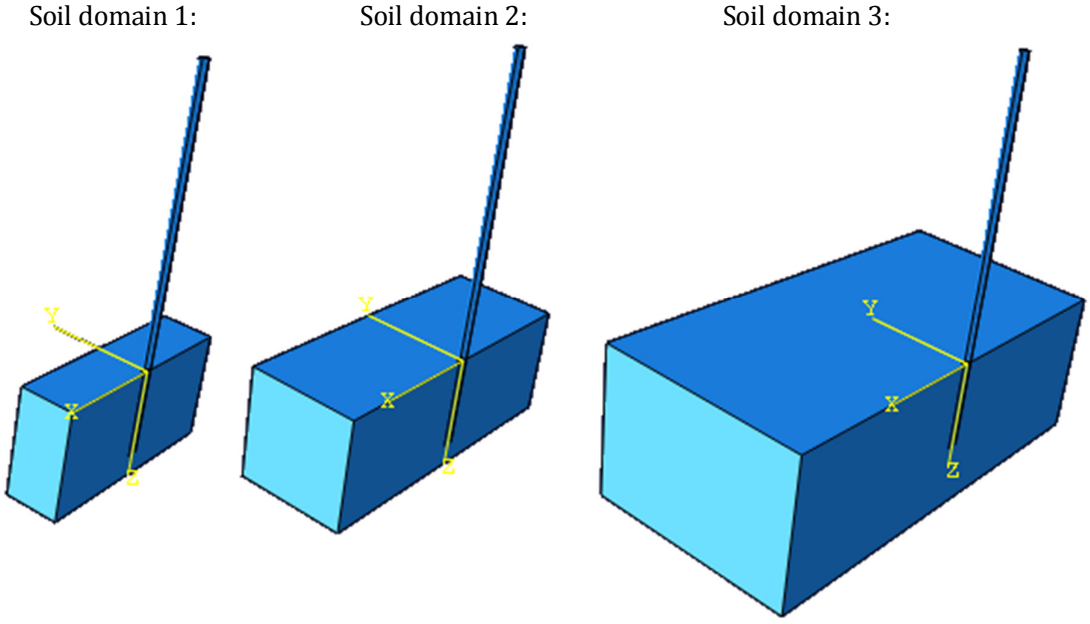

Figure 7.4: Illustration of the three different sizes of soil domain. Both with symmetry around the x-axis.

It is seen that soil domain 3 is larger than soil domain 2 in all directions, also below the bottom of the pile.
This examination is made to investigate whether there are boundary effects from the edges of the soil domain in the model and determine the consequences of possible boundary effects.

7.2.2 Material parameters

The pile is a steel pile with young's modulus of $2.1 \cdot 10^{11}$ N/m^2 and poison's ratio 0.3.

In appendix M two different material models are examined for a circular footing placed on top of a soil domain. The examined material models are both based on Mohr Coulomb's failure criterion. One of the material models is incorporated in the Abaqus materials and the other is a user defined material model. The conclusion of the analysis in appendix M is that the user defined material model is the most stable and it produces the best results compared to theoretical failure loads.
The input parameters in the user defined material model are the friction angle, the dilatation angle, young's modulus, the cohesion and Poisson's ratio. Even though the dilatation angle is an input parameter, the material model does not work when using non associated plasticity. Therefore the friction angle is determined as the modified friction angle, see figure 2.6, p. 17.
The soil domain is divided into layers because the friction angle and the dilatation angle changes with depth cf. section 2.1.2, p. 15. The layers have equal thicknesses and the material parameters are found in the middle of each layer. The layers are illustrated in figure 7.5.

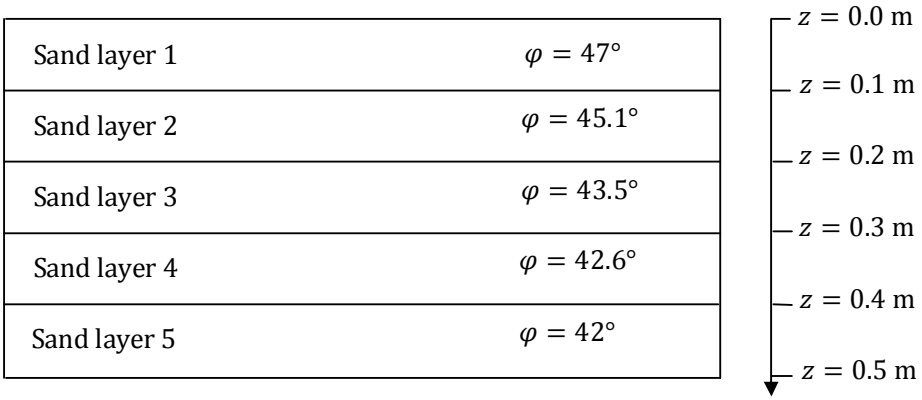

Figure 7.5: Illustration of the five different layers of sand in the 3D model.

The material parameters for the five different sand layers are shown in table 7.1.

Sand layer	Friction angle, φ_{mod} [°]	Dilatation angle, ψ [°]	Cohesion, c [N/m^2]	Modulus of elasticity, E [kN/m^2]	Density, γ [kN/m^3]	Poisson's ratio, ν
1	47	47	0	$4 \cdot 10^6$	17.54	0.3
2	45.1	45.1	0	$4 \cdot 10^6$	17.54	0.3
3	43.5	43.5	0	$4 \cdot 10^6$	17.54	0.3
4	42.6	42.6	0	$4 \cdot 10^6$	17.54	0.3
5	42	42	0	$4 \cdot 10^6$	17.54	0.3

Table 7.1: Material parameters for the sand in the 3D Abaqus model of the pile.

7.2.3 Boundary conditions and contact

The contact between the soil domain and the pile is modelled as bonded by merging the two parts.

In the model, symmetry around the x-axis is used and therefore, the symmetry surfaces of the pile and soil domain must be constrained in the y-direction. The edges of the soil domain must also med constrained. The boundary conditions in the model are shown in figure 7.6.

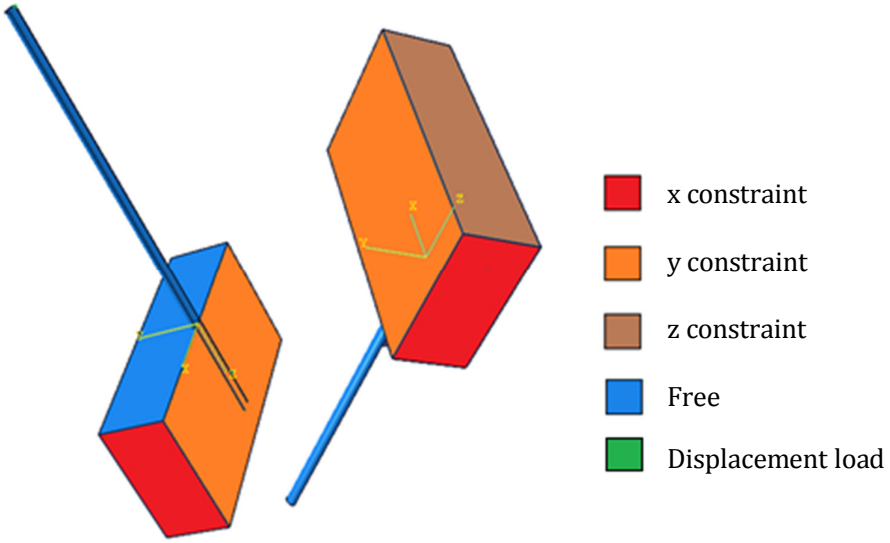

Figure 7.6: Boundary conditions in the Abaqus model of the pile.

The model is loaded by a displacement in the x-direction at the top of the pile.

7.2.4 Mesh

For the model with soil domain 1, two different mesh coarsenesses are examined. The meshes are shown in figure 7.7.

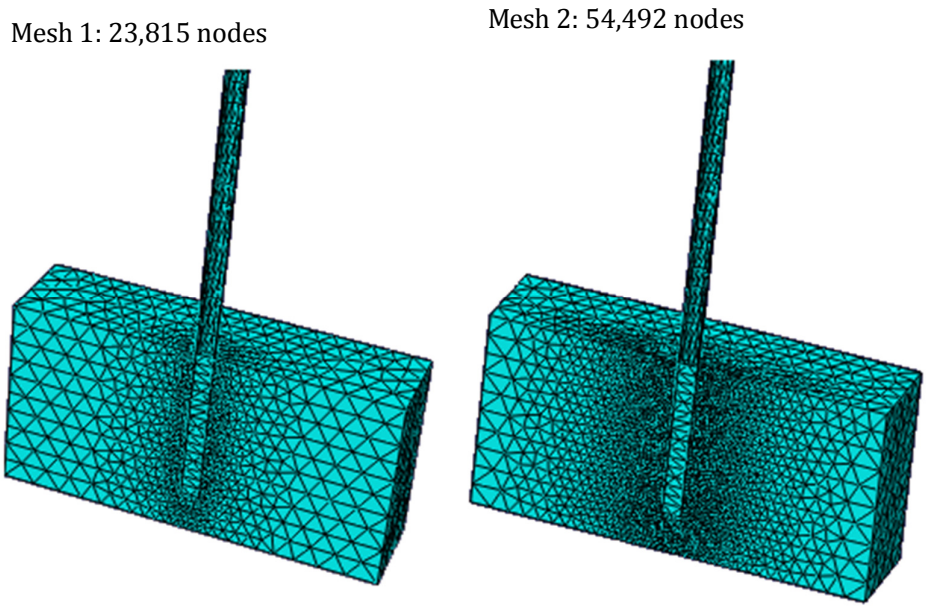

Figure 7.7: The two different coarsenesses of the mesh for soil domain 1.

7.2.5 Geostatic step

The overburden pressure increases with increasing depth; this means that the weight of the sand must be included in the model. When the gravity is activated in the model this induces displacements of the soil domain, and these displacements can cause disturbance of the analysis. This is taken into account in a geostatic step where initial stresses are calculated for the soil domain. These stresses have the same values but with opposite signs of the stresses coming from the gravity load. Therefore, the total stresses and displacements will be equal to zero at the end of the geostatic step.

The initial stresses are determined in a FORTRAN script where the vertical initial stresses are computed from:

$$\sigma_z = \gamma \cdot d \tag{7.10}$$

Where:

d is the depth [m]

γ is the density of the soil [kg/m^3]

The stresses perpendicular to the vertical stresses are determined as:

$$\sigma_x = \gamma \cdot d \cdot K_0 \tag{7.11}$$

$$\sigma_y = \gamma \cdot d \cdot K_0 \tag{7.12}$$

where:

$K_0 = 1 - sin(\varphi)$ is the earth pressure coefficient at rest

The first calculation step after the initial step is the geostatic step. Figure 7.8 shows that the displacements are close to zero at the end of the geostatic step.

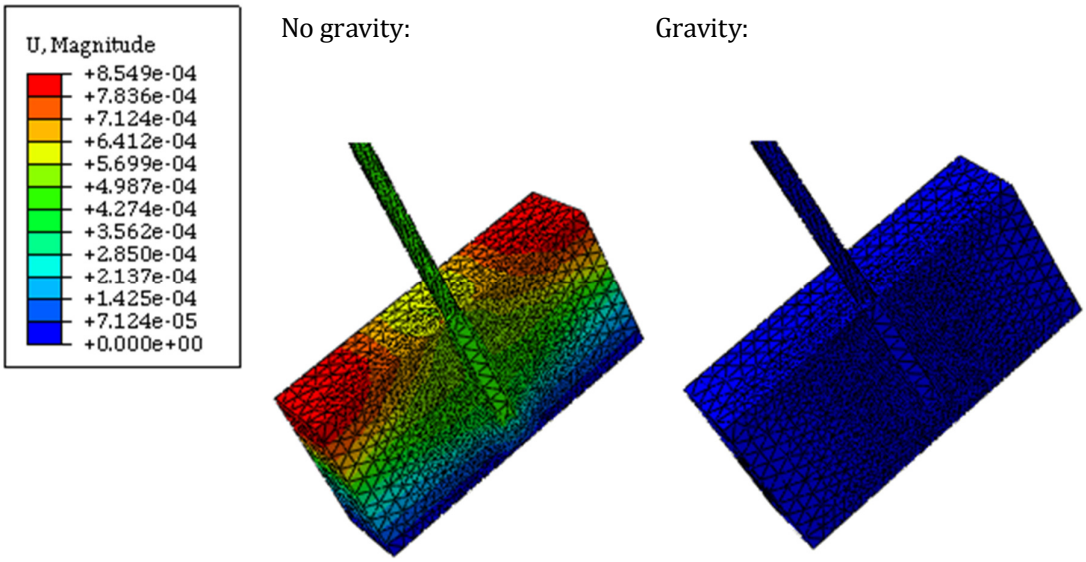

Figure 7.8: Total displacements in the model at the end of the geostatic step with no gravity load to the left. To the right: Displacements at the end of the geostatic step with the gravity load activated. When the gravity load is active the displacements has a magnitude of $1 \cdot 10^{-7}$ m. The displacements on the figure are in m.

7.2.6 Results

The results are compared to and to experimental results and the theoretic solution by applying the API p-y curves in the beam program. All displacements and loads are at the top of the pile and in the x-direction.

The load-displacements curves for the analyses of the model with soil domain 1 and the two different meshes are shown in figure 7.9 and figure 7.10.

The figures show that the mesh has some influence of the results for large displacements but it has no influence of the initial slope of the curve. The following analyses are carried out with a mesh coarseness corresponding to 54,492 nodes with soil domain 1.

The analyses with the three different soil domains are compared for the mesh coarseness corresponding to 54,492 nodes with soil domain 1. The results are shown in figure 7.11.

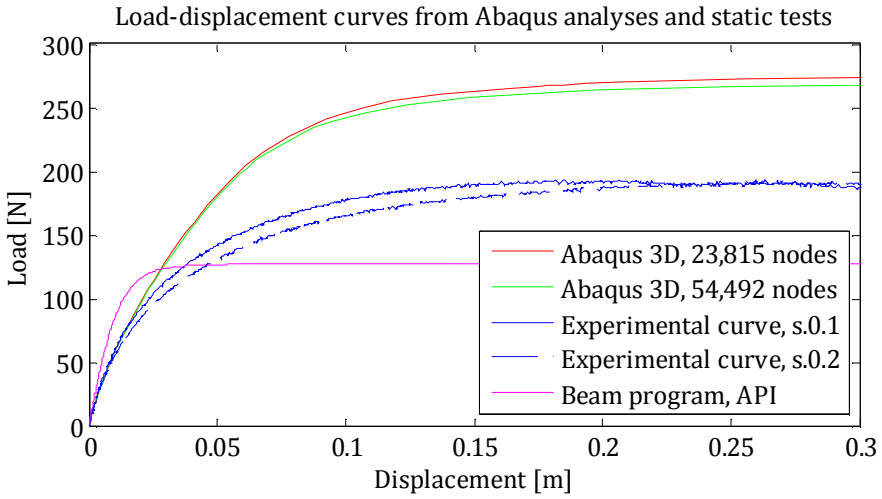

Figure 7.9: Load displacement curve for the analysis's of the model with soil domain 1 and the two different meshes. The experimental curve and theoretical solutions are also displayed.

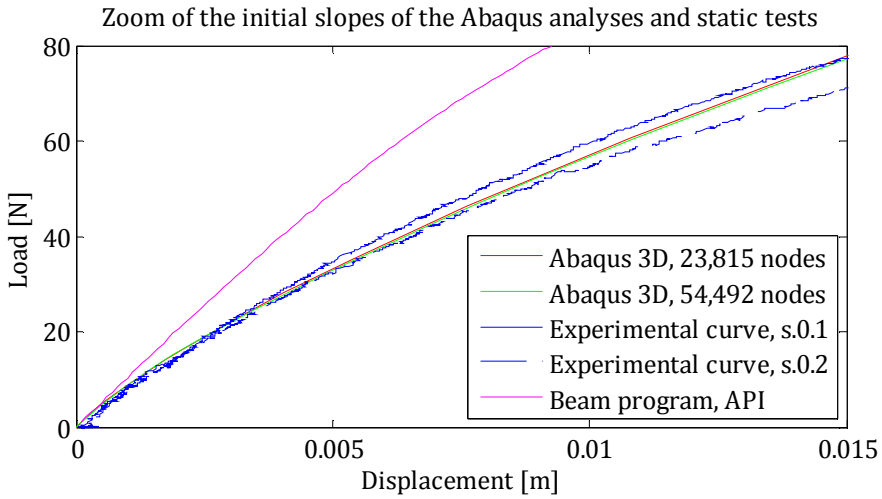

Figure 7.10: Zoom of the initial slope for the analyses of the model with soil domain 1 and the two different meshes. The experimental curve and theoretical solutions are also displayed.

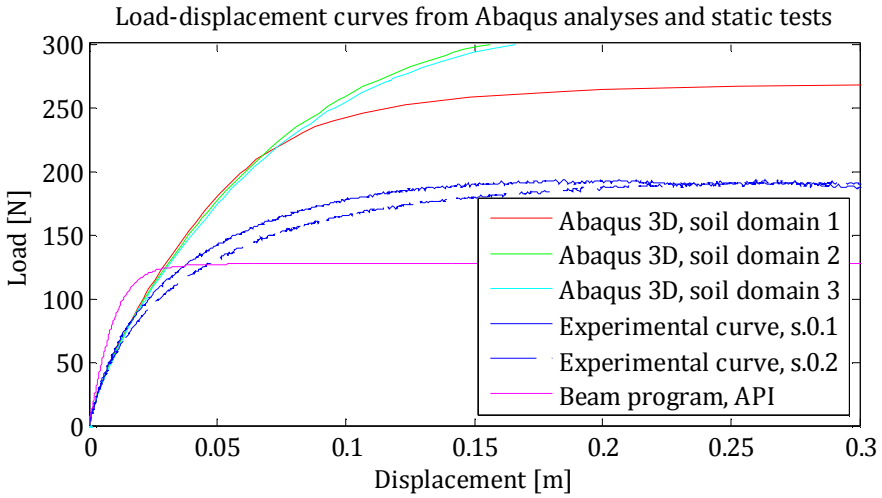

Figure 7.11: Load displacement curve for the analyses of the model with the three different soil domains. The experimental curves and theoretical solution are also displayed.

Figure 7.11 show that the size of the soil domain influences the load-displacement curve. Until the load reaches 220 N the size of the influence of the soil domain on the load-displacement curve is small. When the load reaches 220 N the curve with the smallest soil domain starts going towards a horizontal tangent. The curves for the larger domains keep increasing in force. This means that the size of the soil domain has no significant effect for the initial stiffness of the material.
The failure zones in terms of the plastic strains are shown in figure 7.12.

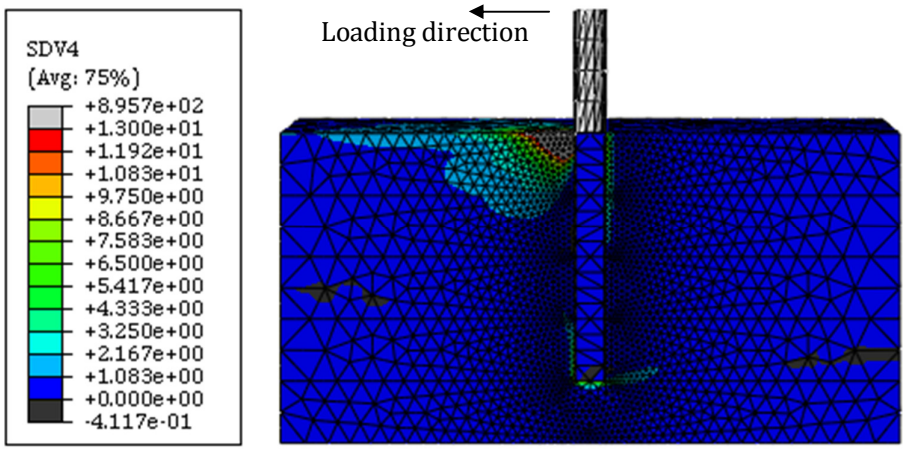

Figure 7.12: Plastic strains in the model of the pile. The model is soil domain 1.

Figure 7.12 show that the plastic strains spread much more in front of the pile than behind the pile. This shows that even though the pile is bonded to the soil, the material model for the soil makes the material very weak when subjected to tension.
The stresses in the x-direction are illustrated in figure 7.13.

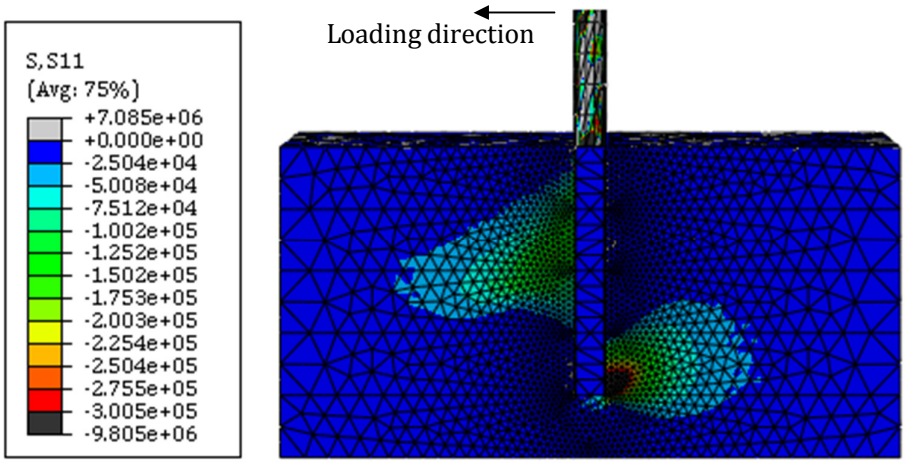

Figure 7.13: Stresses in the x-direction in the model of the pile. The model is soil domain 1.

Figure 7.13 show that the distribution of the stresses beneath the ground surface resembles the distribution of the earth pressure from the 2D beam model, see figure 6.14 p. 56.

7.2.7 Conclusion

The 3D model in Abaqus with the user defined material model for the sand imitates the behaviour of the sand very well when observing the stresses and the plastic strains. Also load displacement curve given by the model is very close to the test results when looking at the initial slope of the curves.

7.3 Modelling the pile using Plaxis 3D Foundation

Plaxis is a finite element program designed to evaluate geotechnical problems.

7.3.1 Geometry of the model

In Plaxis 3D, work planes are perpendicular to the direction of the gravity load. This means that all geometry is modelled from above. The entire work plane and the space in between two work planes represent the soil volume and thereby the volume to be meshed. The negative y-direction represents the direction of the gravity load.
The Dimensions of the works planes in the model are shown in figure 7.14.

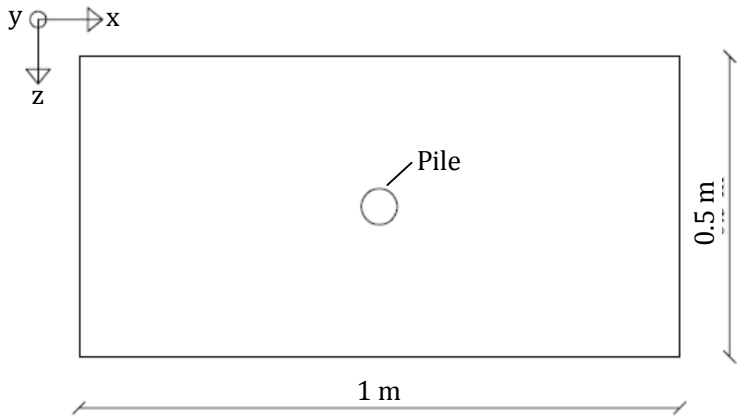

Figure 7.14: Illustration of the dimensions of the work planes in the model.

At first, a borehole is created. The borehole contains information about the soil layer boundaries in the y-direction as well as the material properties for the soil layers. In this case, five soil layers are modelled, see figure 7.15.

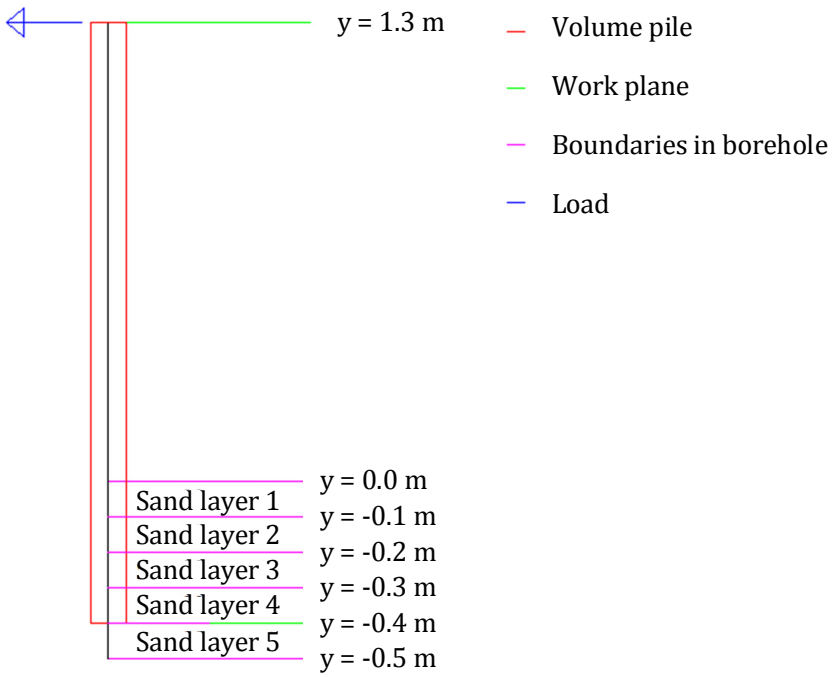

Figure 7.15: Illustration of the different layers of the model in Plaxis 3D and the materials.

The pile is modelled as a volume pile, using shell elements. The user's manual recommends that when modelling volume piles one should create the two work planes, where distance between two work planes corresponds to the length of the pile. Therefore, work planes in y = -0.4 m and y = 1.3 m are created. The volume pile is created in the work plane of y = 1.3 m.
The different levels of the model and the materials they are assigned are shown in figure 7.15.

The model is also examined for a larger soil domain where the work planes are 2 × 1 m and sand layer 5 is from y=-0.4 m to -0.7 m. The 3D models with the two different work plane sizes are shown in figure 7.7.

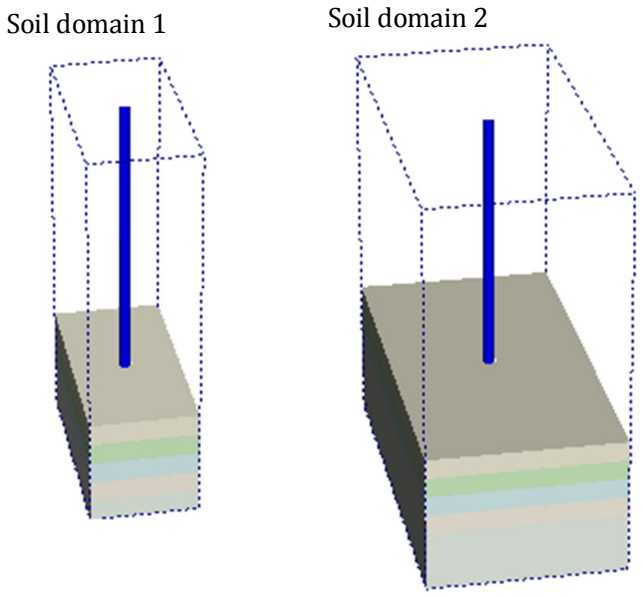

Figure 7.16: Illustration of the two different sizes of soil domains which are examined in Plaxis 3D.

7.3.2 Material parameters

The pile is a steel pile with young's modulus of $2.1 \cdot 10^{11}$ N/m^2 and a poison's ratio of 0.3.

The input parameters in the Mohr Coulomb material model are the friction angle, the dilatation angle, young's modulus, the cohesion and Poisson's ratio.
I Plaxis, it is possible to have a dilatation angle that is different from the friction angle. Therefore realistic values of the dilatation angles are used. This means that the peak friction angles must be used instead of the modified friction angles, see figure 2.6, p. 17.
The soil domain is divided into layers because the friction angle and the dilatation angle changes with depth cf. section 2.1.2, p. 15. The layers have equal thicknesses and the material parameters are found in the middle of each layer. The layers are illustrated in figure 7.15.
The material parameters used in the model are shown in table 7.2.

Sand layer	Friction angle, φ_{peak} [°]	Dilatation angle, ψ [°]	Cohesion, c [N/m^2]	Modulus of elasticity [kN/m^2]	Density [kN/m^3]	Poisson's ratio, ν
1	53.3	23	0	$4 \cdot 10^6$	17.54	0.3
2	51.3	20.4	0	$4 \cdot 10^6$	17.54	0.3
3	49.7	18.6	0	$4 \cdot 10^6$	17.54	0.3
4	48.7	17.7	0	$4 \cdot 10^6$	17.54	0.3
5	47.9	17.1	0	$4 \cdot 10^6$	17.54	0.3

Table 7.2: Material parameters for the sand ind the 3D Abaqus model of the pile.

7.3.3 Boundary conditions and contact

The pile is modelled by shell elements and the contact between the soil domain and the pile is modelled by interface elements. These elements are automatically created when the pile is placed. The properties of the interface elements are default.

7.3.4 Mesh

The model is examined for two different meshes. The two different meshes have 5,807 and 16,581 nodes, respectively. The meshed model with the two mesh coarsenesses are shown in figure 7.17.

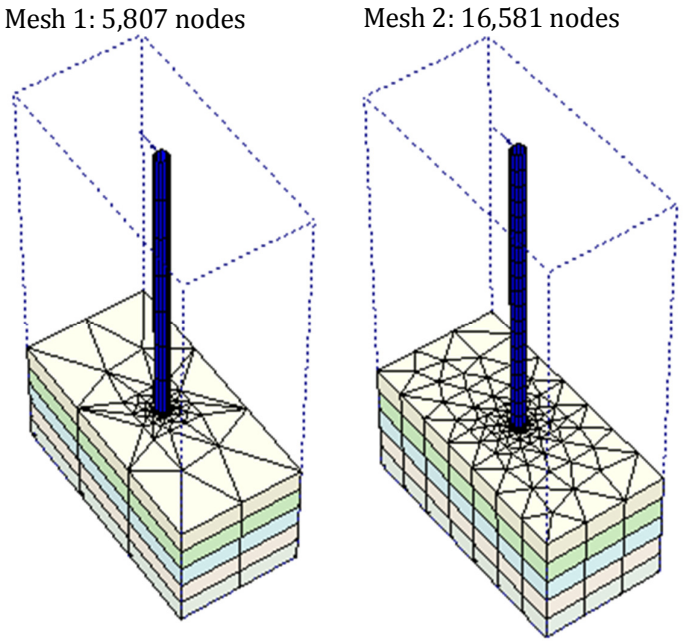

Figure 7.17: 3D mesh of the model in Plaxis 3D. Two different mesh sizes: 5,807 and 16,581 nodes.

7.3.5 Calculation steps

Three different calculation phases are defined in the model. These are shown in table 7.3.

Phase name	What happens
Initial phase	The gravity load is applied and the initial stresses are defined. The displacements are close to zero after this step
Phase 1	The pile is activated in the model
Phase 2	The load is activated in the model

Table 7.3: Description of the three different calculation phases in the Plaxis model.

7.3.6 Results

The results of the Plaxis analyses are compared to the experimental results of the static tests in dry sand. All loads and displacements are at the top of the pile in the x-direction.
Figure 7.18 and figure 7.19 shows the load-displacement curves from the Plaxis analysis with soil domain 1 and the two different meshes. The results of the Plaxis analyses do not resemble the test results very well. The shape of the entire curve is very different and the initial slopes from the Plaxis analyses are linear in the Plaxis analyses, where the test results are much curvier. The mesh is converged at 5,807 nodes and therefore mesh coarseness 1 is used from now on.

Figure 7.20 and figure 7.21 shows the load displacement curves from the Plaxis analyses with the two different sizes of soil domain.

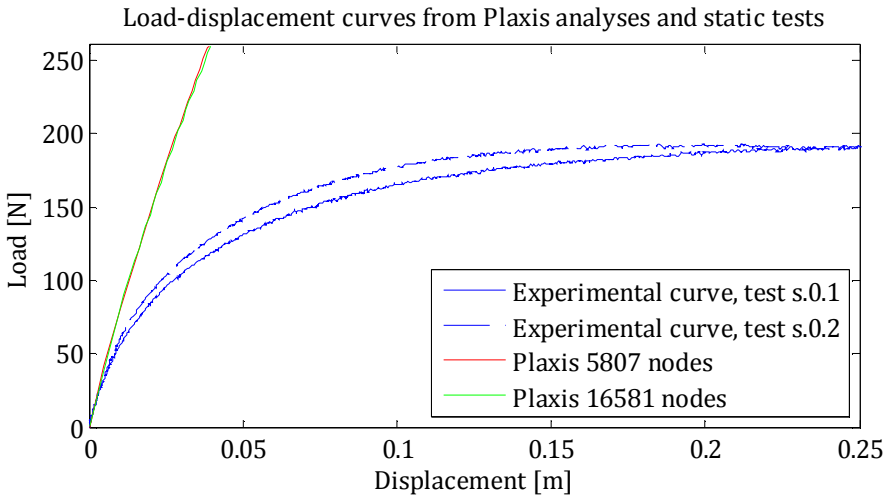

Figure 7.18: Load as a function of displacement from the Plaxis analyses with soil domain 1 and different meshes and the load-curves from the static tests in dry sand.

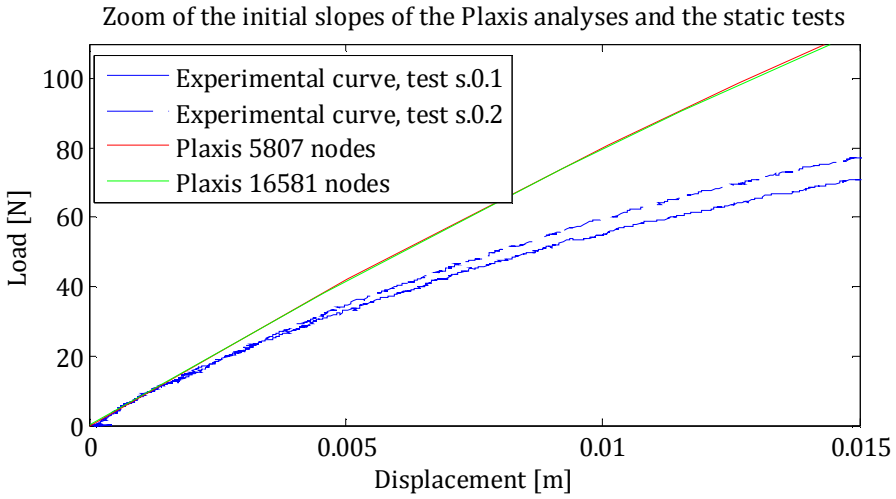

Figure 7.19: Zoom of the initial slopes of the curves from the Plaxis analyses with soil domain 1 and different meshes and the load-curves from the static tests in dry sand.

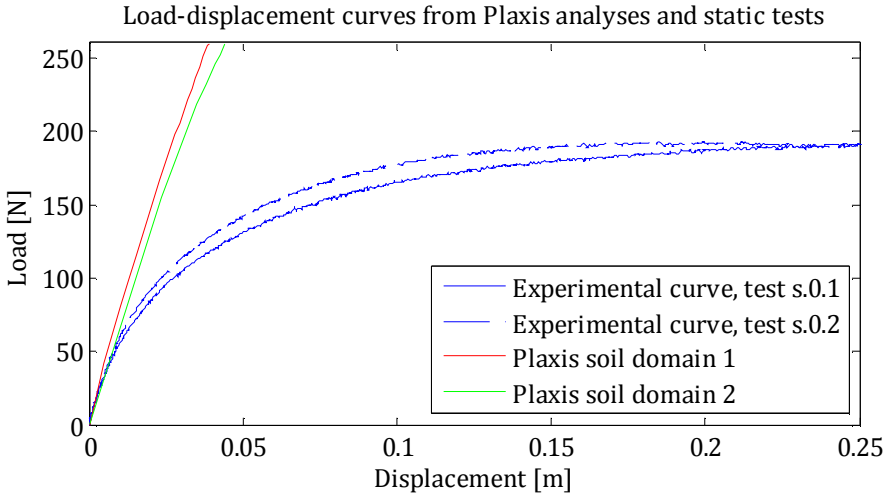

Figure 7.20: Load displacement curves from the Plaxis analyses with soil domain 1 and soil domain 2 with mesh coarseness 1 and the load-curves from the static tests in dry sand.

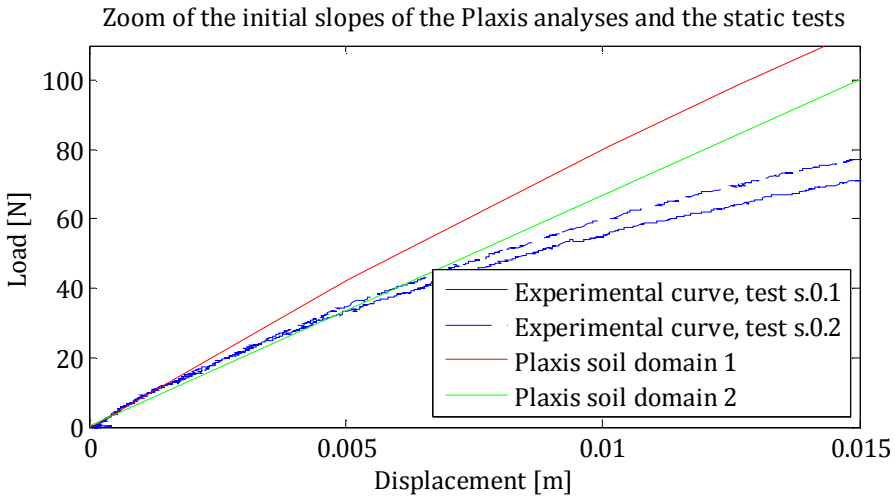

Figure 7.21: Zoom of the initial slopes of the curves from the Plaxis analyses with soil domain 1 and soil domain 2 with mesh coarseness 1 and the load-curves from the static tests in dry sand.

Figure 7.20 and figure 7.21 shows that with a larger soil domain, the stiffness of the load displacement curve is reduced. However the shape of the curve does not change and is still way too linear compared to the experimental curves.

Figure 7.22 shows a contour of the total displacements in the model.

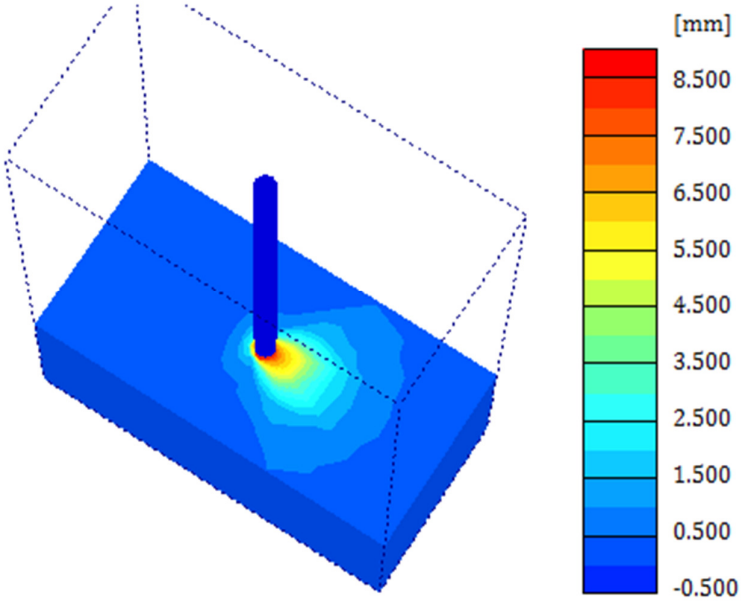

Figure 7.22: Total displacements of the soil in mm.

The contours in figure 7.22 show that the failure zone from the model resembles the figure seen in the experiments.
Figure 7.23 shows the displacements of the soil in the y-direction. The soil moves up in front of the pile and collapses behind the pile.

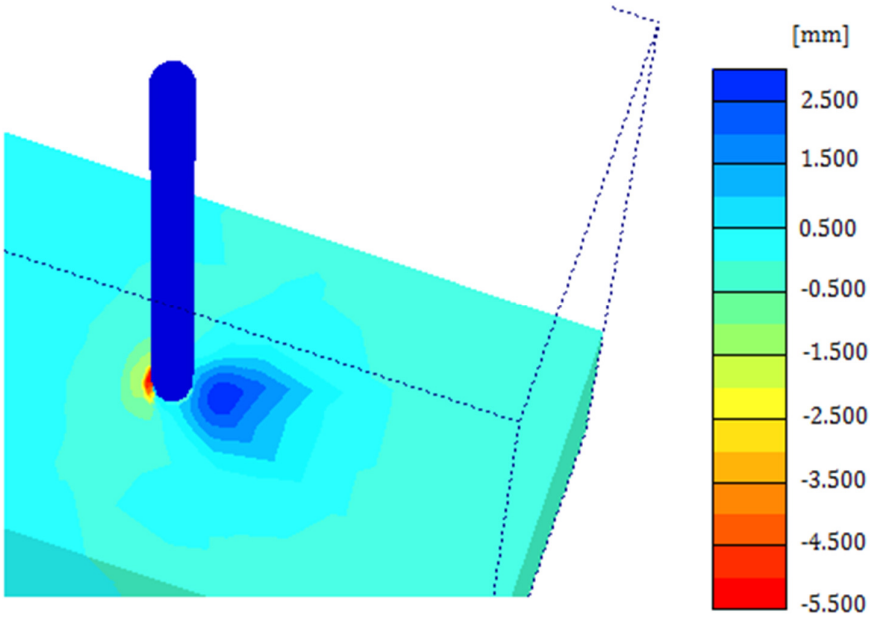

Figure 7.23: Displacements of the soil in the y-direction.

Figure 7.24 shows a contour plot of the stresses in the x-direction in the section midway through pile.

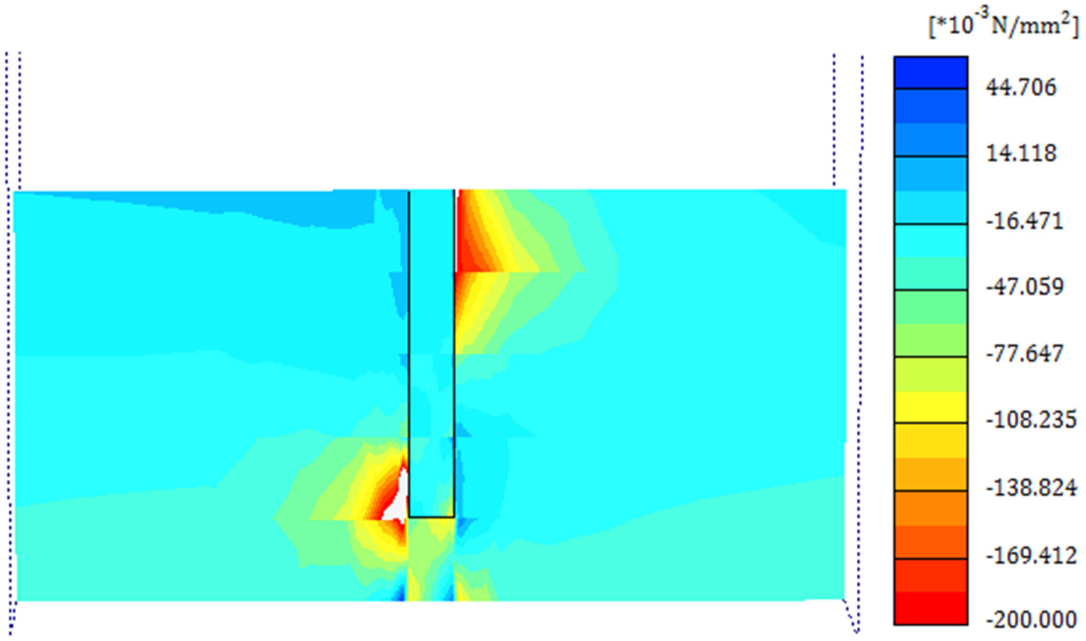

Figure 7.24: Stresses in the x-direction for a section at the centre of the pile. In the white areas the stress is outside of the upper and lower bounds of the contours.

The figure shows that the pile rotates in the soil but the exact point of zero deflection cannot be determined based on the figure. The contours of stresses in the x-direction do not resemble the earth pressure from the beam program as well as the contours of the Abaqus model.

7.4 Conclusion

The load-displacement curves form the Plaxis model show that the stiffness of the soil in the model is too large and the shape is too linear compared to the experimental results. This is the case both for the initial slope of the curves and the entire curve. In the Abaqus model the ultimate resistance is too large compared to the experimental results but the initial slopes of the load-displacement curves are coinciding. The converged element size in the Plaxis model is much larger than in the Abaqus model. This is a plus as the calculation time is short.

As the Abaqus model produces far better results compared to the test results than the Plaxis model and the calculation time is reasonable despite the small element size it is assessed that Abaqus 3D model with a user defined material model is the best for simulating the behaviour of a single pile in dry sand.

8 Discussion

In this section the findings throughout the report are compared are discussed. The FEM models are compared in order to determine advantages and disadvantages of the 2D and 3D models.
The shape of the p-y curves is discussed by comparing the experimental and theoretical curves both directly and the global response.
The results of the cyclic experiments are discussed with regard to the change in secant stiffness.
Finally, the possibility of establishing a 2D FEM model to simulate the behaviour of the sand during cyclic loading is discussed.

8.1 Comparing the FEM models

Two different commercial programs have been used to create a 3D model of the pile: Plaxis 3D foundation and Abaqus/CAE. The Abaqus model gives good results when comparing with the results of the static experiments, but the mesh has to be very fine in order for the model to be correct. This makes the calculation time long compared to both the Plaxis model and the 2D model. But long calculation time is of course relative in relation to the computer capacity.

The 2D nonlinear Winkler model has a very short calculation time and the results are very good. However it only produces good results when the input functions for the nonlinear springs are correct and the existing theoretical functions are not very good. Therefore the problem with the 2D model is that the input functions for the springs cannot be determined with the existing formulas from the API. But if new formulas for the input springs can be created then the 2D Winkler model can be a very efficient tool for determining the response of the soil for offshore wind turbines on monopile foundations.

As the 3D model in Abaqus shows good results we suggest using 3D model to determine new formulas for the p-y curves to be used in 2D modelling.

8.1 Shape of p-y curves

The shape of the theoretical p-y curves is determined from five conditions, see .

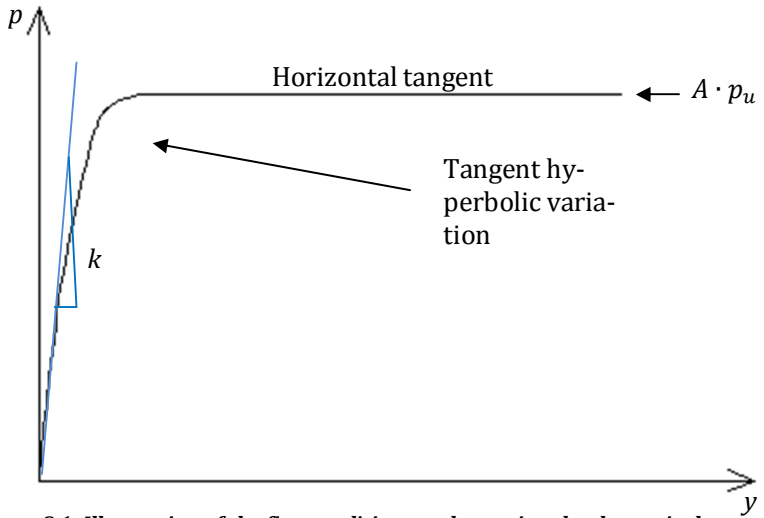

Figure 8.1: Illustration of the five conditions to determine the theoretical p-y curves.

The shape of the p-y curve is tangent hyperbolic. The initial slope of the curve is called the initial modulus of subgrade reaction and denoted k. The ultimate bearing capacity is determined from $A \cdot p_u$ and the p-y curves take horizontal tangent at this value.
The five conditions are:

- Tangent hyperbolic shape
- Initial modulus of subgrade reaction, k
- Horizontal tangent of the p-y curves
- Ultimate bearing capacity $A \cdot p_u$
- Empirical adjustment factor, A

The conditions are discussed separately in order to evaluate the shape of the theoretical p-y curves.

8.1.1 Tangent hyperbolic shape

P-y experiments have been conducted in order to create experimental p-y curves. In section 3.5 p. 23 the experimental p-y curves are compared to the theoretical p-y curves from API. It has been established that the theoretical p-y curves does not fit very well to the experimental p-y curves. For a depth of 0.1 m the initial stiffness of the theoretical p-y curve is too large and so is the ultimate resistance, see figure 3.7.

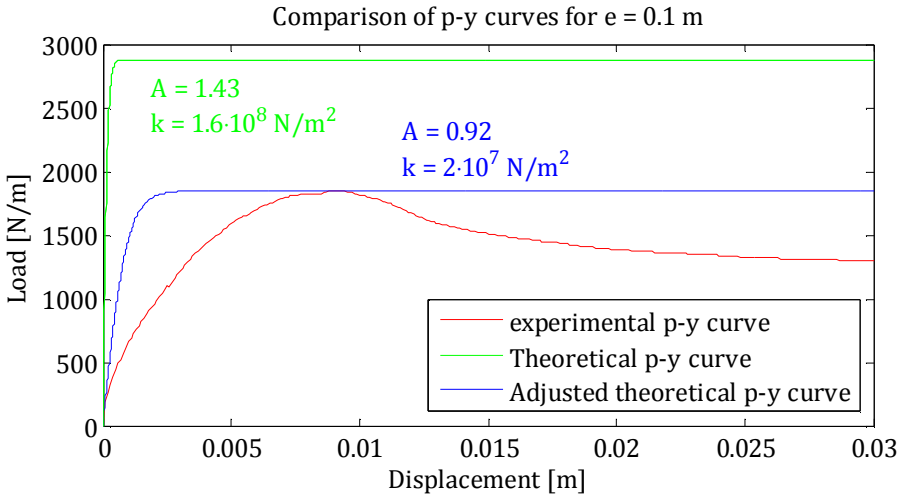

Figure 8.2: Comparison of p-y curves for e = 0.1 m.

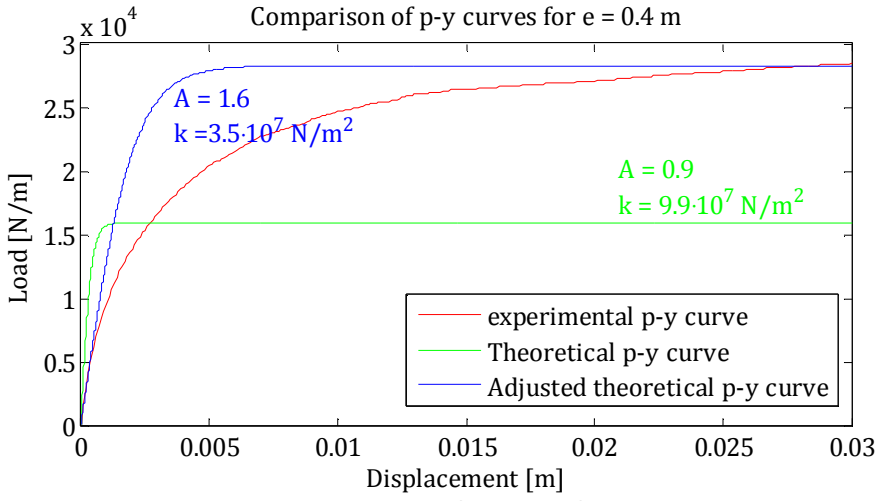

Figure 8.3: Comparison of p-y curves for e = 0.4 m.

For a depth of 0.1 m, the empirical adjustment factor, *A*, is too high and from the figure it can be seen that the ultimate resistance of the theoretical p-y curve would have matched the ultimate resistance of the experimental curve better if the adjustment factor had not been used.

For a depth of 0.4 m the initial stiffness of the theoretical curve is too large and the ultimate resistance is too small, see figure 3.10.

Comparing the curves for depths of 0.2 and 0.3 m shows the same tendencies as for the curves for 0.4 m.

The theoretical values of *k* are generally too large for all depths and the values of *A* are generally too small. Also the shapes of the theoretical curves are not like the shapes of the experimental curves. This indicates that the general method of determining p-y curves needs to be changed.

Adjusting the factors of the initial stiffness and the ultimate resistance shows that the tangent hyperbolic shape is not appropriate, as the curves remain too steep.

8.1.2 Initial modulus of subgrade reaction

So, from the p-y experiments it follows that the theoretical p-y curves are too steep.
Table 8.1 shows the theoretical values of the initial stiffness, *k*, and the values of *k* fitted to the experimental p-y curves. For a constant value of the friction angle the value of *k* is independent of the depth. As the experiments are scale tests, however the friction angle varies with depth and therefore the values of *k* also varies with depth.

The table shows that the value of the initial stiffness decreases with the depth for the theoretical values. This is generally also the case for the fitted values. However, the initial stiffness for depth 0.1 deviates from this tendency. This could be caused by effects in the sand which only happens at very small depths and therefore this effect is not considered in the API for the determination of *k*.

Depth [m]	**Theoretical value of *k*** [N/m²]	**Values of *k* fitted to the experimental curves** [N/m²]
0.1	$1.6 \cdot 10^8$	$2.0 \cdot 10^7$
0.2	$1.2 \cdot 10^8$	$6.3 \cdot 10^7$
0.3	$1.1 \cdot 10^8$	$5.9 \cdot 10^7$
0.4	$0.99 \cdot 10^8$	$3.5 \cdot 10^7$

Table 8.1: Theoretical values of k and values of k fitted to the experimental curves.

From the results of the beam nonlinear Winkler model ($BEAM_{NL}$) this is further confirmed. Another remarkable tendency is the ultimate bearing capacity being too low.
In this section the assumptions for the theoretical p-y curves used as basis of comparison in this report are discussed.

As the experiments are performed in a soil domain dominated by low stress levels, we have extrapolated the formulation of *k* originally presented in the API and the DNV. This is accounted for in section 1.2 p. 5. The formulation of *k* is given by means of the friction angle. The fitted function for *k* is a power function and therefore highly increasing, see figure 8.4.

As described in section 2.1.2 p. 15 the maximum friction angle used is 47°. At 47° the fitted functions estimates a value about twice the value at 40°. This could be an explanation that the p-y curves used are too steep as *k* is the initial modulus of subgrade reaction.

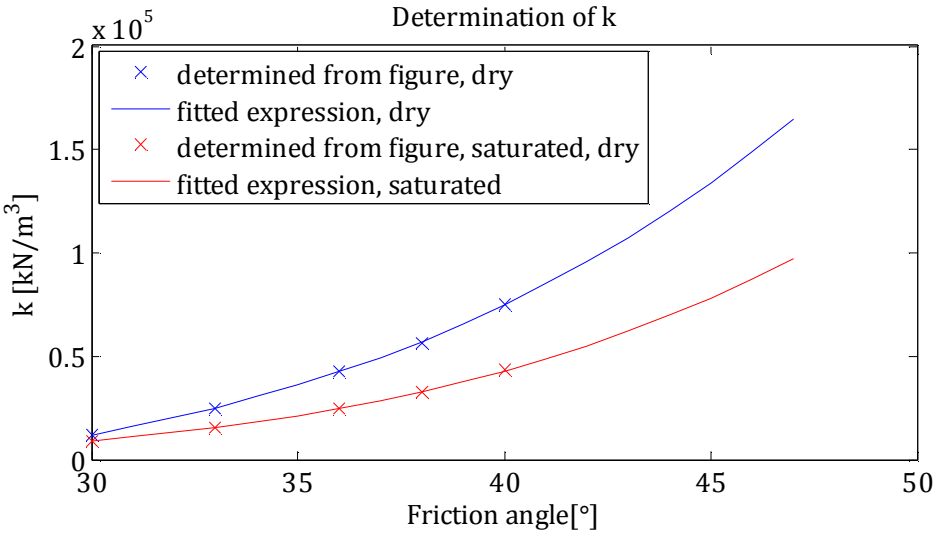

Figure 8.4: The fitted functions for k for dry and saturated sand.

The angle of friction also influences the value of p_u. To investigate the effect of extrapolated values of φ and k it has been tried to use a constant value of φ and consequently a constant value of k in the $BEAM_{NL}$ model. The chosen value of φ used in this investigation is $\varphi = 40°$ which corresponds to a relative density of 0.80, see figure 1.5 p. 5.
The results of the investigation are pictured in figure 8.5.

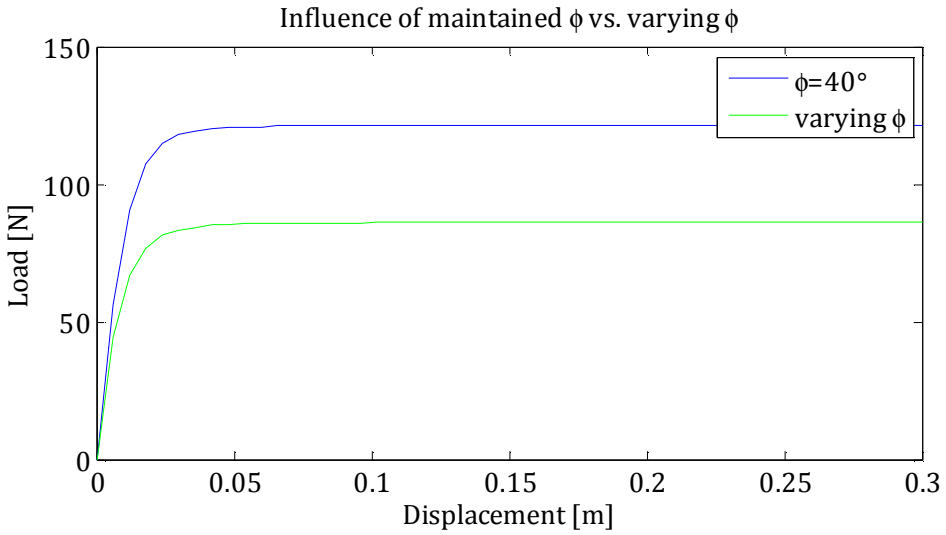

Figure 8.5: Results from $BEAM_{NL}$ for maintained value of φ versus varying value of φ corresponding to the stress level and extrapolated values of k.

From the figure it is seen that maintaining the value of φ does not change the steepness of the curve significantly but the bearing capacity is lowered. That is a consequence of p_u being lower, as the constants, C_1 and C_2, are depending on φ, see figure 8.6.
When discussing the steepness of the p-y curves it should be noted that p-y curves are subtracted from a mix of theory and empirical considerations. Regarding the initial modulus of subgrade reaction one value of this has been defined above the water table and another value below the water table. The experiments in this project are considering completely dry sand. Sand above water table does not necessarily mean completely dry. Sand above water table will under field conditions has a content of water which makes the sand a little cohesive thereby increasing the stiffness compared to completely dry sand.

However, the observations regarding the steepness of the theoretical p-y curves are valid for the saturated case as well, indicating that the stiffness of the theoretical p-y curves is too high after all.

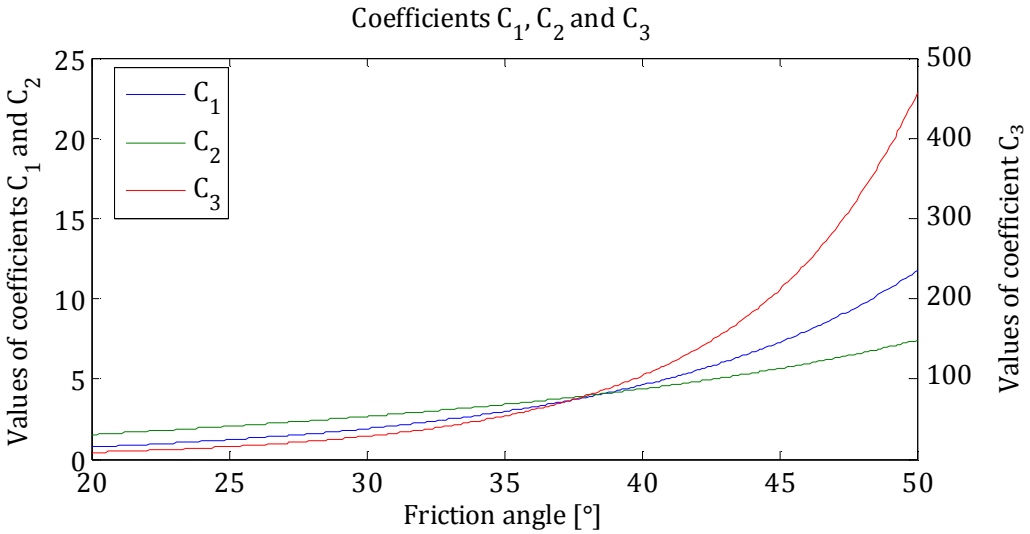

Figure 8.6: Values of coefficients C_1, C_2 and C_3.

8.1.3 Horizontal tangent of p-y curves

The experimental and theoretical p-y curves are used in a beam nonlinear Winkler model ($BEAM_{NL}$) and the response is compared to the results of the static experiments, see figure 8.7. In the figure set 1 means that the functions for the experimental p-y curves are used and set 2 means that the functions for the theoretical p-y curves are used. The figure shows that the results of the beam model using set 1 fits the experimental curves very well until a displacement of about 0.1 m. After this displacement the green curve drops where the experimental curves keep climbing. The drop is caused by drops in the experimental p-y curves. The theoretical p-y curves from the API all get horizontal tangent at the ultimate limit and therefore the experimental p-y curves are modified so that they all get horizontal tangent at the ultimate limit as well. Therefore set 1 – modified means that the experimental p-y curves are used but they are modified so that none of the curves drop in force after the ultimate limit is reached. This is illustrated for one of the experimental curves in figure 8.8.

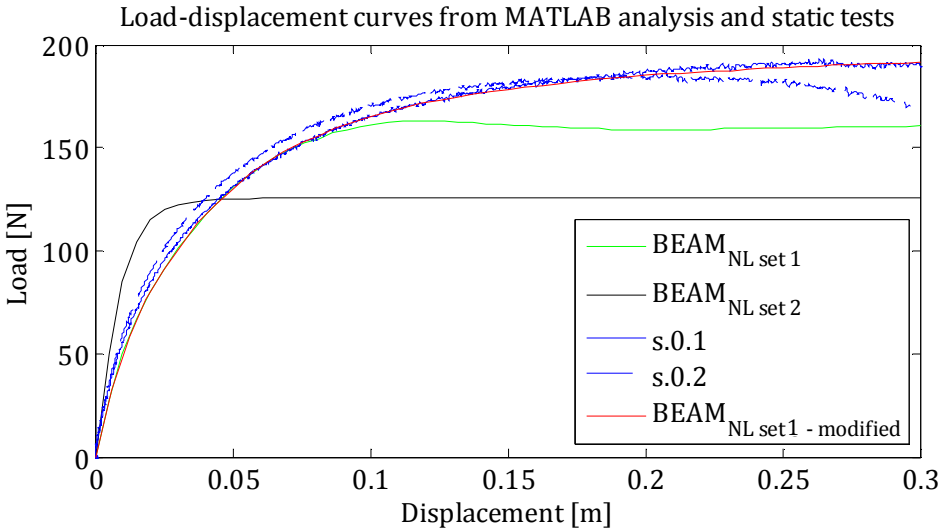

Figure 8.7: Comparison of the results of the beam nonlinear Winkler model ($BEAM_{NL}$) with the results of the static experiments. Set 1 is using the experimental p-y curves and set 2 is using the theoretical p-y curves.

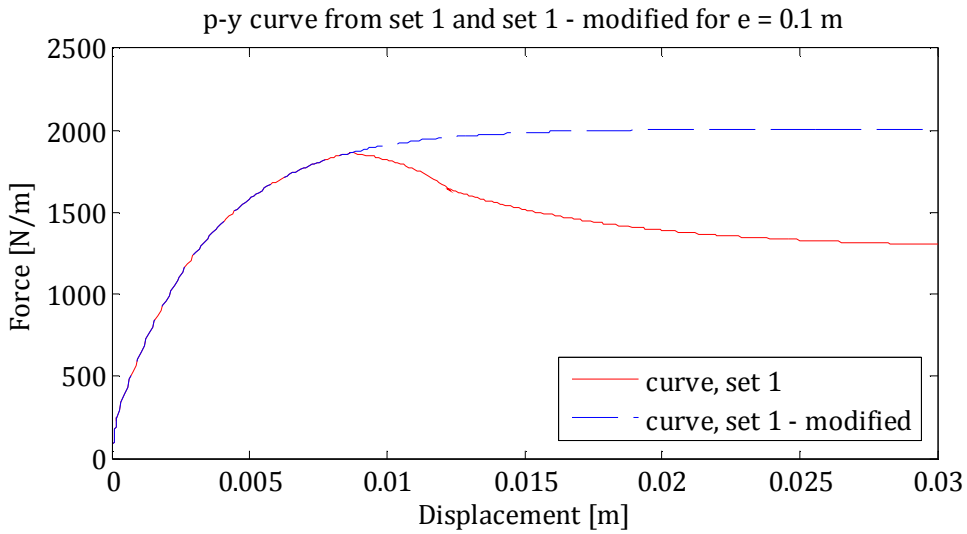

Figure 8.8: Example of p-y curve from set 1 and the set 1 - modified.

In figure 8.7 it can be seen that when the modified set of experimental p-y curves is used the results of the Winkler model are coinciding with the results of static experiment s.0.1.
This indicates that the assumption of a horizontal tangent used in the theoretical formulation of the p-y curves is probably correct.
The reason why there is a drop in the experimental p-y curves could be that failure in the soil develops differently in front of the pile segment than in the static experiments.

8.1.4 Ultimate bearing capacity

An investigation has been made revealing the failure mode in all considered depths is wedge failure, as $p_{us} < p_{ud}$ in all considered depths. In [10] the shape of the wedge used to calculate p_{us} is discussed. Based on this, in section 1.2.1.1 p. 7 the wedge considered in the theoretical formulation is described as something in between a lower bound solution and an upper bound solution. This is illustrated in figure 8.9.

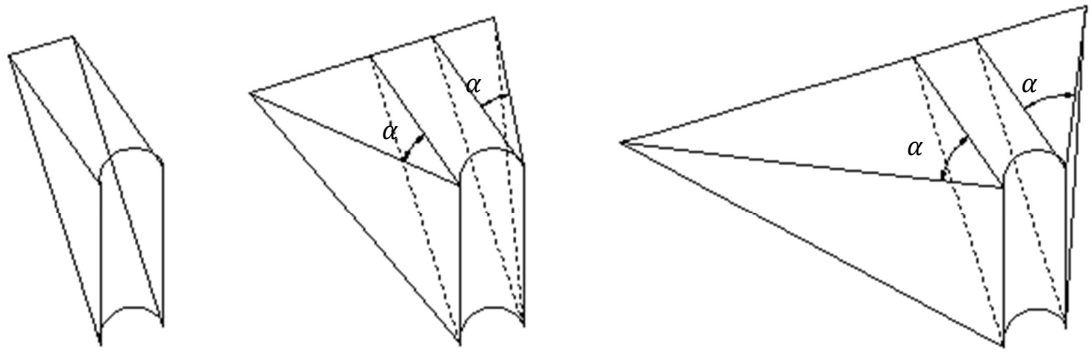

Figure 8.9: Principal illustration of different solution for the failure wedge.

An upper bound solution results in a greater value of p_{us}, hence, the total response will be greater as well. For a lower bound solution the opposite is valid. The condition of wedge failure is assumed maintained and the BEAM_{NL} model is used to evaluate the consequences of the different wedge solutions. The results are shown in figure 8.10.

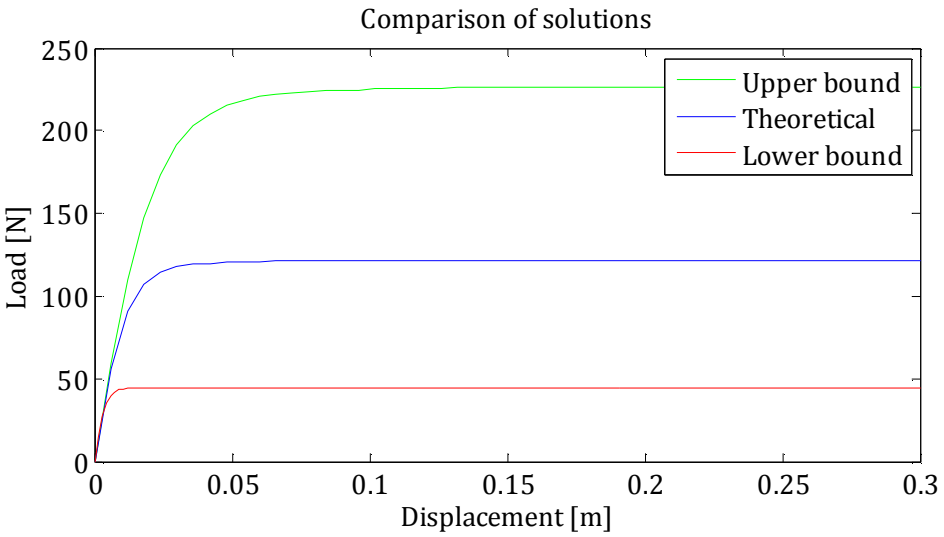

Figure 8.10: Beam solutions for different wedges.

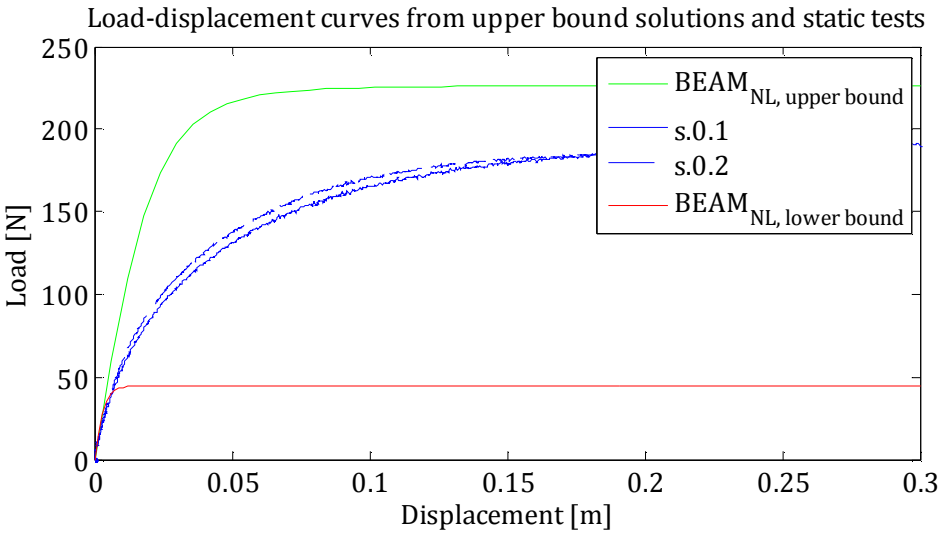

Figure 8.11: Experimental result from test s.0.1, test s.0.2 and BEAM solution using upper bound wedge.

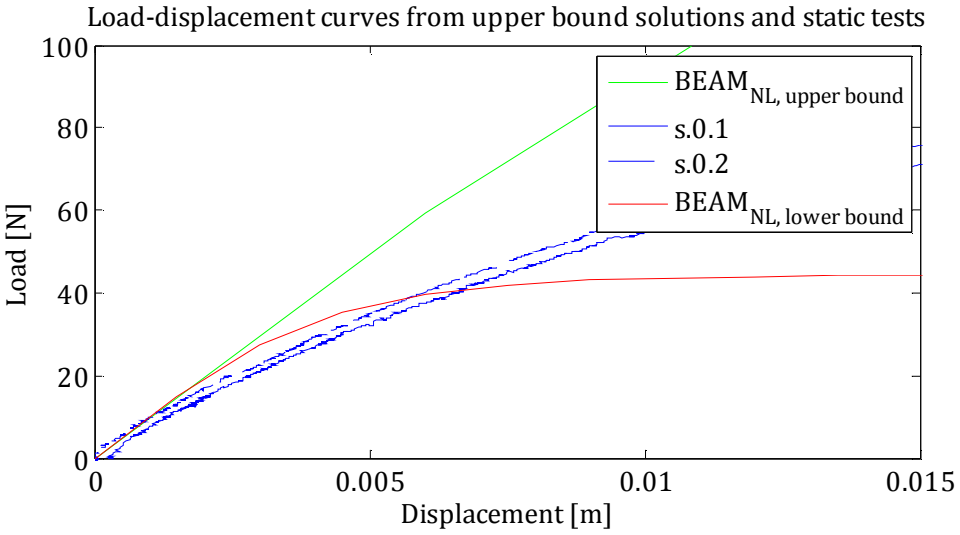

Figure 8.12: Zoom of figure 8.11.

It can be seen from figure 8.10 that an upper bound solution results in a bearing capacity improved by approximately 100 % compared to the wedge solution from the API and DNV. The lower bound solution predicts a bearing capacity of approximately 30 % of the wedge solution from API and DNV. From this evaluation it can be seen that an upper bound solution probably is more correct than a lower bound. This is because the bearing capacity of the upper bound solution resembles the bearing capacity from the experiments more, see figure 8.11. However the shape of the curves is still wrong. It seems as though the lower bound solution is in good agreement with the experimental results within a small displacement. From a zoom of figure 8.11 it can be seen, that this is actually not the case, see figure 8.12.

8.1.5 Empirical adjustment factor

The empirical adjustment factor, *A*, differs for cyclic and static loading. The factor is reduced in the upper layers of the soil for cyclic loading. For the lower layers of the soil the factor is the same as for non-cyclic loading. The global load-displacement curves from the experiments for static loading with and without preceding cyclic loading and the corresponding curves using the theoretical p-y curves are shown in figure 8.13 and figure 8.14 for dry and saturated sand.

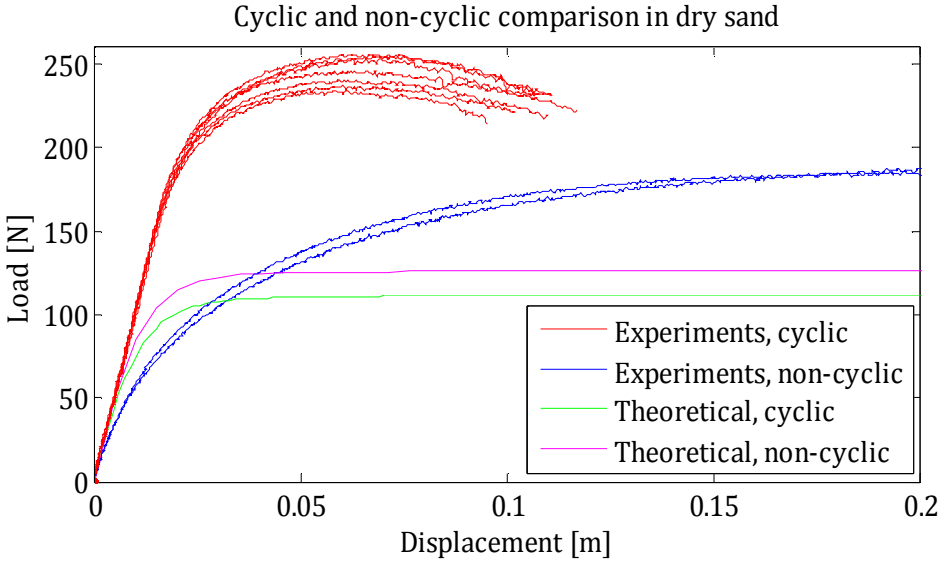

Figure 8.13: Load-displacement curves in dry sand for static loading with and without preceding cyclic loading.

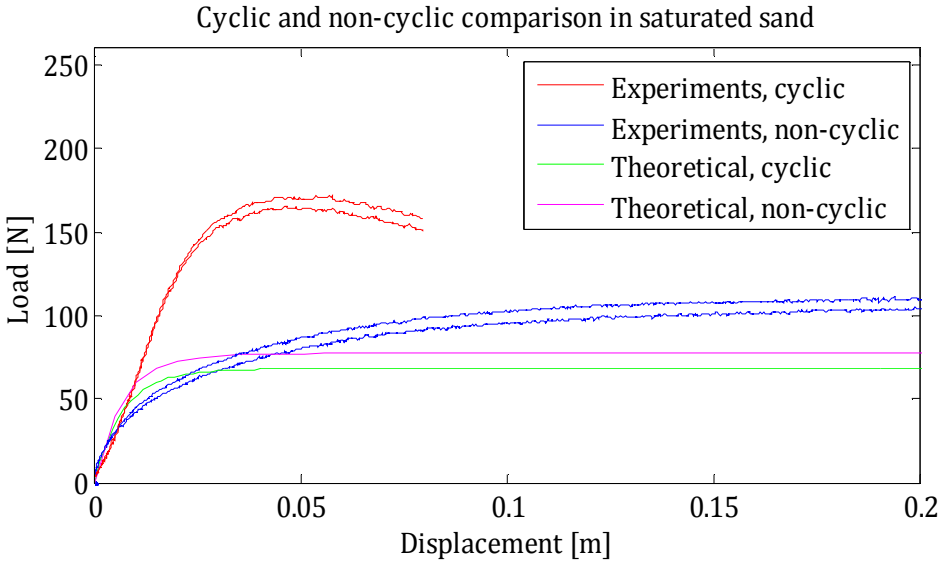

Figure 8.14: Curves in saturated sand for static loading with and without preceding cyclic loading.

From these figures it can be seen that the ultimate bearing capacity as well as the general stiffness of the curves are improved significantly when the pile is subjected to preceding cyclic loading. The theoretical p-y curves show the opposite effect; the ultimate resistance and the stiffness are reduced for cyclic loading. The change in stiffness and ultimate resistance for cyclic loading in the theoretical p-y curves is caused by the empirical adjustment factor, *A*. The experimental results show that both the stiffness and the ultimate resistance should be increased for the p-y curves. Except in the upper soil layers where the soil is gone after cyclic loading.
This means that the experiments executed in this project show that the attempt of accounting for cyclic loading in the theoretical p-y curves only amplifies makes the deviations from reality.

8.2 Secant stiffness

Both Klinkvort et al [14] and LeBlanc et al [7] have found that the secant stiffness increases with the number of cycles. The secant stiffness is defined as the slope between the end points of the load-displacement curve from the cyclic tests, see figure 8.15.

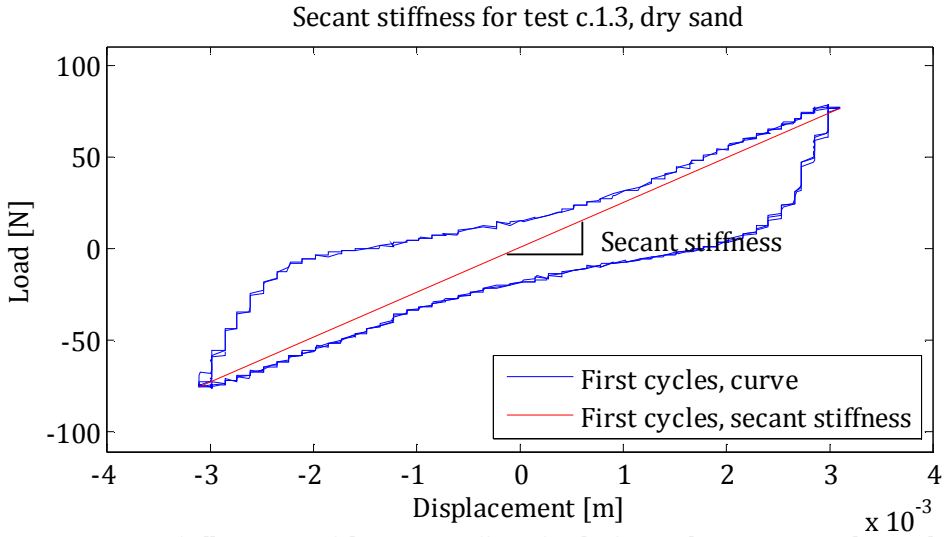

Figure 8.15: Illustration of the secant stiffness for the first cycles in test c.1.3, dry sand.

The secant stiffnesses for different numbers of cycles for test s.1.3 in dry sand are shown in figure 8.16.

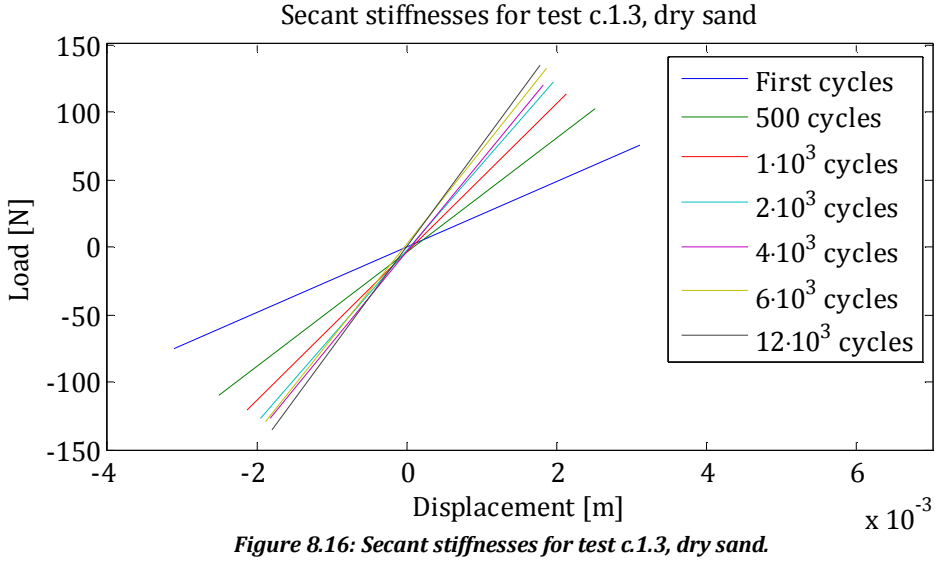

Figure 8.16: Secant stiffnesses for test c.1.3, dry sand.

The secant stiffnesses for different numbers of cycles for test s.4.2 in saturated sand are shown in figure 8.17.

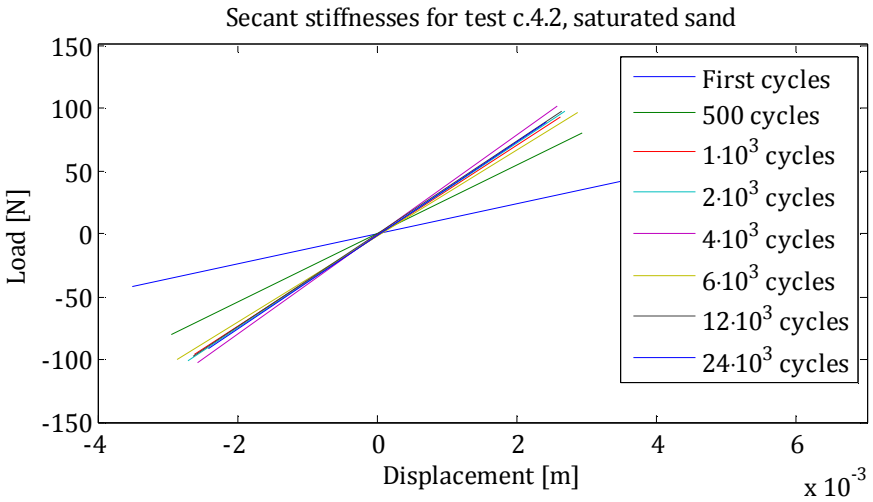

Figure 8.17: Secant stiffnesses for test c.4.2, saturated sand.

Figure 8.16 and figure 8.17 show that secant stiffness increases significantly with the number of cycles, especially in the beginning. The secant stiffnesses determined for dry and saturated sand are shown in table 8.2.

Number of cycles	Secant stiffness, dry sand [N/m]	Secant stiffness, saturated sand [N/m]
First cycles	$2.4 \cdot 10^4$	$1.2 \cdot 10^4$
500	$4.2 \cdot 10^4$	$2.7 \cdot 10^4$
$1 \cdot 10^3$	$5.5 \cdot 10^4$	$3.6 \cdot 10^4$
$2 \cdot 10^3$	$6.4 \cdot 10^4$	$3.7 \cdot 10^4$
$4 \cdot 10^3$	$6.8 \cdot 10^4$	$4.0 \cdot 10^4$
$6 \cdot 10^3$	$7.0 \cdot 10^4$	$3.4 \cdot 10^4$
$12 \cdot 10^3$	$7.6 \cdot 10^4$	$3.7 \cdot 10^4$
$24 \cdot 10^3$	-	$3.8 \cdot 10^4$

Table 8.2: Secant stiffnesses for dry and saturated sand.

The development in the secant stiffnesses is determined by fitting a function to the stiffnesses in table 8.2, see figure 8.18 and figure 8.19.

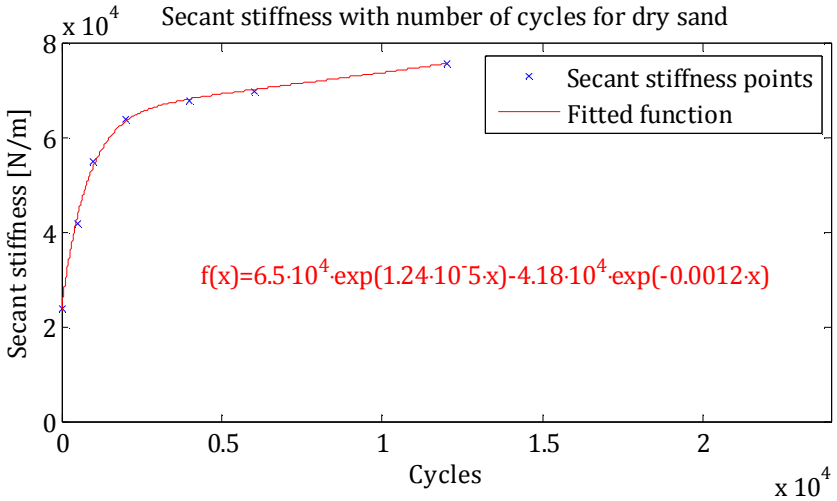

Figure 8.18: Secant stiffnesses as a function of the number of cycles and a fitted function to the points for test c.1.3, dry sand.

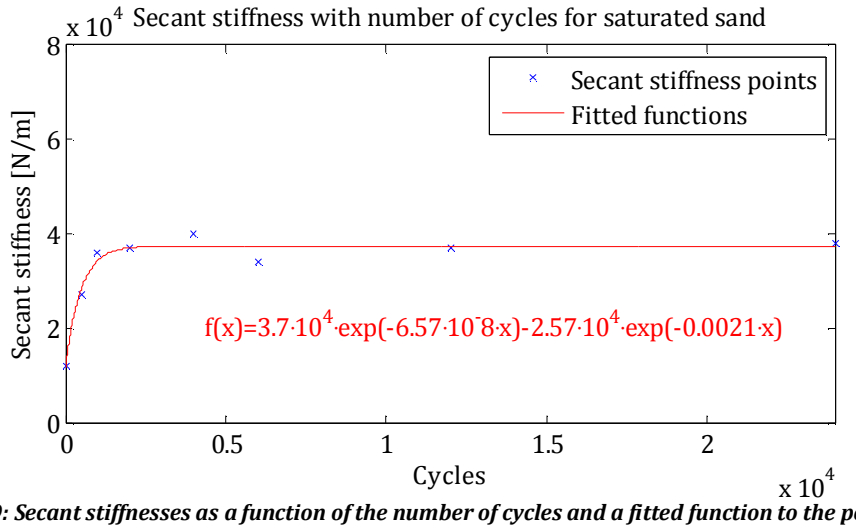

Figure 8.19: Secant stiffnesses as a function of the number of cycles and a fitted function to the points for test c.4.2, saturated sand.

It can be seen from figure 8.18 and figure 8.19 that the change in the secant stiffness happens mostly within the first 2000 cycles. These two tests indicate that the steady state is reached earlier for saturated sand than for dry sand but more tests need to be conducted to confirm this. If this tendency is confirmed, it can be concluded that the soil has reached maximum stiffness already after 2000 cycles.

8.3 2D modelling of cyclic loading

In order to apply the results of the cyclic tests in modern engineering practice the tendencies observed in the tests need to be incorporated in a numerical model. In this section we discuss different cyclic models.

A 3D model could probably be used for this purpose but solving only for static loading is a time consuming procedure. From the investigation of the p-y method we know that having the correct input a simple 2D model can provide reasonable results for the static load case. Therefore an efficient model for predicting cyclic response could be an extension of the 2D beam model on a Winkler foundation. The challenge is to define a local spring that resembles the correct cyclic response. Such models are already developed, by El Naggar et al. [20] and Hededal et al [21].

El Naggar et al. presented in an article from 2004 two different spring responses regarding two different types of soil behaviour; gapping and cave-in. Gapping is an effect believed to occur in cyclic loading in cohesive soils such as clay, whereas cave-in is believed to occur in non-cohesive soil such as sand.

Gapping means that a hole develops behind the pile during loading. When changing the loading direction the hole remains and the pile will only face resistance from some drag acting on the sides of the pile. The principle is illustrated in figure 8.20.

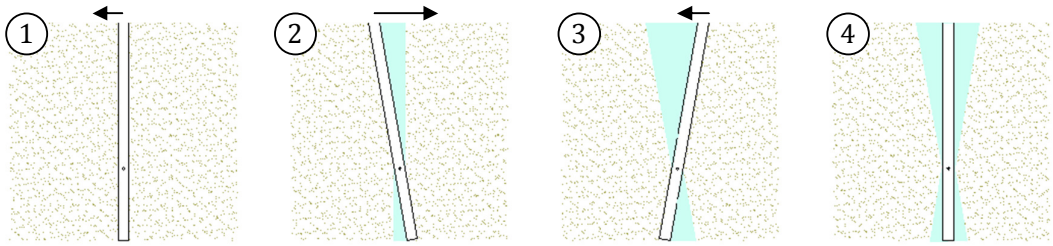

Figure 8.20: Gapping. Piles illustrate loading direction. 1) The pile is in its initial position and has not yet been loaded. 2) The pile has been loaded and a gap has occurred on the back of the pile. 3) The pile has been further loaded in the co-direction, and a gap on the front side therefore is developed. 4) The pile is back in its initial position, and a permanent gap has developed on both sides of the pile. The blue area shows the gap-zone.

A principal drawing of the local spring response in case of gapping is shown in figure 8.21.

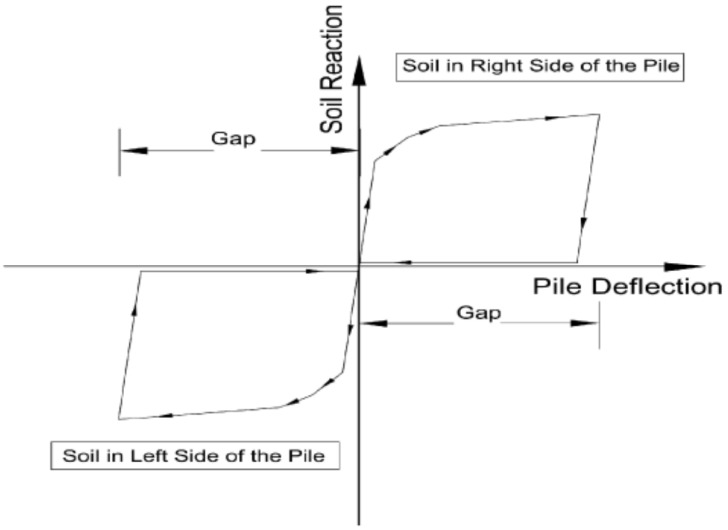

Figure 8.21: Typical Soil reaction – Pile deflection behaviour in cohesive soils (gapping), cf. [20].

In a cave-in behaviour the soil will cave in and close the gap. A principal drawing of this is shown in figure 8.22.

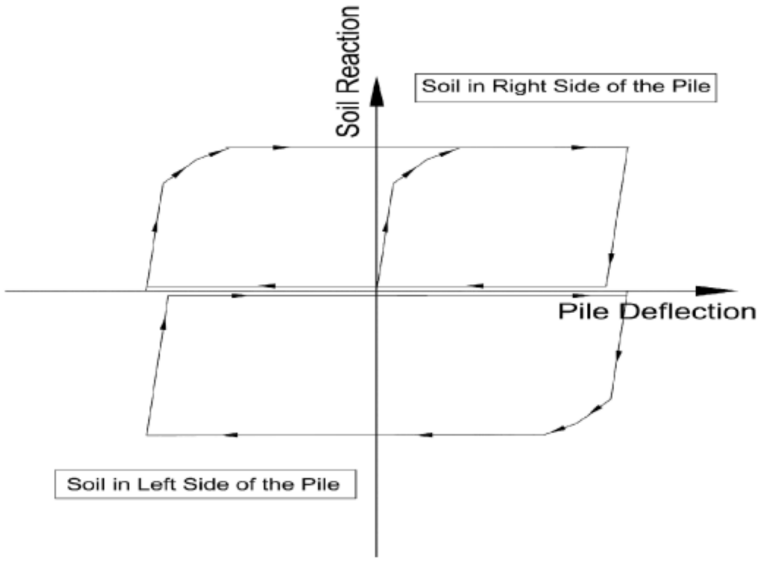

Figure 8.22: Typical Soil reaction – Pile deflection behaviour in cohesionless soils (cave-in), cf. [20].

Klinkvort presented in 2009 an article regarding centrifuge tests of cyclic loaded piles in sand, [U.8]. The results of the centrifuge tests indicated that a cave-in effect did not fully develop.
Therefore the two models of El Naggar are discussed in an article by Hededal and Klinkvort from 2010 [21]. They conclude that probably it is necessary to include the drag effect in a model, even for cohesionless soils. Therefore a model which is quite similar to the gap-model from el Naggar et al [20] is presented. In the gap-model of Hededal et al, [21], some drag is included. The drag is due to friction on the sides of the pile. We refer to this model as the drag-spring model. A principal drawing of this is shown in figure 8.23.

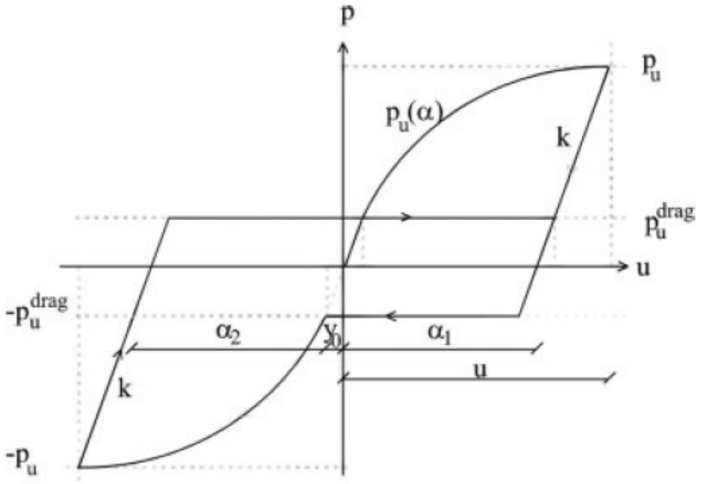

Figure 8.23: Schematic drawing of the drag-spring element, cf. [21]

In the article [21], the model from figure 8.23 is implemented for the springs as a plasticity model. The spring response and the overall response are shown in figure 8.24.

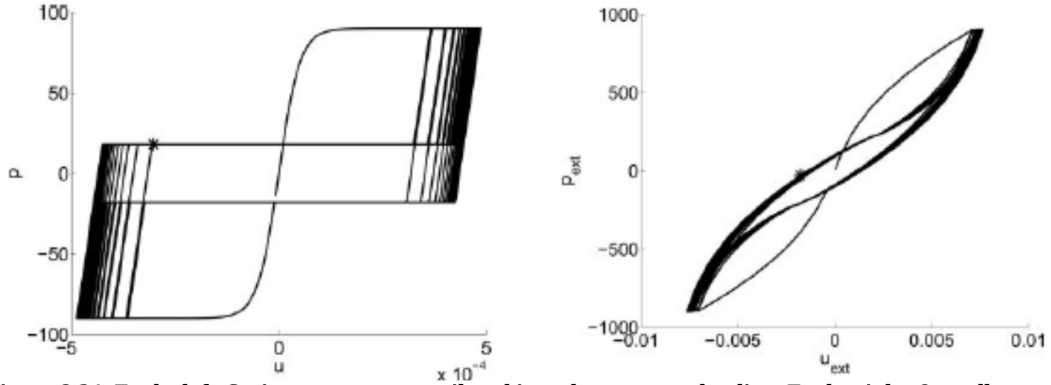

Figure 8.24: To the left: Spring response to a pile subjected to two-way loading. To the right: Overall response subjected to two-way loading, cf. [21].

The overall response has certain similarities with the cyclic results presented in this project, see section 5.3 p. 36 Therefore the model of Hededal could be applicant for our type of problem.

In the cyclic experiments presented in this report also the development of a gap has been discovered. This is pictured in figure 5.13 p. 40.
Apparently, the gap only develops in the upper layers. Meanwhile the sand in the lower layers are hardening. We believe that cave-in effect is the effect most likely to occur in sand and when the gap in the upper layers develops it is due to sand in the lower layers being compressed why more sand is used to close the gap in these layers. Sand therefore is transported away from the upper layers to close the gap in the lower layers causing the gap.

A numerical model should be a general model that can account both for the above described behaviour as well as the development in strength and stiffness parameters during cyclic loading.

In a numerical model therefore we believe that a combination of drag-springs and cave-in springs are needed. The hardening tendency should be applied to the cave-in springs. As the cave-in springs reaches their maximum stiffness the drag is lowered until the drag-spring is equal to a gap-spring. The principle is illustrated in figure 8.25.

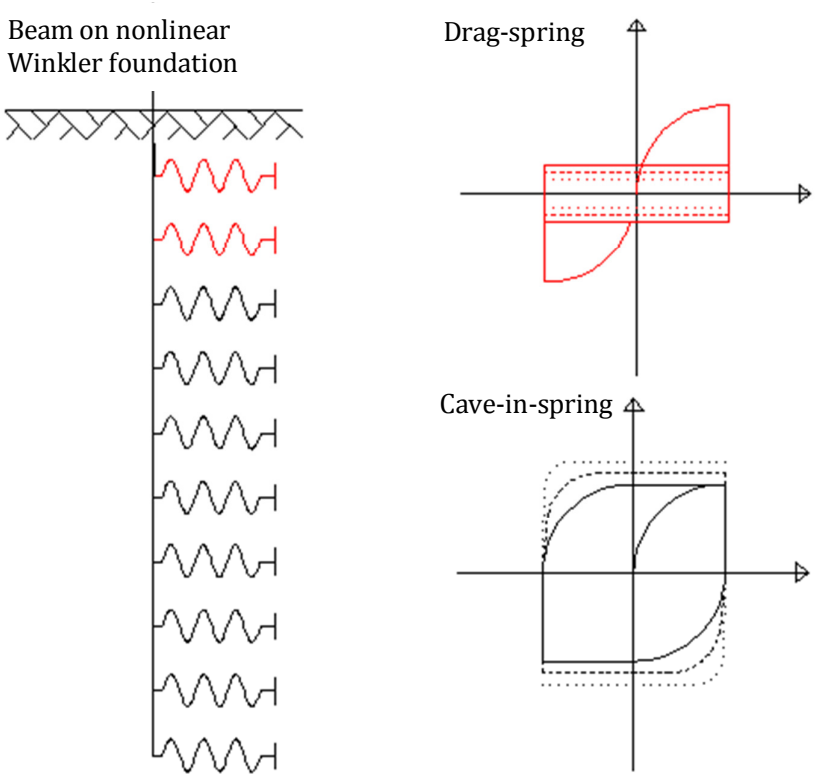

Figure 8.25: Proposed model for cyclic loading. To the left: Beam on nonlinear Winkler foundation. The beam is supported by drag-springs in the upper soil layers. In the bottom soil layers the beam is supported by cave-in springs. To the right: The two types of springs: the continuous line is at time 0, dashed line is at time 1 and dotted line is at time 2. As the cyclic loading continues the drag-springs becomes more like gap-springs and the cave-in springs are improved in strength and stiffness.

The assumptions here are based on a quasi-static loading. Probably effects of damping also need be considered.

9 Conclusion

The scope of this report is to:

- Investigate the shape of the theoretical p-y curves
- Investigate the p-y method
- Investigate the effect of cyclic horizontal loading of a pile, including effects of different frequencies
- Investigate alternative designing methods, i.e. 3D modelling in Abaqus and Plaxis 3D.

To achieve this, an experimental program is conducted and 2D nonlinear beam model and two 3D nonlinear FEM models are established.

The experimental program consists of:

- P-y experiments to determine experimental p-y curves for comparison with the theoretical p-y curves. Both direct comparison and comparison of the global response though a nonlinear Winkler model is performed.
- Static experiments with and without preceding cyclic loading in both dry and saturated sand. The results are compared to assess the influence of cyclic loading. The results are also compared to the three FEM models in order to assess the reliability of each model.
- Cyclic experiments for analysing the effects of cyclic loading on both dry and saturated sand.

The experimental work was carried out on the Esbjerg Campus. The three different experimental setups are homemade and appear somewhat simple. Preparation of the soil domain is processed by hand from time to time and therefore average density can vary from time to time. The variation is assessed not to be of great importance the tests have been repeated with similar results from time to time. Boundary effect is a risk that has been assessed not present, this however is only visually accounted for, by evaluating the surface of the soil domain after performed tests. The results therefore are assessed reliable.

The tests were performed under low stress conditions. This has an influence on the friction angle, which is varying with depth instead of being constant. This has been accounted for, by using a relation between friction angle and depth determined by review of results from triaxial tests performed by Krabbenhøft et al. [16].
In connection with the 3D models the soil domains have been layered in five layers to include the effect of varying φ.
Regarding the value of the initial modulus of subgrade reaction, an explicit expression is determined and extrapolated to include values for friction angles greater than 40°. This has proved to be a reasonable approach.
Therefore it is reasonable to compare the test results from static tests to the results of the numerical models. It is also reasonable to compare results of p-y experiments to theoretical p-y curves.

Direct comparison of theoretical and experimental p-y curves show that the shape of the theoretical p-y curves appears to be wrong for the static case.

- The theoretical p-y curves are generally too steep and prescribe an ultimate bearing capacity that is generally too low for static loading.

This results in the global response also being too steep with a bearing capacity that is too low when theoretical p-y curves are applied as boundary conditions in the nonlinear Winkler model

and the results are compared to static experiments. This is valid for both dry and saturated conditions. Hence, the warning in the DNV, presented in section 1.4 p. 9, appears to be justified.

Another finding is that the p-y method as principle appears to be reasonable. When experimental p-y curves are used as boundary conditions in a Winkler model the global response predicted by the model is in perfect correspondence with the experimental results from static tests. This is valid in dry conditions. Saturated conditions have not been investigated but we believe the tendency to be the same.

- The p-y method is a reasonable modelling approach in static loading, given correct input functions for the nonlinear springs.

One major finding in this project is the hardening tendency. The cyclic experiments have shown that the stiffness of the sand increases with the number of cycles and the increase is most significant within the first 2000 cycles. For saturated sand, the secant stiffness is more than doubled within 2000 cycles of cyclic loading.
The static tests conducted with preceding cyclic loading show a significant increase in the ultimate bearing capacity by up to 80 % and also a significant increase in stiffness.
The theoretical p-y curves are decreased both in stiffness and ultimate bearing capacity for cyclic loading. The findings in this project indicate that the influence of cyclic loading is the opposite.

- The stiffness and ultimate bearing capacity improves significantly due to cyclic loading.

It should be noted that the stiffness of the static curves after preceding cyclic loading is coinciding with the stiffness of the load-displacement curves from the beam nonlinear Winkler model, when applying the theoretical p-y curves as boundary conditions. However, the ultimate bearing capacity is highly underestimated using the theoretical p-y curves. It seems that in disturbed soil conditions, the theoretical solution is on the safe side.

The results of the cyclic experiments indicate no clear tendency toward the effects being influenced by the loading frequency. This should be investigated further.

The results of the 3D finite element models show that the stiffness of load-displacement curves from the Plaxis model are too large and the shape is too linear compared to the experimental results. The results of the Abaqus model shows that the ultimate resistance is too large compared to the experimental results but the initial slopes of the load-displacement curves are coinciding with the experimental results. The converged element size in the Plaxis model is much larger than in the Abaqus model. This is a plus as the calculation time is short.

As the Abaqus model produces far better results compared to the test results than the Plaxis model and the calculation time is reasonable despite the small element size it is assessed that Abaqus 3D model with a user defined material model is the best for simulating the behaviour of a single pile in dry sand. This means that it is possible to establish a 3D finite element model of a horizontally loaded monopile in sand using a user defined material in Abaqus 3D.

- With the Abaqus model it is possible to determine the initial slope of the load-displacement curve very well.

10 References

[1] *Cost Reduction Prospects for Offshore Wind Farms*
M. Junginger, A. Faaij, W. C. Turkenburg
Wind Engineering, vol. 28, No. 1, 2004, pp. 97–118 97
Copernicus Institute, Utrecht University, The Netherlands.

[2] *Static and dynamic analysis of an offshore mono-pile windmill foundation*
L. Kellezi and P. B. Hansen
GEO - Danish Geotechnical Institute, Lyngby, Denmark 2003

[3] *Analysis of Beams on Elastic Foundations using Finite Difference Theory*
G. Jones
Thomas Telford, 1. Udgave, 1997
ISBN: 0727724886

[4] *Die Lehre von Elastizität und Festigkeit*
E. Winkler
Prag, 1867

[5] *An evaluation of p-y relationships in sands*
M. W. O'Neill and J. M. Murchison
Research Report No. GT-DF02-83
University of Houston, Department of Civil Engineering, May 1983.

[6] *Analysis of Laterally Loaded Piles in Sand*
L. C. Reese, W. R. Cox and F. D. Koop
Proceedings of the Sixth Annual Offshore Technology Conference, Houston, Texas
2. paper no. OTC 2080, 1974

[7] *Response of stiff piles in sand to long-term cyclic lateral loading*
G. T. Houlsby, and B. W. Byrne.
Géotechnique 60, No. 2, 79–90, 2010.

[8] OFFSHORE STANDARD, DNV-OS-J101
Design of offshore wind turbine structures
October 2010

[9] *API Recommended Pratice 2A-WSD*
Recommended Practice for Planning, Designing and Constructing Fixed Offshore Platforms – Working Stress Design, Twenty-first Edition, December 2000.
Errata and supplement 1, 2002 and Errata and supplement 3, 2008.

[10] *Bearing capacity and settlement of piles*
K. Gwizdala and M. Jacobsen
Centraltrykkeriet, Aalborg University, June 1992.

[11] *Evaluation of coefficients of subgrade reaction*
K. Terzaghi
Geotechnique, No. 4, pp. 297-326, 1955

[12] *Evaluation of Pile Diameter Effect on Initial Modulus of Subgrade Reaction*

S. A. Ashford and T. Juirnarongrit
Journal of geotechnical and geoenvironmental engineering, ASCE march 2003

[13] *Review of p-y Relationships in Cohesionless Soil*
K. T. Brødbæk, M. Møller and S. P. H. sørensen
Aalborg University, January 2009

[14] *Centrifuge modeling of a laterally cyclic loaded pile*
R. T. Klinkvort, C.T. Leth and O. Hededal
Technical University of Denmark, Copenhagen, Denmark
Physical Modelling in Geotechnics – Springman, Laue & Seward (eds)
2010 Taylor & Francis Group, London
ISBN: 978-0-415-59288-8

[15] *An efficient return algorithm for non associated plasticity with linear yield criteria in principal stress space*
J. Clausen, L. Damkilde and L. Andersen
Computers and structures 85, pp. 1795-1807, 2007

[16] *The carrying capacity of circular foundations in sand – comparison between model tests and numerical simulations based on a non-linear Mohr-Coulomb failure envelope*
Sven Krabbehoft, Johan Clausen, Lars Damkilde
Esbjerg Institute of Technology, Aalborg University, Niels Bohrs Vej 8, 6700 Esbjerg, Denmark
In proceedings, unpublished

[17] *Scale Effects of Shallow Foundation Bearing Capacity on Granular Material*
A. B. Cerato and A. J. Lutenegger
Journal of geotechnical and geoenvironmental engineering
ASCE, Vol. 133:10, 1192-1202, 2007

[18] *Stålkonstruktioner efter DS 412*
B. Bonnerup and B. C. Jensen
Nyt Teknisk Forlag, 3. Edition, 2007
ISBN 978-87-571-2604-4

[19] *Plaxis 3D foundation, Material models manual*
Version 2

[20] *Nonlinear response analysis of offshore piles under seismic loads*
M. Kimiaei, M. A. Shauanfar, M. H. El Naggar, A. A. Aghakouchak
13th World Conference on Earthquake Engineering
Vancouver, B.C., Canada, August 1-6, 2004, Paper No. 3056

[21] *A new elastoplastic spring element for cyclic loading of piles using the p-y-curve concept*
Ole Hededal & Rasmus Klinkvort
Department of Civil Engineering, Technical University of Denmark, 2010

[W.1] http://greenworldinvestor.com/2011/04/18/offshore-wind-farms-list-of-the-major-offshore-wind-projects-and-future-wind-plants/

[W.2] http://www.londonarray.com/the-project/

[W.3] http://ing.dk/artikel/108363-monstermoeller-paa-5-mw-pryder-tysklands-foerste-havmoellepark

[W.4] http://www.danskgeotekniskforening.dk/media/20091112_Design_af_monopæle_til_havvindmøller_.pdf

[W.5] http://www.flickr.com/photos/tigerhobbes/3068891511/

[W.6] http://www.wind-energy-the-facts.org/en/part-3-economics-of-wind-power/chapter-2-offshore-developments/

[W.7] http://www.sanistaal.dk/nc/da/produkter/produktkatalog.html

[U.1] *API recommended Practice for Planning, Designing and Constructing Fixed Offshore Platforms*
American Petroleum Institute, Washington D.C., 13. Edition, 1982.

[U.2] *Simplified Calculation of P-Y Curves for Laterally Loaded Piles in Sands*
D. Bogard, and H. Matlock.
Unpublished Report, Earth Technology Corp,1980.

[U.3] *Analysis of Centrifuge Pile Tests; Simulation of Pile Driving*
R.F. Scott.
Research Report, OSAPR Project 13
American Petrolium Institute, California Institute of Technology, Pasadena, California, June, 1980.

[U.4] *Experimental and Analytical Study of Behaviour of Single Piles in Sands Under Lateral and Axial Loading*
F. Parker, and L. C. Reese
Rpt. 117-2, Ctr. For Highway Research, Univ. of Texas, Austin, November, 1970

[U.5] *Ultimate Resistance Against a Rigid Cylinder Moving Laterally in a Cohesionless Soil*
L. C. Reese
Journal of the Society of Petrolium Engineers, Dec., 1962, pp. 355-359.

[U.6] *A non-linear soil model for predicting lateral pile response*
D. P. Carter
Rep. No. 359, Civil Engineering Dept., Univ. of Auckland, New Zealand, 1984

[U.7] *Back analysis of lateral load tests on piles*
L. F. Ling
Rep. No. 460, Civil engineering Dept., Univ. of Auckland, New Zealand, 1988

[U.8] *Laterally loaded piles – centrifuge and numerical modelling. Master`s thesis.*
R. T. Klinkvort. Technical University of Denmark, 2009